



Universiteit
Leiden
The Netherlands

Single-molecule dynamics at variable temperatures

Zondervan, Rob

Citation

Zondervan, R. (2006, March 16). *Single-molecule dynamics at variable temperatures*. Retrieved from <https://hdl.handle.net/1887/4327>

Version: Corrected Publisher's Version

License: [Licence agreement concerning inclusion of doctoral thesis in the Institutional Repository of the University of Leiden](#)

Downloaded from: <https://hdl.handle.net/1887/4327>

Note: To cite this publication please use the final published version (if applicable).

Single – molecule dynamics at variable temperatures

PROEFSCHRIFT

ter verkrijging van
de graad van Doctor aan de Universiteit Leiden,
op gezag van de Rector Magnificus Dr. D.D. Breimer,
hoogleraar in de faculteit der Wiskunde en
Natuurwetenschappen en die der Geneeskunde,
volgens besluit van het College voor Promoties
te verdedigen op donderdag 16 maart 2006
klokke 16:15 uur

door

Rob Zondervan

geboren te Leiden

in 1978

Promotiecommissie:

Promotor: Prof. Dr. M. A. G. J. Orrit
Copromotor: Dr. F. Kulzer
Referent: Prof. Dr. Th. Basché (Universitat Mainz)
Overige Leden: Prof. Dr. P. H. Kes
Prof. Dr. E. J. J. Groenen
Prof. Dr. M. Dogterom
Prof. Dr. J. Hofkens (KU Leuven)

The presented work is part of the research program of the Stichting voor Fundamenteel Onderzoek der Materie (FOM), which is financially supported by the Nederlandse Organisatie voor Wetenschappelijk Onderzoek (NWO).

Casimir PhD Series, Delft-Leiden, 2006-03
ISBN: 90-8593-010-3

Contents

1	Introduction	1
1.1	Ensemble versus single-molecule dynamics	1
1.2	Dynamics at varying temperature	3
1.3	Temperature cycles and single-molecule dynamics	4
1.4	Outline of the thesis	6
2	The temperature-cycle microscope	9
2.1	Inside the cryostat	10
2.1.1	The absorbing sample plate	10
2.1.2	The low-temperature microscope objective	12
2.1.3	The cryostat insert	13
2.2	Outside the cryostat	15
2.2.1	The probing optics	15
2.2.2	The heating optics	15
2.3	Imaging properties	16
3	Photoblinking of rhodamine 6G in poly(vinyl alcohol)	21
3.1	Introduction	22
3.2	Experimental	23
3.3	Results and discussion	26
3.3.1	Decay kinetics of the emissivity	28
3.3.2	Steady-state emissivity	31
3.3.3	Recovery of the emissivity	34
3.3.4	The nature of the dark state	34
3.4	Conclusion	39
4	Photobleaching of rhodamine 6G in poly(vinyl alcohol)	41
4.1	Introduction	42
4.1.1	Primary oxygen-induced photobleaching	43
4.1.2	Primary photobleaching without oxygen	43
4.1.3	Photobleaching of metastable states	44
4.1.4	Photobleaching and temperature	44

4.2	Experimental	45
4.3	Results	46
4.3.1	Ensemble experiments	46
4.3.2	Single-molecule experiments	49
4.4	Discussion	52
4.4.1	Simulations of the ensemble photobleaching	52
4.4.2	The non-exponential photobleaching kinetics	53
4.4.3	Photobleaching and excitation	54
4.4.4	Photobleaching and atmosphere	55
4.4.5	Photobleaching and temperature	55
4.4.6	Photobleaching of single molecules	56
4.4.7	Photoblinking of single molecules	57
4.5	Conclusion	58
4.6	Appendix – derivation of bleaching rates	59
5	Local temperature determination by Raman spectroscopy	63
5.1	Introduction	64
5.2	Accuracy of Raman-determined temperatures	65
5.3	Calibration of laser-induced local heating by Raman spectroscopy	67
5.4	Conclusion	69
6	Relaxation in supercooled glycerol near T_g probed by rotational diffusion	71
6.1	Introduction	72
6.2	Experimental	74
6.2.1	Sample preparation	74
6.2.2	Experimental configuration	76
6.2.3	Ensemble analysis	76
6.2.4	Single-molecule analysis	78
6.3	Results	79
6.3.1	Ensemble experiments	79
6.3.2	Single-molecule experiments at static temperatures . . .	82
6.3.3	Single-molecule experiments at variable temperatures .	87
6.4	Discussion	91
6.5	Conclusion	96
7	Demonstration of laser-driven microsecond temperature cycles	97
7.1	Introduction	98
7.2	Experimental	99

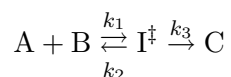
7.3	Theory – temperature measurements through molecular diffusion	99
7.4	Temperature calibration of the fluorescence anisotropy	101
7.5	Imaging the laser-induced hot spot	104
7.6	Steady-state local temperature from FACS	107
7.7	Kinetics of heating and cooling	107
7.8	Conclusion	113
8	Thermal manipulation of single-molecule dynamics	115
8.1	Triggering of single-molecule rotational diffusion by temperature jumps	116
8.2	Perspective for temperature-cycle analysis of single-protein dynamics	120
8.2.1	Polyproline – characterization of spFRET as a “spectroscopic ruler”	121
8.2.2	Cold-shock protein – an apparent two-state folder	124
	Bibliography	127
	Samenvatting	145
	List of Publications	151
	Curriculum Vitae	153
	Nawoord	155

1 Introduction

This thesis comprises two lines of work. On the one hand, we demonstrate the potential of single-molecule (and ensemble) optical microscopy at variable temperatures in the study of the photodynamics of a fluorophore in a hydrophilic environment, and in the study of the relaxation dynamics of supercooled glycerol. On the other hand, we develop and characterize a novel technique to study dynamics of molecular processes and reactions at the single-molecule level by varying the temperature. This new method, temperature-cycle microscopy of single-molecule dynamics, has the potential to extend the observation window in single-molecule optical experiments to both shorter and longer times. In addition to that, it allows rapid and reproducible adjustment of the temperature to investigate single-molecule kinetics and reaction barriers.

1.1 Ensemble versus single-molecule dynamics

In an ensemble experiment, many molecules are probed at the same time and therefore such a measurement can only yield the average behavior of the molecules. To appreciate the added value of a single-molecule experiment, which probes one molecule at a time, let us regard the following (chemical) reaction in which two molecules A and B are in equilibrium with a short-lived intermediate I^\ddagger which from time to time rearranges in a one-way step to a final product C:



When the reaction is in equilibrium, the ensemble experiment will obviously only provide the steady-state concentrations of A, B, and C. However, to fully understand the mechanism behind the reaction, i.e., for retrieving rate constants k_1 , k_2 , and k_3 , a study of its dynamics is crucial. In an ensemble experiment, this is only possible by either synchronizing the reaction, for instance in a stopped-flow experiment, or by driving the reaction far out of equilibrium through an abrupt change of a variable. Such measures are not always possible and often unacceptable if one wishes to study the reaction under its natural conditions.

The single-molecule approach automatically solves the synchronization problem. One follows an individual molecule A, waits until B attaches to observe the formation of I^\ddagger and, subsequently, waits until either dissociation back to A and B or formation of C takes place. When repeated for many molecules, single-molecule analysis not only retrieves the steady-state concentrations but also the rate constants of each step. Furthermore, it elucidates to what extent the various rate constants are distributed or correlated with each other. In additional experiments, relevant parameters, like the pH, can be varied to study the change of the reaction at the steady-state and kinetic levels. However, it should be noted that, if one is mainly interested in the average behavior of the system, an ensemble experiment should be favored, since it provides the average in one go and is in general easier to conduct than a single-molecule experiment.

Unfortunately, the detection of a single molecule is not straightforward. The most widely applied method is fluorescence detection after optical far-field excitation, pioneered by Orrit and Bernard in 1990 [1]. Only a limited number of fluorescent molecules meets the requirements (high fluorescence quantum yield, large absorption cross-section) to be detected at the single-molecule level. A work-around, often applied in biophysics, is to label a non-fluorescent molecule of interest, e.g. a protein or DNA, with one or more suitable single-molecule fluorophore(s). To study single-molecule dynamics, one not only needs to detect the molecule as an individual, but also to observe a change in its fluorescence linked to the process of interest. Two examples of applied techniques are single-pair Förster resonance energy transfer spectroscopy (spFRET) to measure the distance between two individual fluorophores (which will be discussed in more detail in Section 8.2.1), and single-molecule fluorescence polarization spectroscopy to probe the orientation of a fluorophore (used in Chapter 6 to study relaxation dynamics in supercooled glycerol).

Despite the many challenges, the field of single-molecule optics has expanded enormously in recent years. Among other things, the technique has indeed proven to be a powerful tool in the study of any dynamics, varying from photophysics, rotational or translational diffusion, RNA or protein folding, to enzymatic kinetics [2–18]. Nevertheless, the current methods are still insufficient to study fast processes (faster than 1 to 10 ms) because not enough photons can be collected during shorter integration times. Slow processes (slower than 100 s) present problems too, since photobleaching seriously limits the observation time of a single molecule, specially at room temperature (cf. Chapter 4). We intend to extend the observation window both to shorter and longer times by a new technique, temperature-cycle microscopy (see Section 1.3).

1.2 Dynamics at varying temperature

The temperature, a measure of the average energy per degree of freedom that a system contains, is a crucial parameter in any reaction or process since it determines the probability to pass its activation barrier(s). As a consequence, temperature variation can be used to determine the height of an activation barrier (Arrhenius law). Furthermore, at a reduced temperature the passage of a given barrier may become so improbable that the process will be blocked, or proceed by an alternative pathway at a much lower rate than before. In this way, by selectively “knocking out” pathways, the presence of alternative process schemes can be explored. For a simple chemical reaction, like the one between A and B of the previous section, this will probably be of limited interest. However, it will be for complicated multi-pathway processes, like protein folding [20]. To fully appreciate this notion, it is useful to imagine such a process on the level of the potential energy, by drawing a simplified repre-

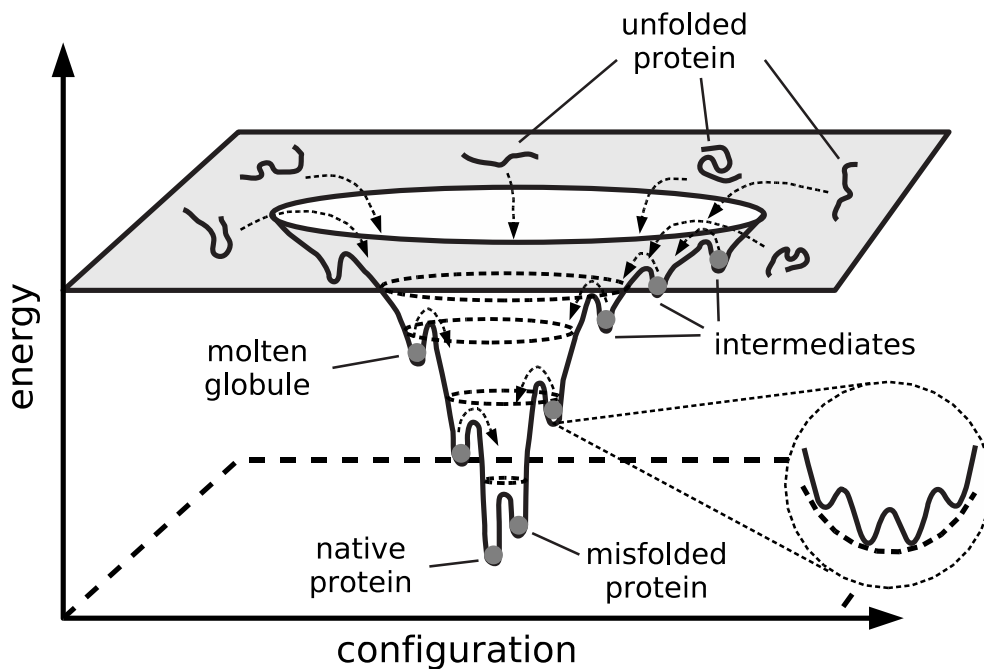


Figure 1.1: Schematic representation of a typical potential-energy landscape for protein folding. The landscape reveals the various pathways from the unfolded to the folded state. The inset shows a magnification of part of the landscape to illustrate its substructure which indicates that the folding will extend over many decades of time. The drawing is adapted from reference [19].

sentation of the potential-energy landscape of, for instance, a protein. Figure 1.1 shows a schematic example adapted from reference [19] for a typical case of protein folding. The landscape represents all possible steps and pathways during the folding process. By adjusting the temperature, the experimenter will continuously change the folding dynamics and thereby map the complete landscape. The landscape of Figure 1.1 also illustrates that such a complex process typically extends over many timescales [20]. This makes synchronization impossible (at least over times longer than microseconds), so that only single-molecule analysis will retrieve the full details of the potential-energy landscape.

The temperature can also influence reaction dynamics when additional processes are required for a reaction to occur, for example translational diffusion of reaction partners. At low temperature, the probability that two reaction partners will meet (by diffusion) is considerably lower than at high temperature. This is for instance observed for photobleaching which is greatly reduced at low temperatures because the diffusion of small, reactive molecules like water and oxygen is slowed down and eventually stopped (cf. Chapter 4 and reference [21]).

1.3 Temperature cycles and single-molecule dynamics

We propose a novel method, temperature-cycle microscopy of single-molecule dynamics, to study the dynamics of fast processes at room temperature and to facilitate variable-temperature investigations. The technique is closely related to temperature-jump experiments at room temperature: In these experiments, temperature jumps of a few Kelvin are induced by nanosecond to picosecond laser pulses to unfold DNA, RNA, polypeptides, or proteins [22–31]. Fast heating is achieved by dumping a large amount of optical energy into the sample. The subsequent cooling is slow, because it entirely relies on heat diffusion out of a rather large volume. Since active optical cooling is impossible, we propose to speed up cooling by dramatically reducing the sample volume. Placing our sample in a cold cryostat, we heat a small volume up to room temperature with a continuous-wave laser focused on an absorbing metal film. The moment the heating laser is switched off, the heated volume quickly reverts to the cryostat temperature. In this way, we can repeatedly cycle the temperature between a low and a high value, as schematically presented in Figure 1.2. With a diffraction-limited hot spot about 1 μm in size, the expected heating and cooling times are on the order of a microsecond.

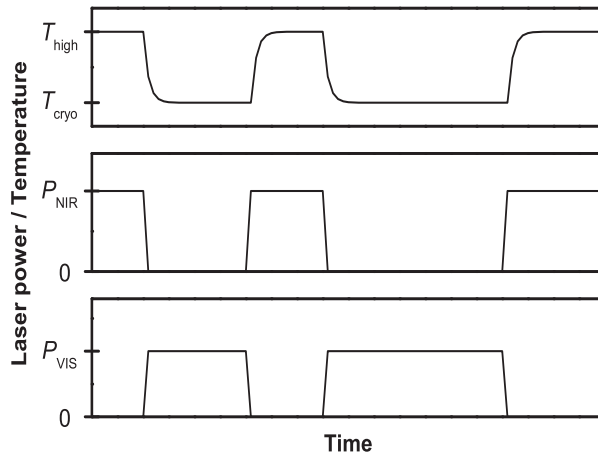


Figure 1.2: Scheme of the proposed thermal cycles between cryogenic and room temperatures. A focused near-infrared (NIR) laser beam with power P_{NIR} (middle graph) rapidly raises the local focus temperature to T_{high} (top graph). The moment the NIR laser is switched off, the temperature quickly drops back to the surrounding temperature T_{cryo} . In single-molecule experiments, a visible laser (bottom graph) with power P_{VIS} will excite fluorescent labels during the cold periods at T_{cryo} only.

Fast thermal cycles attractively dovetail with single-molecule analysis. Indeed, although fast cooling requires a huge temperature gradient, a single molecule can always be placed at the center of the focal spot, where the gradient vanishes. In contrast to this, the temperature inhomogeneity would seriously degrade the outcome of traditional ensemble measurements. The temperature cycles allow us to study fast dynamics at room temperature by repeatedly quenching the process of interest at a lower temperature. In this way, we reconstruct the process through a series of frozen structural snapshots that are optically analyzed at low temperature (cf. Figure 1.2). The time resolution of our experiment will be determined by the time it takes to quench the process, which is directly related to the cooling time. In Chapter 7 we will show that the quenching time can be as short as a microsecond. This would constitute an improvement in time resolution of about three orders of magnitude compared to conventional single-molecule experiments at room temperature. We also expect a significant improvement in the total observation time, since the optical probing is performed at low temperature (cf. Figure 1.2) where photobleaching is considerably reduced compared to the situation at room temperature (cf. Chapter 4). Furthermore, the localized heating will make temperature variation much easier and quicker than in experiments where the macroscopic (cryostat) temperature as a whole is varied.

1.4 Outline of the thesis

Chapter 2 describes the variable-temperature fluorescence microscope that we have built to perform the temperature-cycle experiments. This chapter will address its operation principle and its imaging properties.

Chapters 3 and 4 describe the results of ensemble experiments to characterize photoblinking and photobleaching of a typical organic dye (rhodamine 6G) in a typical hydrophilic matrix (the polymer poly(vinyl alcohol)). We have identified the radical anion of rhodamine 6G as responsible for the majority of photoblinking events and as the most important intermediate in photobleaching. Chapter 4 also presents single-molecule experiments to investigate the effect of the radical dark state on the observation of single molecules. After we had published two papers concerning this work, radical dark states have been reported as important intermediates in the photodynamics of many other systems as well, such as rhodamine 6G in glycerol (Chapter 7 of this work), water-soluble perylenedicarboximide [32] and terrylene [33] in poly(vinyl alcohol), multi-chromophoric dendrimers [34], the cyanine dye Cy5 when attached to DNA [35], and perylenedicarboximide in poly(methyl methacrylate) [36].

Chapter 5 reports on our efforts to apply Raman scattering to probe the temperature of a laser-induced micrometer-sized hot spot. Although we have managed to determine the local temperature with rather high accuracy and have demonstrated laser-induced local heating, the required accumulation times of minutes made us seek other techniques for further characterization of the laser-induced thermal cycles. The results of this chapter serve therefore mainly as an additional proof of the feasibility of local heating in our experimental scheme.

Chapter 6 shows our results of fluorescence polarization autocorrelation experiments on perylenedicarboximide in supercooled glycerol closely above its glass-transition temperature at the ensemble and single-molecule levels. The autocorrelation experiments probe the rotational diffusion of the fluorophores and thus give insight into the relaxation dynamics of supercooled glycerol. We have not only investigated distributions of single-molecule rotation times at static temperatures, but we have also followed the rotational diffusion of one single molecule at a time as a function of the temperature. We believe that our experiments provide fundamental insight into the dynamical heterogeneity in glass-forming liquids.

Chapter 7 constitutes the actual demonstration of the proposed laser-induced temperature cycles. We have probed the local temperature between 200 and 350 K by the temperature dependence of the fluorescence anisotropy of rhodamine 6G in glycerol. The short accumulation time required to determine

the anisotropy helped us image the heating profile and observe heating and cooling in real-time. We also present a more accurate local-temperature calibration between 200 and 220 K by fluorescence anisotropy autocorrelation experiments.

Chapter 8 presents applications of temperature jumps and temperature cycles to manipulate or study single-molecule dynamics. We show an example of thermally induced reactivation of the rotational diffusion of an immobilized single molecule and discuss the perspectives for the application of the temperature-cycle technique to the study of single-protein folding.

2 The temperature-cycle microscope

In this chapter, we present the setup that we have developed to perform temperature-cycle experiments on single molecules. This temperature-cycle microscope is schematically shown in Figures 2.1 and 2.2. It combines a low-temperature fluorescence microscope with single-molecule sensitivity and a heating path for the fast temperature cycles. The sample, a fluorophore-doped film spincoated on an absorbing substrate, is mounted in a cryostat (Janis SVT-200-5). Figure 2.1 shows the configuration of the sample plate in the cryostat with the two separate optical pathways for probing and heating. The probing beam (514.5 nm) enters the cryostat through its bottom window and is focused by a custom-made low-temperature microscope objective (NA = 0.85) onto the sample. The near-infrared (NIR) heating beam (785 nm) enters the cryostat through one of its side windows, is directed downward by a 45 degree mirror and focused by an aspheric singlet lens (NA = 0.68). This 4π -like geometry was chosen to prevent photobleaching of the sample which could be caused by two-photon excitation by the NIR laser during extended heating periods. The sample plate and the NIR lens (together with the 45 degree mirror) are held by a home-built cryostat insert, which will be described in Section 2.1.3. This insert facilitates the independent adjustment of both elements in three dimensions so that the visible and NIR foci can be overlapped on the same sample position.

The part outside the cryostat comprises two separate optical “sub-setups” that handle the optical probing (514.5 nm) and the NIR heating (785 nm), see Figure 2.2. The probing part is a laser-scanning confocal microscope and takes care of the excitation and subsequent, polarization-dependent, detection of fluorescence. The heating part is also a laser-scanning confocal microscope but without detection path. An acousto-optical modulator (AOM) (AA Opto-Electronic) is placed in the NIR beam to allow modulation and fast switching of the heating laser. In the rest of this chapter, the components inside and outside the cryostat are described in more detail. In the last section, the imaging properties of the microscope are discussed.

The experiments reported in Chapters 5, 7, and 8 have been performed with the complete temperature-cycle microscope. The results of Chapter 6 have been obtained with only the optical probing part (and a non-absorbing sample

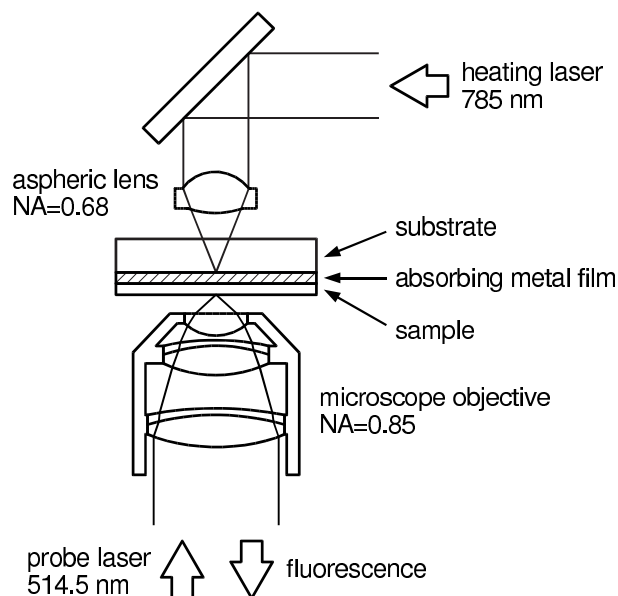


Figure 2.1: Scheme of the optical paths around the sample plate in the cryostat (not to scale). The figure shows the absorbing sample plate required for sufficient NIR laser absorption. It consists of a glass substrate (thickness 0.17 mm), coated with a thin, absorbing metal film (thickness 50 nm), itself covered with the fluorescent sample layer. Fluorescence is excited (514.5 nm) and collected by the custom-made ten-lens objective (NA = 0.85, represented here by a simplified five-lens scheme) beneath the sample. Above it, a mirror at 45 degree and an aspheric singlet lens (NA = 0.68) direct and focus the NIR beam (785 nm) onto the metal film right above the visible focus.

plate). The ensemble experiments on rhodamine 6G in poly(vinyl alcohol), Chapters 3 and 4, have been conducted on a separate setup that is described in Section 3.2. The setup for the single-molecule experiments of Chapter 4 is presented in Section 4.2.

2.1 Inside the cryostat

2.1.1 The absorbing sample plate

For successful temperature-jump or -cycle experiments, we require to reach room temperature in the laser-induced hot spot while the cryostat temperature is typically around 100 K. To obtain such a large temperature increase, one cannot rely on absorption by the sample medium (which should be trans-

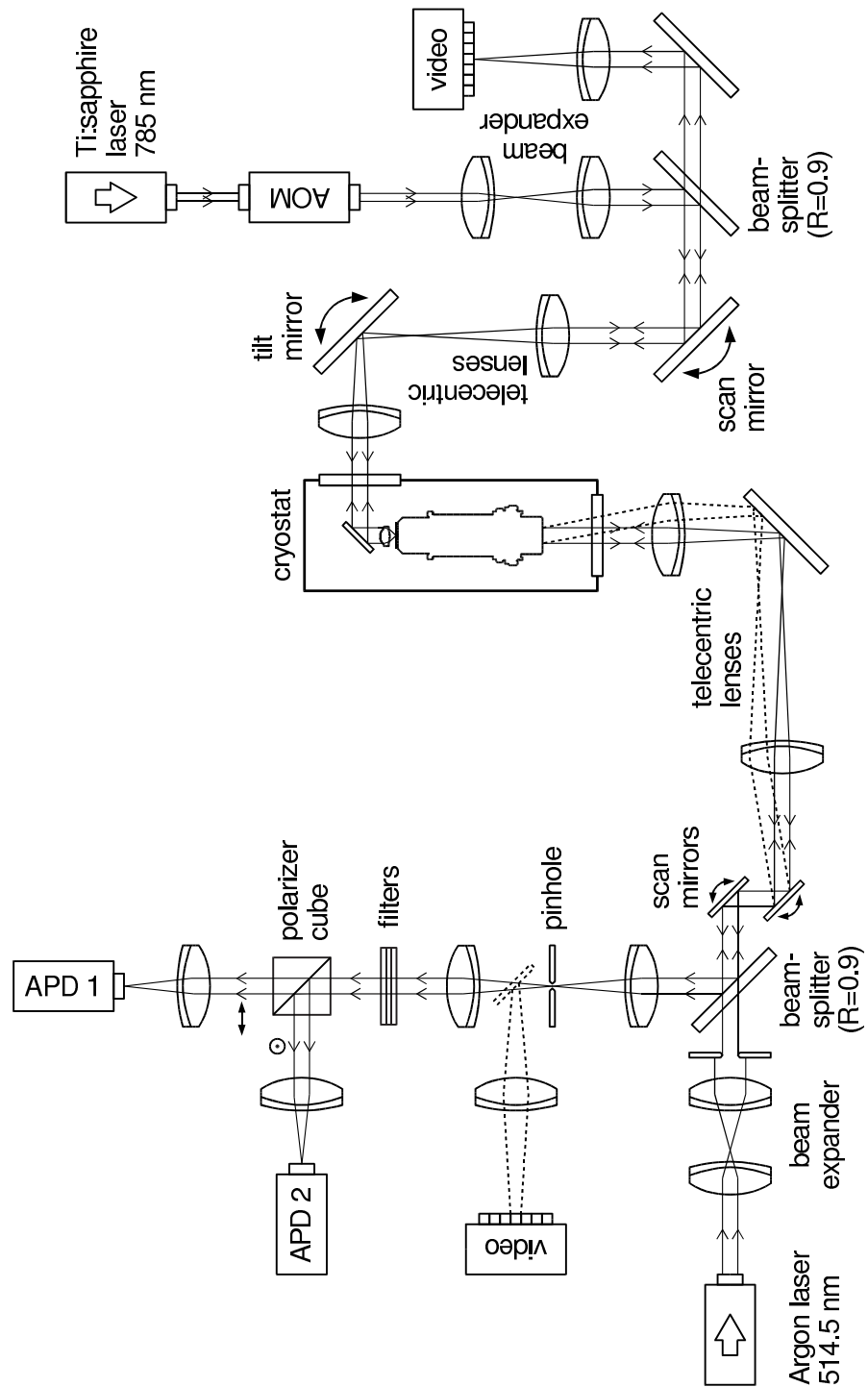


Figure 2.2: Schematic representation of the temperature-cycle microscope. The optical probing part is shown to the left of the cryostat, the heating part to the right. All the components are discussed in the text.

parent). Previous studies of heating effects in intense laser fields, for instance in multi-photon spectroscopy [37, 38] or in optical traps [39–41], in optically clear samples and for practical powers, have achieved a temperature rise of a few Kelvin at most. We have therefore decided to place our sample in contact with an efficient absorber of NIR radiation, in our case a thin metal layer on a glass substrate. This absorbing sample plate (cf. Figure 2.1 for its position in the cryostat) is a standard 20 mm round cover slide of BK 7 (thickness 0.17 mm) coated with a thin (50 nm) sputtered metal layer. We chose thin films because the residual NIR transmission helps alignment, and to reduce heat conduction by the metal. The work presented in this thesis is performed with either home-made nickel-chromium films or commercial chromium films (Berliner Glas, Berlin, Germany). The absorption of metal films strongly depends on preparation [42]. Our NiCr films absorb about 30–40% and transmit 2% at 785 nm. The chemically inert Cr films absorb roughly 10–15% and transmit approximately 1%. The Cr films can be optionally coated with a thin (50 nm) silica layer to reduce quenching by isolating the fluorophores from the metal.

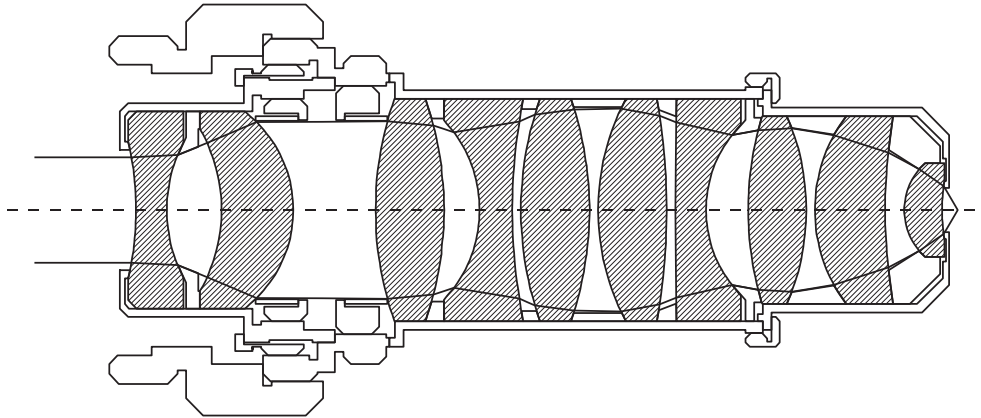


Figure 2.3: Schematic drawing of the custom-made ten-lens microscope objective for repetitive operation at cryogenic temperatures. The optical axis is shown as a dashed line, while two solid lines indicate the limiting rays upon exact filling of the objective's aperture.

2.1.2 The low-temperature microscope objective

The low-temperature microscope objective (NA = 0.85, 60 times), cf. Figure 2.3, has been specially developed for repetitive operation at cryogenic temperatures in cooperation with the company Bernhard Halle Nachfolger (Berlin,

Germany). This custom-made objective replaces commercially available 5-lens objectives, which often survive only a few cycles between room- and low temperatures. Its anti-reflection coated lenses are made from glasses selected for their low thermal expansion and resistance to moisture (condensation). The lenses, mounted without any glue or cement, are held in place by spacer rings in a titanium housing. Longitudinal slits are cut in this housing to allow for thermal expansion during thermal cycles. The objective is infinity-corrected and generates near-diffraction-limited excitation spots.

2.1.3 The cryostat insert

The home-built cryostat insert consists of two parts: the objective holder at the bottom, and the sample holder, the long top part that also carries the NIR lens. Figure 2.4 shows a detailed drawing of the lower third part of the cryostat insert, which contains all the parts that are included in Figure 2.1.

The objective holder is spring-loaded against the cryostat's bottom, and remains in the cryostat upon sample change. It contains the ten-lens low-temperature microscope objective. The sample holder is coupled kinematically to the objective holder by three self-locking prongs. The sample plate is mounted at the lower end. On the sample mount, close to the sample plate, a silicon diode (Lakeshore) measures the actual cryostat temperature near the sample. The sample mount can be moved in three dimensions by piezo-driven inchworm motors (Attocube Systems). The "axial" piezo motor shifts the sample vertically into the focus of the microscope objective. The other two piezo motors command an area of $5 \times 5 \text{ mm}^2$ in the sample plane. The NIR heating beam is reflected down by a mirror onto a singlet lens with NA 0.68 (Thorlabs 350330-B). The mirror and the lens are mounted together above the sample. This assembly can also be positioned in three dimensions: A fourth piezo motor shifts the lens vertically to bring its focus at the metal-glass interface. With two mechanical controls, we can position the lens-mirror assembly with micrometer precision in the (x,y) focal plane. These controls actuate two spring-loaded flexure hinges, which are elastically deformable bridges thinned out in one metal piece. When slightly tilted around either hinge, the lens-mirror holder also shifts in the sample plane. Our group has previously shown that flexure hinges provide reliable and stable positioning in low-temperature microscopy [43, 44].

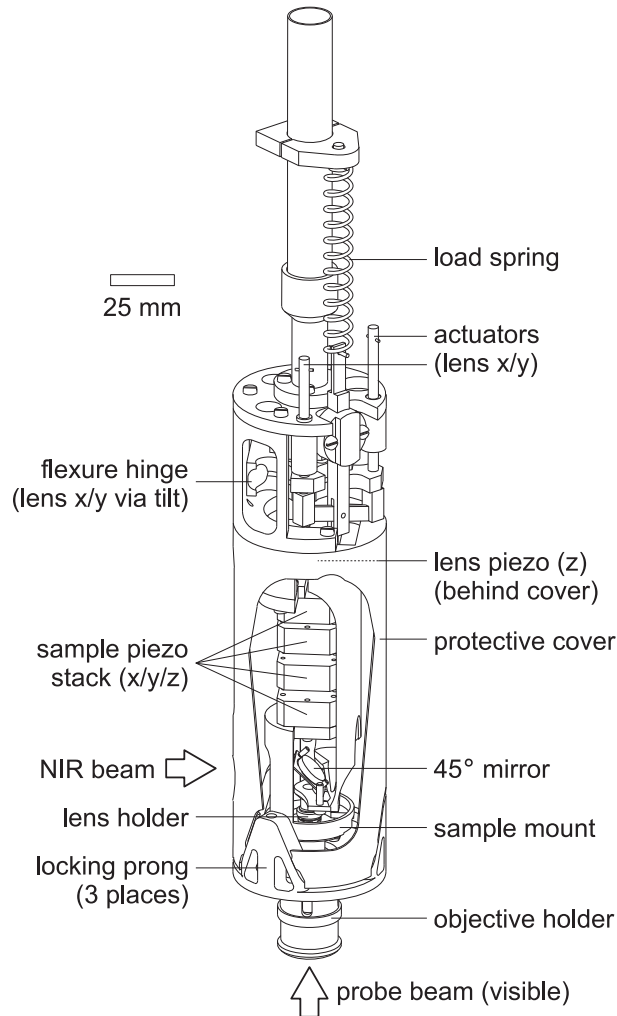


Figure 2.4: Simplified drawing of the bottom of the home-built cryostat insert. The protective cover is “cut open” to show the internal part and the optical elements schematized in Figure 2.1. Sample-holder and objective-holder are separate parts, kinematically self-locked to one another by three prongs. A piezo stack moves the sample mount in three dimensions (x, y, z of sample), and a fourth piezo actuator moves the lens-mirror assembly to focus the NIR laser onto the sample (z of lens). Additionally, two mechanical actuators coarsely control the lens-mirror assembly (x, y of lens). The mechanical movement is effected through a nearly backlash-free bending of two spring-loaded flexure hinges.

2.2 Outside the cryostat

2.2.1 The probing optics

The optical probing part of the temperature-cycle microscope (cf. Figure 2.2) is a laser-scanning confocal microscope. The excitation source is a multi-line argon-ion laser (Spectra-Physics Stabilite 2017), which pumps the NIR laser with 90 % of its output. The remaining 10 % are dispersed in a Pellin-Broca prism (Bernhard Halle, Berlin, Germany), and the 514.5 nm line is selected for excitation. This beam passes a variable attenuator (Newport M925B), a laser-line clean-up filter (Laser Components LCS10-515-F), a combination of a beam expander and a diaphragm to optimize the illumination of the microscope objective, until it reaches a (90/10), (reflection/transmission) beam-splitter (AHF Analysentechnik) which separates the excitation and detection paths. Between the beamsplitter and the cryostat, the beam encounters an automated beam scanner based on two one-axis scan mirrors (Cambridge Technology Inc. 6450 Galvanometer Optical Scanner), a telecentric lens system and a 45 degree mirror to direct the beam through the bottom window of the cryostat.

Starting from the beam-splitter, the detection path includes a spatial filter (two lenses and a 100 μm pinhole). A flip-mirror can be inserted between the pinhole and the second lens for imaging by a color video camera, which helps bring the sample into the focal plane of the microscope objective and to align the pinhole. After the spatial filter, two notch filters (Kaiser Optical Systems HNPF-514.5 and HSPF-785.0), centered at 514.5 and 785 nm, respectively, and two long-pass filters (AHF Analysentechnik HQ525LP and HQ530LP) remove residual laser light. Fluorescence photons are then polarization-selected by a polarizer cube (Linos 33 5641) and detected by two avalanche photodiodes (Perkin-Elmer SPCM-AQR). The setup and data acquisition are computer-controlled with an AdWin-Gold system (Keithley Instruments) and software written in LabVIEW 6.1 (National Instruments).

2.2.2 The heating optics

The heating source (Figure 2.2) at 785 nm is a broad-band Ti:Sa laser (Spectra-Physics 3900S), pumped by the argon-ion laser. The intensity at the sample can reach 75 mW in our current configuration. The laser beam can be switched on and off within 1 μs by an acousto-optical modulator (AOM, AA Opto-Electronic). After the AOM, the NIR light passes a beam expander, a (90/10) beam splitter (AHF Analysentechnik), and is directed to the cryostat side-window by a telescope consisting of two mirrors and two lenses. The bottom

mirror acts as a manual scan mirror and the top mirror can be tilted to center the beam on the aspheric singlet lens (cf. Figure 2.1). The NIR focus on the metal film is monitored by a color video camera that receives 10 % of the back-reflected NIR light.

2.3 Imaging properties

To successfully perform temperature-cycle microscopy of single-molecule dynamics, we have to be able to detect the fluorescence of individual molecules at cryogenic temperatures. Since the single-molecule systems will be fluorophores (either alone or attached to a biomolecule) in a water-like environment, we cannot rely exclusively on frequency selection for single-molecule detection but have to resort to spatial selection. This makes the imaging properties of the microscope more critical, because we have to discern a single-molecule signal from the background without any amplification.

First, we characterize the improvement in imaging properties obtained by the use of the custom-made low-temperature microscope objective instead of the best alternative for low-temperature operation, a five-lens microscope objective. Figure 2.5 shows two images of Nile-red soaked latex beads (Molecular Probes) deposited on a 20 mm microscope cover slide at room temperature under air atmosphere. The left image is obtained with a five-lens objective (Edmund Optics DIN standard) that has the same NA and nominal magnification factor as the custom-made ten-lens objective used for the right image. Further experimental details are given in the caption of the figure. Upon analysis we find an average spot size of around 450 nm for the ten-lens low-temperature microscope objective. For the five-lens alternative, the spot size is 600 nm, and the average collected intensity appears to be two to three times lower than for the ten-lens objective. The latter observation is illustrated by cross-sections of the two images. Although our microscope objective constitutes a clear improvement with respect to the five-lens objective, we should point out that it is still considerably poorer than the multi-lens objectives commonly used in room-temperature microscopy. Comparing our low-temperature objective to a multi-lens Olympus microscope objective (NA = 0.95, 100 times), we observe the latter to produce spot sizes of about 350 nm and to have a 3 times higher collection efficiency (data not shown).

We find both the spot size and the collection efficiency of the low-temperature microscope objective to remain constant throughout the whole temperature range between 295 and 4.2 K. We have verified this by recording a series of images of the fluorescent beads at various temperatures. Figure 2.6a shows an

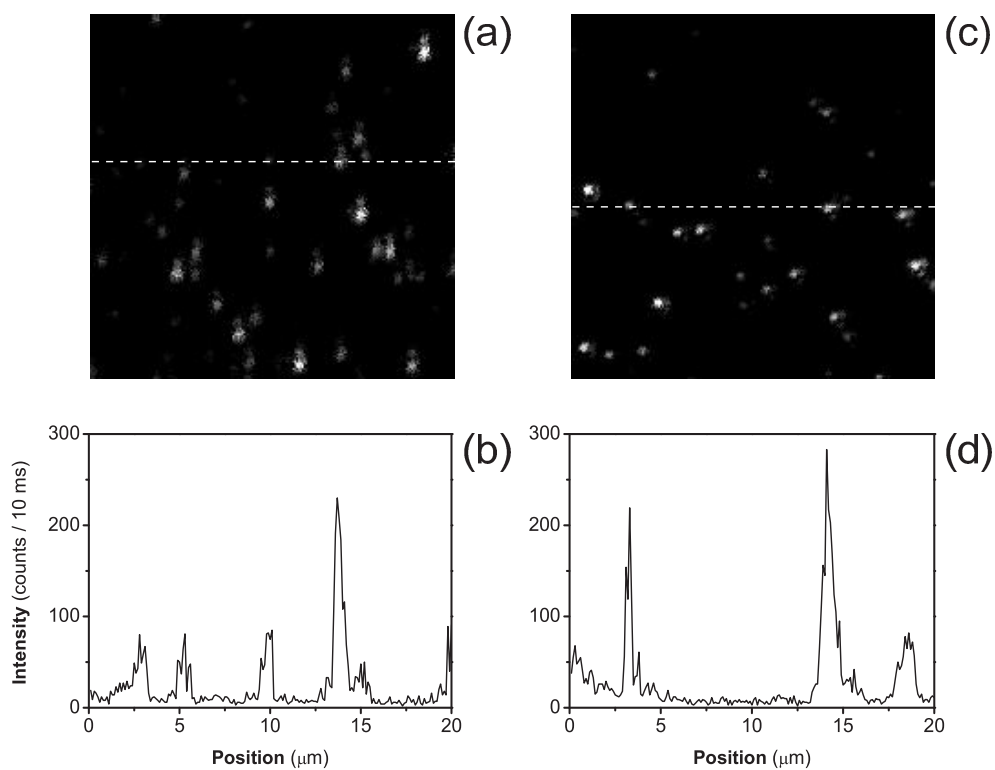


Figure 2.5: Fluorescence images at room temperature: $20 \times 20 \mu\text{m}^2$ laser-scanned confocal images of 20 nm Nile-red soaked latex beads deposited on a BK 7 microscope cover slide excited at 514.5 nm and detected by (a) a five-lens, finite-length corrected (tube length 160 mm) objective (Edmund optics DIN standard, NA = 0.85, 60 times) and (c) the custom-made, infinity-corrected, low-temperature microscope objective (NA = 0.85, 60 times). Diagrams (b) and (d) show cross-sections of images (a) and (c), respectively, at the positions of the dashed white line in each image. The spatial resolution is 100 nm/point and the acquisition time 10 ms/point. The fluorescence intensity is indicated by a linear gray scale between 10 and 400 counts/10 ms. The excitation intensity is 2.5 kW/cm^2 for the five-lens objective and 1.5 kW/cm^2 for the ten-lens one.

image recorded at 41 K.

Figure 2.6 b shows an image of 10^{-9} M perylenedicarboximide (PDI, cf. Figure 6.1 for its structure) in the polymer Zeonex (Zeon Europe, Düsseldorf, Germany) at 150 K. The sample has been prepared by spincoating from an 0.6 wt-% Zeonex in toluene solution yielding a polymer film with a thickness of about 20 nm. The image reveals the presence of bright, nearly diffraction-limited (450 nm) spots. We prove those to be single molecules by record-

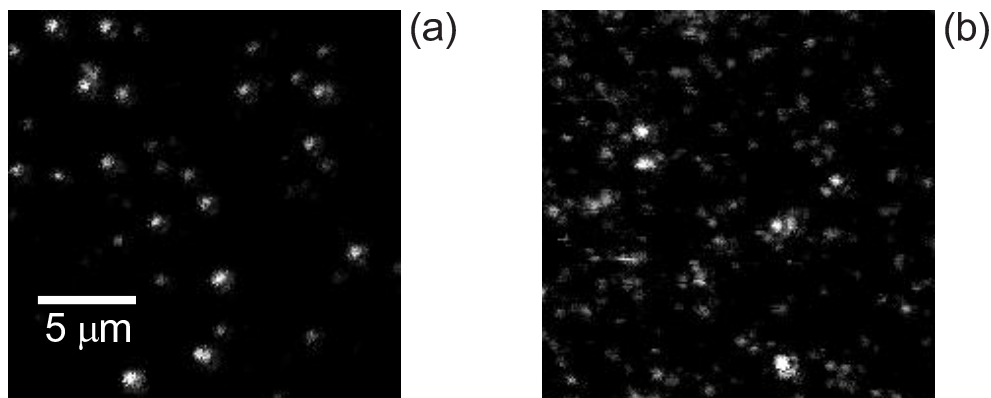


Figure 2.6: Fluorescence images displaying the imaging properties of our microscope at cryogenic temperatures: $20 \times 20 \mu\text{m}^2$ confocal images of (a) 20 nm Nile-red soaked latex beads deposited on a BK 7 microscope cover slide at 41 K and (b) 10^{-9} M PDI in zeonex spincoated on a BK 7 microscope cover slide at 150 K in which the PDI molecules are resolved as individuals. The resolution is 100 nm/point and 10 ms/point in both images. The fluorescence varies on a linear gray scale between 10 and 400 counts/10 ms for the beads and 10 to 150 counts/10 ms for the PDI sample. The excitation intensity is 1.5 kW/cm^2 for the beads and 3 kW/cm^2 for the PDI molecules. In both cases the fluorescence spots are found to have the same size as observed at room temperature, 450 nm.

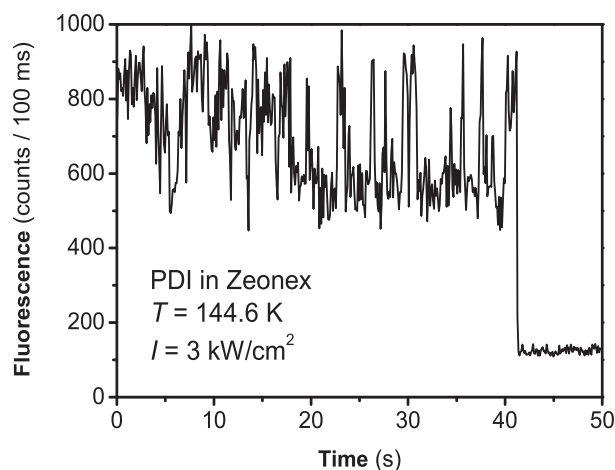


Figure 2.7: Fluorescence time trace of one of the single molecules visible in the image of 10^{-9} M PDI in Zeonex (Figure 2.6 b). The time resolution is 100 ms/point and the excitation intensity 3 kW/cm^2 . The single-step photobleaching event unambiguously proves that the observed fluorescence stemmed from an individual molecule.

ing time traces and observing single-step photobleaching. Figure 2.7 shows a typical example of such a time trace. Finally, we have investigated the reproducibility of our microscope by recording a series of images of fluorescent beads over two days (data not shown). When the temperature is actively stabilized we find a constant drift of about 1 to 2 μm per day in the lateral position of the sample. For its axial position we find comparable stability, so that we should be able to observe single molecules for several hours at any given temperature between 295 and 4.2 K without losing the signal due to mechanical drift.

Acknowledgements

The author wishes to acknowledge the design and construction of the cryostat insert by H. van der Meer and J. A. J. M. Disselhorst, technicians at the Leiden Institute of Physics (LION). He thanks M. van der Aa of Safe Trade BV (Rotterdam, The Netherlands) and Zeon Europe GmbH (Düsseldorf, Germany) for kindly providing 1 kg of Zeonex.

3 Photoblinking of rhodamine 6G in poly(vinyl alcohol)

abstract – We investigate the fluorescence intensity of rhodamine 6G in poly(vinyl alcohol) as a function of excitation intensity, illumination time, the presence of oxygen and temperature. The variations in emissivity (or fluorescence brightness) are attributed to a dark state, which shows populating kinetics resembling those of the triplet state, but a much longer lifetime. We simulate the observed kinetics by a four-level model, in which a long-lived dark state is formed through the triplet as an intermediate state. The weak temperature dependence of the lifetime of the dark state points to electron tunnelling as the main recovery process. This intermolecular mechanism also explains the observed broad distribution of lifetimes. An electron-spin-resonance experiment confirms the assignment of the dark state to a radical. For the first time, photo-induced charge transfer is identified as a source of blinking in single-molecule measurements.

The contents of this chapter have been published:
R. Zondervan, F. Kulzer, S. B. Orlinskii, and M. Orrit, *J. Phys. Chem. A* **107** (2003) 6770–6776.

3.1 Introduction

Single fluorescing quantum systems almost invariably display blinking, i.e., discrete fluctuations of their fluorescence intensity with time [45]. Blinking is generally interpreted as arising from transitions of the fluorophore to a non- or less-fluorescing state, a “dark” or “dim” state, from which it returns to the initial state after some time [4]. If the system does not return to the fluorescing state, the process is called bleaching. If blinking is induced by the excitation light, we call it photoblinking. Photoblinking can be observed in an ensemble experiment, albeit indirectly, because the transitions of all molecules can be synchronized by intensity variations of the excitation laser. High peak intensities and pulsed excitation are usually needed to induce significant photoblinking [46–49], but here we use continuous excitation, shutters and time-resolved detection. Blinking of single fluorophores can be investigated in two ways. From the fluorescence time trace of a single molecule (or single particle) on- and off-times can be determined by defining a threshold between the fluorescent “on”-level and the non- or less-fluorescent “off”-level. The times the molecule is either “on” or “off” provide direct information on the population rate(s) of the involved dark state(s), the recovery rate(s) and the distributions of those rates [50–53]. An alternative method is to measure the fluorescence autocorrelation function, which yields equivalent information without the necessity to define an arbitrary threshold between on- and off-levels [14, 54–57].

For single organic dye molecules, photoblinking is commonly related to excursions of the molecules to the triplet state. Triplet photoblinking is characterized by a succession of relatively short on- and off-times, typically on the order of microseconds to a few milliseconds [1, 2, 50, 52, 53, 55, 58–62]. The off-times are sensitive to the presence of oxygen, which drastically shortens the triplet lifetime [55, 61]. In solid matrices, more complex blinking behaviour has been observed with much longer off-times than expected from a triplet bottleneck (up to minutes) [8, 14, 50–55, 62–70]. Besides the triplet state, other metastable excited states and/or thermally induced changes of the electronic ground state [51, 54] are commonly assumed to be involved. Proposed mechanisms are: i) Photochemical processes such as photoionization followed by electron trapping [63–65, 69], photoisomerization [63] or reversible oxidation by oxygen [69]. ii) Fluorescence quenching by other molecules [52, 63]. iii) Conformational changes of the molecule, which can be either photophysical [50, 70] or thermally induced [51, 54]. iv) Rotation of the molecule [8, 14, 62, 63, 70]. v) Spectral changes induced by the environment of the molecule, either by structure [52, 63] and/or polarity [50] fluctuations of the host matrix, by spatial

heterogeneities in the matrix structure [51,67], or by desorption and reabsorption of the molecule when it is on a surface [8]. In some cases [55,66,68], off-times of approximately 100ms or longer have been interpreted as excursions to the triplet state. As the triplet lifetime of dyes usually does not exceed a few milliseconds in an inert atmosphere, this explanation would require an unlikely large spread or change of this lifetime by several orders of magnitude. Here, we report on the reversible decrease (by up to a factor of 20) of the fluorescence brightness of large ensembles of rhodamine 6G molecules in poly(vinyl alcohol) under continuous-wave excitation. We investigate the influence of excitation intensity, temperature and the presence of oxygen. We develop a model for photoblinking along with the description of our results and draw conclusions on the nature of the dark state involved and on the consequences of the long off-times for single-molecule microscopy.

3.2 Experimental

The system under investigation is the ionic dye rhodamine 6G (R6G, cf. Figure 3.1) in solid poly(vinyl alcohol) (PVA). A solution of R6G (Radiant Dyes laser grade with counter-ion BF_4^-) in methanol (HPLC-grade) is added to a 1 wt-% solution of PVA (MW = 1.25×10^5 g/mol) in 1:1 methanol-water such that the concentration of R6G is 2.0×10^{-5} M with respect to the volume of the PVA. This solution is spin-coated on a fused-quartz plate, which is used because of its low fluorescence background. The sample is characterized by measuring the absorption spectrum on a commercial absorption spectrometer (Perkin-Elmer Lambda 16) and fluorescence spectra at various concentrations with an Acton 500i spectrograph equipped with a back-illuminated CCD camera (Princeton Instruments Spec-10:400B) (spectrum shown in Figure 3.3). From

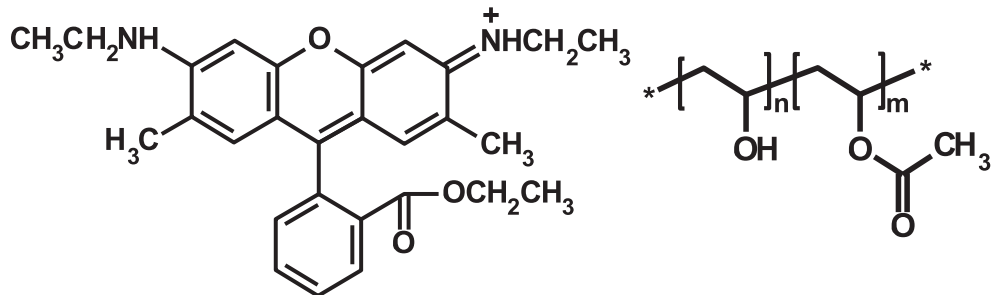


Figure 3.1: The structures of rhodamine 6G and poly(vinyl alcohol).

the absorption spectrum, we obtain the absorption cross-section of R6G in PVA, $(3.0 \pm 0.3) \text{ \AA}^2$ at 514.5 nm.

The experiments on the fluorescence dynamics are performed in a flow cryostat (Leybold Heraeus) to control the atmosphere (air, nitrogen or helium) and the temperature. Nitrogen and helium are obtained from evaporation of, respectively, liquid nitrogen and helium. The air is retrieved from a pressurized air supply with a constant relative humidity of approximately 15%. At room temperature, the experiments are performed under continuous flow. At low temperatures, the cryostat is filled with the desired atmosphere. The temperature is varied between 295 K and 10 K.

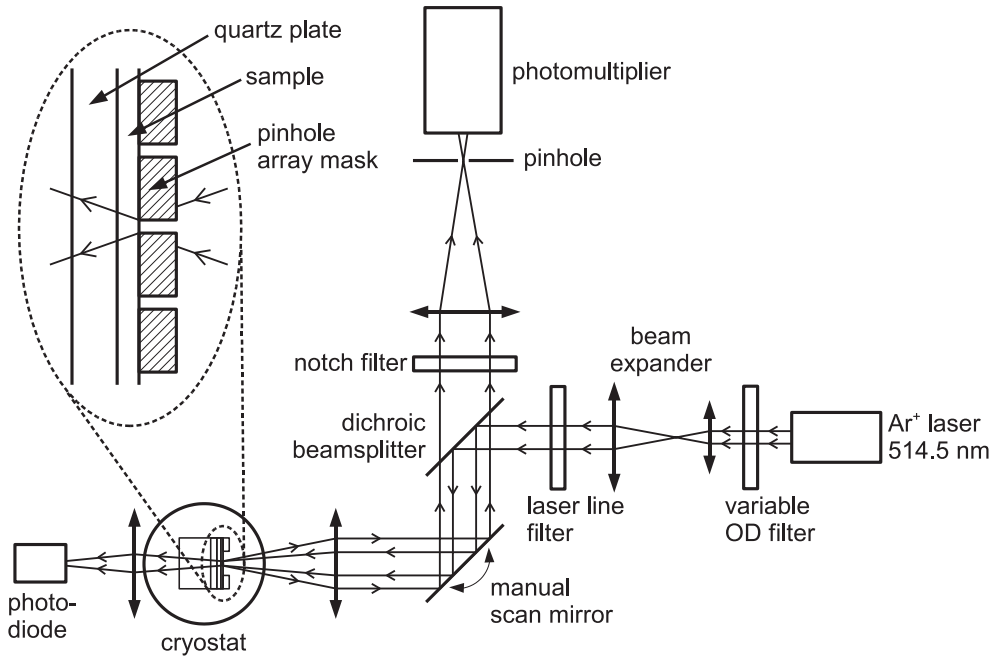


Figure 3.2: Schematic drawing of the optical setup for quantitative ensemble analysis of photoblinking and photobleaching. The inset shows the sample plate with the pinhole array mask. The description of all the parts can be found in the text.

The optical setup is shown in Figure 3.2. It resembles a low-resolution confocal microscope. The system is excited with the 514.5 nm line of an argon-ion laser (Spectra-Physics Stabilite 2017), whose intensity is tuned by a Newport M925B variable attenuator. The excitation beam passes an optical shutter (Uniblitz, Vincent Associates), a beam expander (1:4) and a laser-line clean-up filter (Laser Components LCS10-515-F). The excitation beam is focused by

an achromatic lens with a focal length of 80 mm, which also serves to collect the fluorescence. The excitation and fluorescence photons are separated by a dichroic beamsplitter (AHF Analysentechnik HQ530LP) and in the detection path an additional notch-filter centered at 514.5 nm (Kaiser Optical Systems HNPF-514.5) suppresses residual excitation light. A spatial filter consisting of a lens with a focal length of 250 mm and a 150 μm pinhole further selects the fluorescence from the excitation spot. The fluorescence is monitored with a digital photomultiplier tube, EMI 9558AM 20143, the output pulses of which are discriminated (EG&G Parc model 1182) and fed into a TTL counter input of the control electronics (ADWin-Gold from Keithley Instruments). The excitation light transmitted through the sample holder is detected by a Hamamatsu S2386-45K photodiode for normalization.

For a quantitative analysis of fluorescence time traces, all molecules should experience (as far as possible) the same laser intensity. If the sample dimensions do not exceed the center of the beam by more than half the full-width at half-maximum (fwhm) of the Gaussian spot, the intensity variation across the sample is less than 15 %. To restrict the sample dimensions, we cover it with a pinhole-array mask of stainless steel (10×10 laser-drilled holes, manufactured in the Laser Centre of Loughborough College, UK). The holes are separated by 240 μm (center to center) and have a diameter of 40 μm . An excitation spot with a fwhm of approximately 80 μm on the sample is obtained by slightly defocusing the beam expander. The holes can be addressed individually by means of a manual scan mirror. The sample configuration is shown schematically in Figure 3.2.

In order to directly compare time traces recorded at different excitation intensities, we normalize the measured fluorescence intensity by the excitation intensity. This normalized quantity is defined as the emissivity of the ensemble. Moreover, because the area of the holes and the thickness of the polymer film may fluctuate, we normalize this emissivity to the one measured at the same hole at 65 mW/cm^2 , the lowest intensity for which fluorescence can be measured with satisfactory signal-to-noise ratio.

In this chapter, we present the results of three types of optical experiments. First, the decay kinetics of the fluorescence of R6G in PVA are studied by monitoring the emissivity as a function of the illumination time. Excitation intensities between 65 mW/cm^2 and 320 W/cm^2 are applied and the time resolution varies from 1 to 100 milliseconds. Second, the steady-state fluorescence level is determined. In this experiment, the observation time is in general limited by photobleaching. Third, we study the recovery kinetics of the emissivity after illumination, by applying a high excitation intensity during a short

interval, typically 100 ms, then “instantaneously” reducing it to a lower value by means of an acousto-optical modulator (Quantum Technology 305).

In order to check the proposed hypothesis of light-induced radical formation, we perform an electron-spin-resonance (ESR) experiment with a pulsed ESR spectrometer developed in our laboratory and operating at a microwave frequency of 95 GHz (W-band) [71]. In a pulsed ESR experiment, resonances between the magnetic sublevels of an electron spin and the microwave field are detected via the intensity of an electron-spin echo (ESE) [72].

3.3 Results and discussion

Figure 3.3 shows the absorption spectrum of 10^{-4} M R6G in PVA and fluorescence spectra at three different concentrations, from 10^{-3} to 10^{-5} M. The fluorescence spectra resemble the mirror image of the absorption spectrum, which suggests that the fluorescence arises from isolated dye molecules. Nevertheless, upon a closer look, the spectrum at 10^{-3} M appears to be slightly red-shifted with respect to the other two, which we attribute to the onset of Förster resonance energy transfer (FRET) between the R6G molecules. The characteristic distance for FRET is given by the Förster radius, which for two

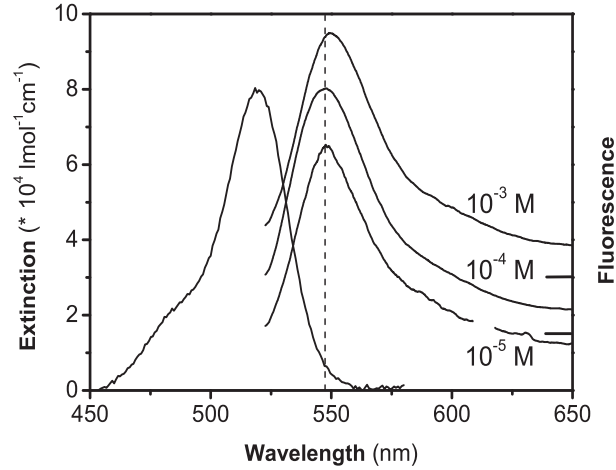


Figure 3.3: Absorption spectrum (on the left) and fluorescence spectra at various concentrations (on the right) of rhodamine 6G in poly(vinyl alcohol). A vertical offset between the fluorescence spectra is introduced for clarity. In the fluorescence spectrum at 10^{-5} M, a Raman line from the PVA matrix at 620 nm has been removed. The dashed line indicates the maximum of the fluorescence spectra at 10^{-4} and 10^{-5} M as a guide to the eye. The maximum at 10^{-3} M is slightly red-shifted.

R6G molecules is approximately 5 nm [73]. Assuming the R6G molecules to be randomly distributed in the sample, we can calculate the percentage of R6G molecules within 5 nm from one another [74]. For a concentration of 10^{-3} M, 27% of the R6G molecules have a neighbor within the Förster radius. At 10^{-4} M, this fraction becomes 3%, and we expect FRET to become negligible. Indeed, comparing the two low-concentration spectra of Figure 3.3, we find no shift, as expected for samples consisting of isolated R6G molecules. Although this analysis does not exclude the presence of R6G dimers or aggregates, we may conclude that their contribution to the fluorescence can be ignored. A comparable study [75] of fluorescein (a dye similar to R6G) in PVA also showed that no significant intermolecular effects such as FRET occur at concentrations below 10^{-3} M.

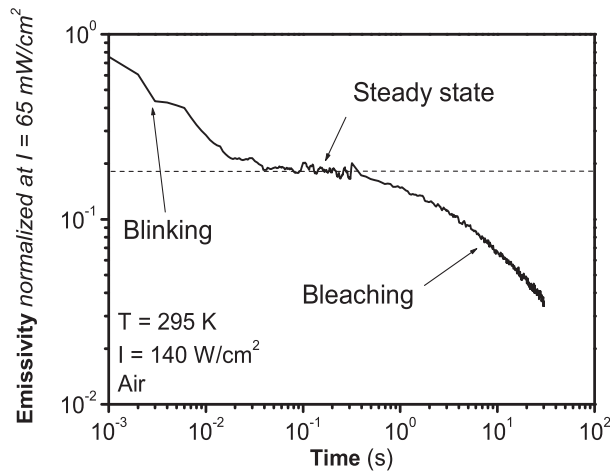


Figure 3.4: A typical emissivity time trace of rhodamine 6G in poly(vinyl alcohol) displaying three different stages in the millisecond to seconds time range. The first part shows a reversible decay of the emissivity related to photoblinking of the individual molecules. In the second part the emissivity reaches a plateau (dashed line), which reflects a steady state of the fluorescent population. The third part corresponds to an irreversible decay of the emissivity caused by photobleaching.

Figure 3.4 shows a typical example of the time dependence of the emissivity of R6G in PVA in the millisecond to seconds time range after unblocking the laser. Three regimes can be distinguished in the trace. First, the emissivity decreases within some tens of milliseconds, then it remains constant for approximately a second before it decreases further. The first decay is reversible. Switching off the excitation light for a few minutes after the emissivity has

reached its plateau (second stage) leads to a complete recovery of its initial level. The reversible decay of the emissivity is related to photo-induced excursions of the molecules to a dark state; in other words, it reflects the photoblinking of the individual molecules. The plateau value of the second stage corresponds to the emissivity of the system in the (intensity dependent) steady state. The decay on the time scale of seconds is irreversible and is due to photobleaching. The separation of the time scales of photoblinking and photobleaching allows us to analyze the photoblinking without having to take bleaching into account. Even at the highest excitation intensity, 320 W/cm^2 , the three stages in the decay of the emissivity are discernible.

3.3.1 Decay kinetics of the emissivity

To a good approximation, the fast reversible decay of the emissivity turns out to be single-exponential for each excitation intensity. Figure 3.5 a displays an example of such a fit. We thus extract an effective decay rate k and evaluate this rate as a function of excitation intensity for various atmospheres and temperatures. Figure 3.5 b shows the variation of k with intensity for air and nitrogen atmosphere at 295 K. Both curves are linear in the range of applied intensities and have the same slope. At lower temperatures, the same decay rates are observed. The single-exponential character of the decay indicates that the dispersion of the response times of the irradiated molecules is less than one order of magnitude. Besides the implications for the system itself, which we will discuss in the following paragraph, it shows that dispersion related to the excitation conditions can be neglected. We conclude that the

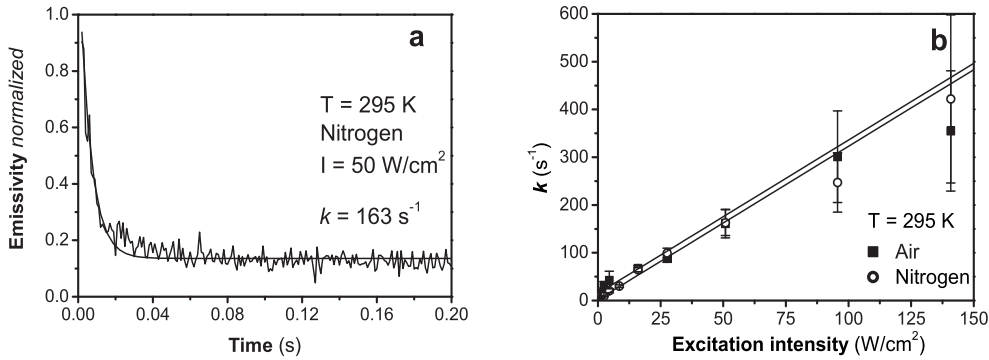


Figure 3.5: (a) Example of a single-exponential fit to a reversible emissivity decay. (b) The effective decay rate k of the emissivity as a function of the excitation intensity in air and nitrogen at 295 K.

presence of the pinhole-array mask (cf. Section 3.2) is sufficient to create a homogeneous excitation profile over the illuminated sample. Furthermore, the dispersion arising from the random orientations of the chromophores with respect to the linearly polarized excitation light can be disregarded. A similar conclusion was reached earlier in hole-burning studies [76, 77].

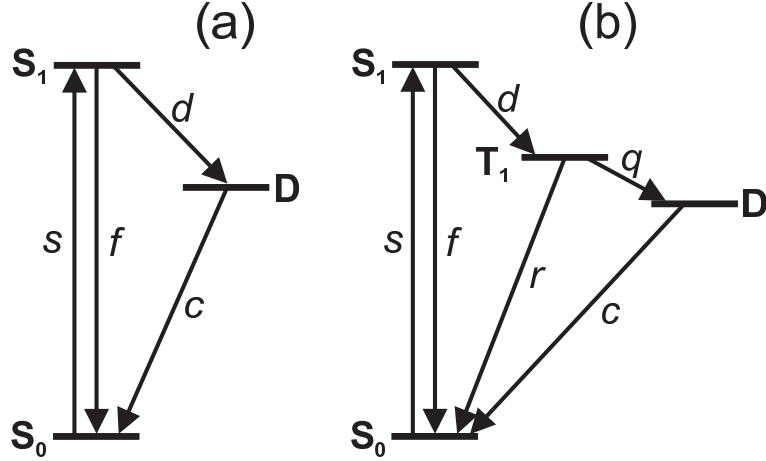


Figure 3.6: (a) Schematic energy-level diagram of a three-level system, consisting of the electronic ground state (S_0), the first excited singlet state (S_1) of rhodamine 6G and an a priori unspecified dark state (D). The symbols along the arrows refer to the rate constants of the respective transitions. (b) Same scheme for a four-level system consisting, besides the two singlet states (S_0 and S_1), of the lowest triplet state (T_1) of rhodamine 6G and of another dark state (D) populated through T_1 .

To interpret the observed reversible decay, let us first assume the presence of a single dark state. We take three electronic energy levels of R6G into account, the singlet ground state (S_0), the first excited singlet state (S_1) and a dark state (D) of an a priori unspecified nature. Figure 3.6 a presents the corresponding schematic energy-level diagram with the relevant transition rates, s , f , d and c . At intensities much below saturation of the optical two-level system (S_0 - S_1), the pump rate s may be written:

$$s = \sigma NI \quad (3.1)$$

where σ is the absorption cross-section of R6G in PVA, $3.0 \times 10^{-16} \text{ cm}^2$, at 514.5 nm, N the number of photons in 1 J at 514.5 nm (2.59×10^{18} photons/J) and I the excitation intensity (in W/cm^2). The fluorescence decay rate f equals $2.5 \times 10^8 \text{ s}^{-1}$ [46]. From the kinetic equations for the respective populations, we obtain the emissivity Φ_{3LS} of the three-level system, which is

proportional to N_{S_1} , the population of S_1 :

$$\Phi_{3LS} = \frac{\eta}{I} N_{S_1} \quad (3.2)$$

with η the fluorescence quantum yield of R6G. In the three-level system there are two timescales, a fast one on the order of nanoseconds (related to the fluorescence decay rate f) and a slow one (related to the build-up of population in D, i.e., to c and d). With our time resolution we only observe the kinetics related to D, which means that the population of S_1 instantaneously adapts to changes in D. Consequently, we may use the so-called intermediate-state approximation and put the time-derivative of N_{S_1} to zero in the system of kinetic equations. Under the assumption that f is considerably larger than d , we obtain for the emissivity Φ_{3LS} :

$$\Phi_{3LS}(s, t) = A_{3LS} + B_{3LS} \exp(-k_{3LS}t) \quad (3.3)$$

with

$$A_{3LS} = \frac{\sigma N \eta}{f} \left(1 + \frac{s}{f} \left(1 + \frac{d}{c} \right) \right)^{-1} \quad (3.4)$$

$$B_{3LS} = A_{3LS} P_{2LS} \frac{d}{c} \quad (3.5)$$

$$k_{3LS} = P_{2LS} d + c \quad (3.6)$$

$$P_{2LS} = \frac{s}{f + s} \quad (3.7)$$

The rate k_{3LS} (3.6) is the effective decay rate in this three-level model. As the reversible decay is found to be single-exponential, k_{3LS} is not dispersed and reflects a single value of the population rate d (because c is negligible in the applied intensity range, cf. Figure 3.5 b). Applying the expression for k_{3LS} to fit the curves in Figure 3.5 b, we obtain a value of approximately $1.0 \times 10^6 \text{ s}^{-1}$ for d . The fact that d is independent of atmosphere and temperature suggests that we are dealing with the inter-system crossing (ISC) rate from S_1 to the lowest triplet state (T_1). In principle, the ISC rate of R6G can be enhanced by the presence of oxygen depending on the S_1 - T_1 gap, but this effect is negligible at the oxygen concentration of air [78]. The value of d is indeed in reasonable agreement with the ISC rates of R6G reported in the literature, which are in the range of 4.0×10^5 to $6.0 \times 10^5 \text{ s}^{-1}$ [46, 47]. The discrepancy is most likely due to the inherent uncertainty in the determination of the absolute intensity which is used to calculate s in Equation (3.1).

For vanishing intensity, the decay rate k_{3LS} tends to c , the recovery rate from the dark state. If the dark state was T_1 , cf. Figure 3.6 a, the reported triplet lifetimes of about 400 μs (rate = $2.5 \times 10^3 \text{ s}^{-1}$) in an inert atmosphere [46] and of about 4 μs (rate = $2.5 \times 10^5 \text{ s}^{-1}$) in air (value for R6G in ethanol) [59] would lead to much higher rates than measured. Therefore, the low values of the decay rate (on the order of 10 s^{-1} at low intensity) indicate that the triplet state cannot be solely responsible for the observed photobleaching. Another dark state with longer lifetime has to be involved, as our discussion of the steady-state emissivity in the next section will also show.

3.3.2 Steady-state emissivity

Figure 3.7 shows the steady-state emissivity, deduced from the plateau between the reversible decay and the photobleaching (cf. Figure 3.4), as a function of excitation intensity in air and nitrogen atmosphere at room temperature. The normalized steady-state emissivity drops by a factor of up to 5 in air and 10 in nitrogen at high intensity. The steady-state emissivity in helium atmosphere at 295 K displays the same intensity dependence as in nitrogen. Figure 3.8 presents the steady-state emissivity as a function of excitation intensity at

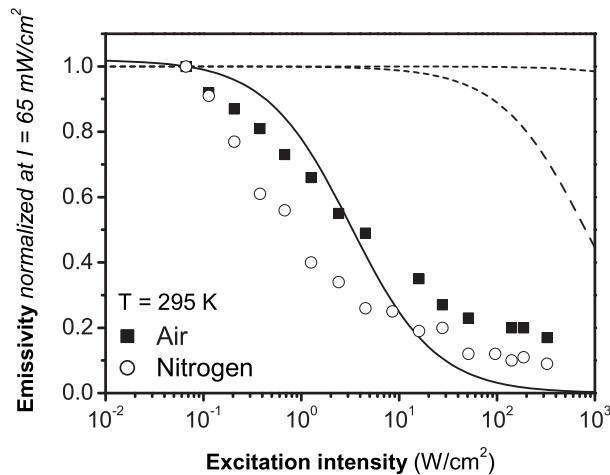


Figure 3.7: Steady-state emissivity of rhodamine 6G in poly(vinyl alcohol) as a function of excitation intensity in air and nitrogen atmosphere at room temperature. The dashed lines are simulations of the steady-state emissivity in the three-level model with the rates associated to the triplet state [46, 59] in nitrogen (lower trace) and air (upper trace). The solid curve is a simulation for the three-level system with a lower recovery rate $c = 10 \text{ s}^{-1}$ of the dark state.

various temperatures down to 10 K. At the lowest temperature the normalized steady-state emissivity decreases by a factor of up to 20 at high intensity. The influence of the temperature seems to be smaller than that of oxygen. The main emissivity changes occur between 295 and 80 K, as the data at 80 and 10 K are nearly indistinguishable.

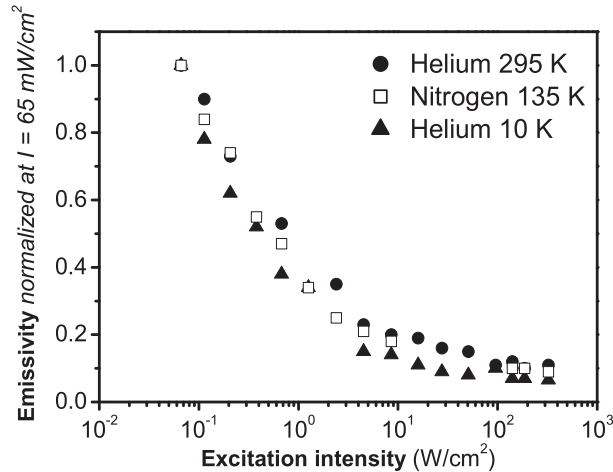


Figure 3.8: Steady-state emissivity as a function of excitation intensity at various temperatures in inert atmosphere. The plot at 10 K is indistinguishable within experimental error from that at 80 K (not shown).

For the three-level system the steady-state emissivity is equal to A_{3LS} (3.4). The normalized steady-state emissivity Ψ_{3LS} is given by:

$$\Psi_{3LS}(s) = \frac{A_{3LS}(s)}{A_{3LS}(s_0)} \quad (3.8)$$

where s_0 represents the pump rate at $I = 65 \text{ mW/cm}^2$. Figure 6 shows simulations of the normalized steady-state emissivity Ψ_{3LS} with the published triplet lifetimes [46, 59] in nitrogen and air at room temperature. These simulations strongly disagree with the experimental data, which confirms our earlier conclusion that the triplet is not the only dark state involved in the photoblinking. To account for our data, we now consider a four-level system, in which T_1 is the intermediate state between S_1 and another dark state D , as illustrated in the energy-level diagram of Figure 3.6 b. In this model, D has the lower energy of the two dark states, as its lifetime apparently determines the recovery, and T_1 is involved as the doorway state, because the effective population rate of D is found to be roughly equal to the ISC rate of R6G. In other words, ISC is

the rate-limiting step in the formation of D, from which we conclude that q is larger than d . Realizing that r is on the order of d in air and even smaller in an inert atmosphere, there will be no build-up of steady-state population in T_1 . As a result, the system (cf. Figure 3.6 b) is expected to effectively reduce to a three-level system (Figure 3.6 a), and the corresponding expressions (3.3) to (3.8) can be applied, with a new value of c .

The expression describing the time dependence of the emissivity Φ_{4LS} of the proposed four-level system is found from the corresponding rate equations applying the intermediate-state approximation for the rate equations related to both S_1 and T_1 . This is justified for T_1 , since the lifetime of T_1 is much smaller than that of D. Neglecting d with respect to f , we obtain:

$$\Phi_{4LS}(s, t) = A_{4LS} + B_{4LS} \exp(-k_{4LS}t) \quad (3.9)$$

with

$$A_{4LS} = \frac{\sigma N \eta}{f} \left(1 + \frac{s}{f} \left(1 + \frac{d(q+c)}{c(q+r)} \right) \right)^{-1} \quad (3.10)$$

$$B_{4LS} = A_{4LS} P_{3LS} \frac{dq}{c(q+r)} \quad (3.11)$$

$$k_{4LS} = P_{3LS} d + c \quad (3.12)$$

$$P_{3LS} = \frac{s}{f + s \left(1 + \frac{d}{q+r} \right)} \quad (3.13)$$

For q much larger than r and d , (3.10), (3.11) and (3.13) reduce to the corresponding equations for the three-level system, (3.4), (3.5) and (3.7). The effective decay rate is indeed given by (3.6) where c is now the recovery rate from the long-lived dark state D, and the normalized steady-state emissivity is again given by (3.8).

Figure 3.7 shows a simulation of the normalized steady-state emissivity with $c = 10 \text{ s}^{-1}$. The observed steady-state emissivity decays more slowly than the simulation. The discrepancy between data and model is significant. The experimental points are quite reproducible, as indicated by their limited scattering. We assign this deviation to a distribution of c values. Since the deviation extends over 3 decades of intensity at least, the distribution has to be broad. Several analytical expressions for the rate distribution may fit our data within the experimental accuracy. We obtain a satisfactory agreement with a

power-law distribution of c between c_1 and infinity, which involves only two parameters, the exponent α and the cutoff c_1 :

$$p(c) = \frac{\alpha}{c_1} \left(\frac{c_1}{c}\right)^\alpha \quad \text{with property } \int_{c_1}^{\infty} p(c)dc = 1 \quad (3.14)$$

After introducing this distribution, the normalized steady-state emissivity becomes:

$$\Psi'(s) = \frac{\int_{c_1}^{\infty} p(c)A_{3LS}(s)dc}{\int_{c_1}^{\infty} p(c)A_{3LS}(s_0)dc} \quad (3.15)$$

with two fit parameters, c_1 and α .

In order to fit the steady-state curves, we have to assume that 5% of the molecules do not go into D at all ($q = 0$). The fits of three typical steady-state curves are presented in Figure 3.9 a, for air and nitrogen at 295 K and for helium at 80 K. Figure 3.9 b shows the distributions of c applied in these fits. The lifetime of D ($1/c$) is shorter in air than in inert atmosphere, and it lengthens when the temperature decreases. The apparent narrowing of the distributions for inert atmosphere and low temperature (cf. Figure 3.9 b) with respect to that for air is probably related to experimental constraints on the value of the cut-off rate c_1 . For the first two, the respective distributions may cover rates smaller than 0.1 s^{-1} , the smallest deducible recovery rate under our experimental conditions, while for air our experimental window allows us to observe the full range of rates.

3.3.3 Recovery of the emissivity

As an independent test of our model, we verify that it correctly accounts for the recovery kinetics of the emissivity. We measure these kinetics by applying an AOM to switch “instantaneously” between high and low intensities. Figure 3.10 shows the results in air and nitrogen at room temperature and in helium at 80 K. The signal-to-noise ratio is rather poor because the light intensity is chosen as low as possible to get as close as possible to the ideal recovery, in the dark. With the parameters obtained from the steady-state curves (cf. Figures 3.9 a and 3.9 b), the recovery traces are simulated satisfactorily, as the solid lines in Figure 3.10 show.

3.3.4 The nature of the dark state

First, we argue that the ambient relative humidity does not affect our experiments. In a recent paper, Hou and Higgins [70] point out that humidity may

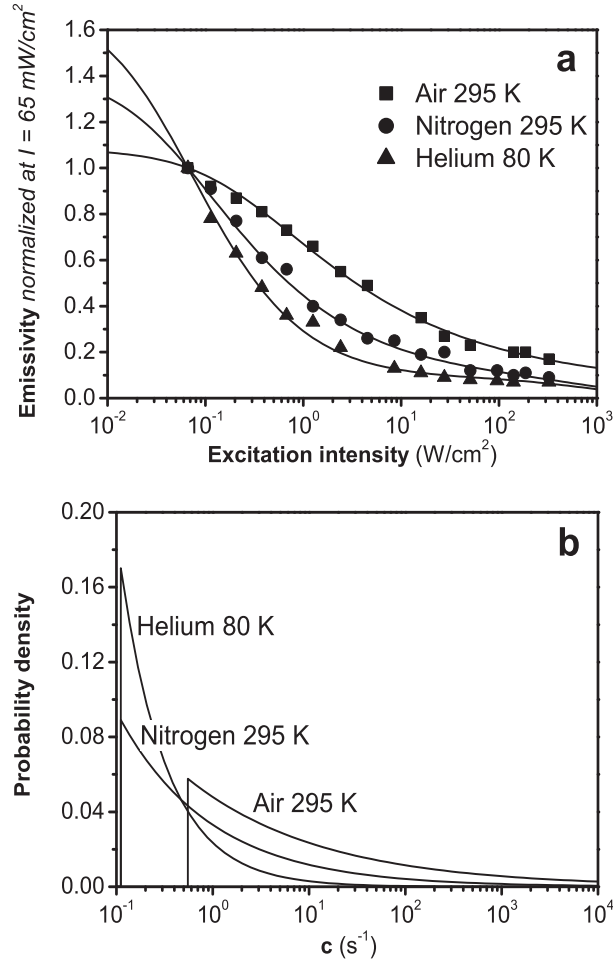


Figure 3.9: (a) Fits of three representative curves of the steady-state emissivity as a function of the excitation intensity. In these fits, the parameter c is described by power-law distributions as indicated in b. For all three fits, we suppose that 5% of the population has only T_1 as dark state. (b) Graphic representations of the applied power-law distributions of c to fit the steady-state curves as shown in a. The values of the fit parameters are: in air at room temperature $c_1 = 0.5 \text{ s}^{-1}$ and $\alpha = 0.31$, in nitrogen at room temperature $c_1 = 0.1 \text{ s}^{-1}$ and $\alpha = 0.45$, and in helium at 80 K $c_1 = 0.1 \text{ s}^{-1}$ and $\alpha = 0.90$.

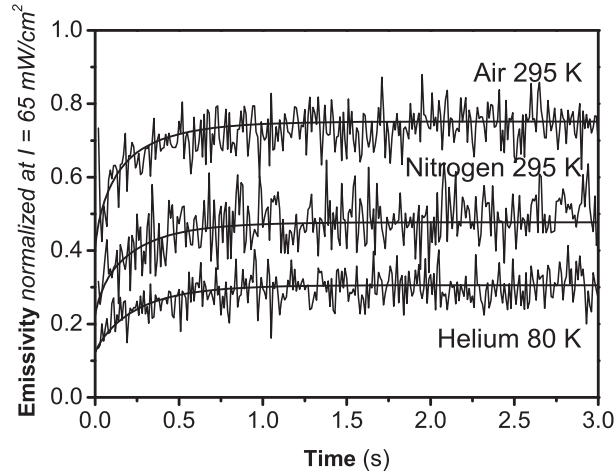
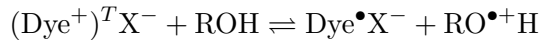


Figure 3.10: Recovery traces recorded in air at room temperature by switching from 8.0 to 0.6 W/cm² (upper trace), in nitrogen at room temperature by switching from 8.0 to 0.8 W/cm² (middle trace) and in helium at 80 K by switching from 8.0 to 0.9 W/cm² (lower trace). The solid lines are simulations with the parameters obtained from the fits of the steady-state curves (cf. Figures 3.9 a and 3.9 b).

affect the blinking of a dye incorporated in a hydrophilic matrix like PVA. The air we use has a relative humidity of 15 %, i.e., well below 30 %, the threshold above which Hou and Higgins observed significant effects on blinking.

The dark state might arise from photo-induced intramolecular rearrangement, such as the formation of a twisted intramolecular charge-transfer (TICT) state. However, R6G is a reputedly stable laser dye, which to our knowledge has never been reported to undergo intramolecular photochemistry in alcoholic solution under our excitation conditions [46, 47]. Furthermore, intramolecular rearrangement is not expected to occur in PVA under our experimental conditions because of its high rigidity at low relative humidity [70]. Remarkably, the recovery process has no activation barrier, since the lifetime of D is hardly sensitive to temperature. This once more excludes intramolecular rearrangement and all processes involving molecular diffusion of R6G or other species and most intermolecular chemical reactions involving significant rearrangements of atoms. Proton transfer is known to occur at low temperatures via tunneling, but it is usually drastically accelerated by thermal activation at room temperature. These arguments leave intermolecular electron tunneling as the most likely process for the recovery of the dark state. We are naturally led to assume that dark state D is a radical formed by intermolecular electron transfer. The family of the rhodamine dyes is known to be able to form both

cationic and anionic radicals [47, 79, 80]. Since PVA has no electron-acceptor sites and the cation of R6G is not stable in an alcoholic environment [47], we suppose that an electron is transferred from PVA to R6G in the lowest triplet state leading to the formation of the radical anion of R6G (see below). In order to emphasize the ionic character of R6G we write Dye^+X^- :



To check whether the dark state D is indeed a radical, we perform an ESR experiment. Figure 3.11 shows the ESE-detected ESR spectrum of 10^{-4} M R6G in PVA at 1.5 K with and without continuous optical excitation with the green and yellow lines (546.1 and 577.0 nm) of a 100 W mercury arc. Upon illumination, a single ESR line arises at a magnetic field corresponding to $g = 2.00215 \pm 0.0001$, with a width of about 5 mT. This is the signal of a radical with $S = \frac{1}{2}$. The small deviation of the g-factor from that of a free electron ($g = 2.00232$), approximately 0.1 mT, indicates a weak spin-orbit interaction [72, 81]. This ESR line cannot stem from the triplet state of the molecule for two reasons. First, the short triplet lifetime would not allow its detection under continuous optical excitation. Second, zero-field splittings of triplet states are on the order of a few tens of mT [82], which would yield a much broader ESR line with a different lineshape. The ESE intensity is proportional to the number of electron spins and should therefore reflect the population of D. Under continuous irradiation, the ESE intensity increases with time and reaches a steady state after approximately 15 minutes (data not shown). This long rise-time is due to the low intensity of the mercury arc, about $1 \text{ mW}/\text{cm}^2$, i.e., much lower than the intensity of the laser used in the optical experiments. When the light is switched off, the ESE signal decays back to zero, which corresponds to the recovery of the ground state of R6G. Under the same conditions no ESR signal is observed for a PVA film without R6G.

The dark state D is thus a radical pair, which reverts to S_0 by electron tunneling. To understand the distribution of the lifetimes of D, the nature of the tunneling process has to be considered. The tunneling rate mainly depends on the overlap between the wave functions of the excess electron on R6G and the hole on the PVA and therefore depends exponentially on their distance. A distribution of distances between the dye and the electron-donor site in the polymer matrix is thus expected to lead to a very broad distribution of lifetimes for D. The role of oxygen can also be understood, as oxygen may assist the recovery as an electron carrier [46, 47], which would explain the observed decrease of the lifetime of D in air.

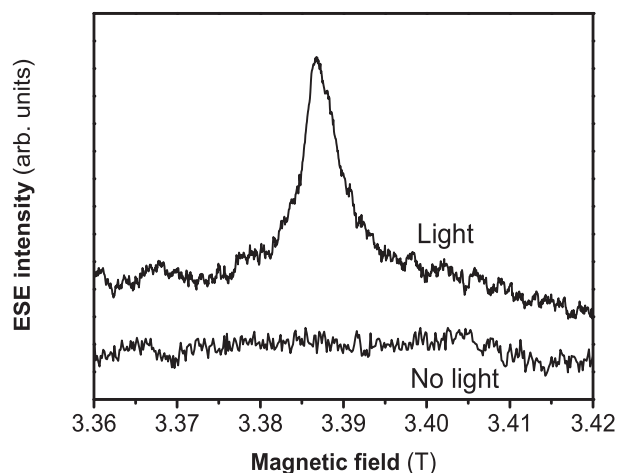


Figure 3.11: W-band (95 GHz) ESE-detected ESR spectra of rhodamine 6G in poly(vinyl alcohol) with (upper trace) and without (lower trace) continuous irradiation of light. The position of the resonance in the upper spectrum corresponds to the expected field for a radical.

Photoblinking processes reported earlier in the literature may also be explained by our model. Hernando *et al.* [83] report long off-time photoblinking (100 ms or more) of a similar rhodamine dye (TRITC, tetramethyl-rhodamine-5-isothiocyanate) incorporated in PVA, which seems to be the same process we have found in R6G. In other polymers, R6G also shows long off-time blinking, for instance in poly(methyl methacrylate) [69], a polar but hydrophobic polymer.

The formation of the radical anion of R6G from the lowest triplet state has also been observed in ethanol at room temperature [46,47], but with a shorter time of formation (a few milliseconds) and a higher stability of the radical, which was only affected by oxygen. The initial electron transfer to the triplet state of R6G should be equally fast in both matrices, so that the differences probably originate from the various possible electron-hole recombination processes. The less efficient radical formation in ethanol may arise from a higher probability of immediate recombination in a fluid compared to solid PVA. The higher stability may result from the escape of the hole from the Coulomb field of the R6G radical. The latter process appears to be negligible in PVA, even at room temperature.

Our four-level model naturally explains why the on-times in photoblinking are related to inter-system crossing, although the off-times are much longer (up to seconds) than the lifetime of the triplet state. Several authors [55,66,68] have

attributed such long off-times to the triplet state. Our study rather suggests that, in many cases, the triplet state is merely the intermediate leading to a long-lived charge-separated dark state. If the temperature dependence of the off-times is weak, charge separation and recovery by tunneling are likely.

3.4 Conclusion

We have studied the photoblinking of R6G in PVA on large ensembles of molecules with continuous-wave excitation. We have measured the decay and recovery kinetics as well as the steady-state of the emissivity. We have simulated our results with a kinetic model where the triplet of R6G is the intermediate between the first excited singlet state and another dark state. Because of the very weak temperature dependence of the lifetime of this dark state, we were led to assign its decay to electron tunneling. Consequently, the dark state must be a radical, which was confirmed by the observation of a light-induced ESR line at the resonant field of a free electron. We also found a broad distribution of dark-state lifetimes, which is compatible with electron tunneling in a disordered solid matrix. Charge transfer from an excited state may be a mechanism of photoblinking that could occur in many dye-matrix couples besides R6G in PVA, in particular when off-times are longer than expected for a triplet state.

Our ensemble observations of a broad distribution of lifetimes associated to a dark state do not allow us to distinguish between two cases on the single-molecule level. First, different populations of “bright” and “dark” molecules may arise, of which the ones displaying long off-times are not expected to be observed under single-molecule conditions. Second, “bright” and “dark” periods may occur in the fluorescence time trace of each individual molecule. This case resembles the photoblinking dynamics of individual semiconductor nanocrystals. In this sense, it is interesting to compare for R6G in PVA the results of single-molecule experiments with the present ensemble results which will be done in Chapter 4.

Acknowledgements

The author thanks G. Mathies and E. van der Togt for their contributions to the experiments and Dr. S.B. Orlinskii for the measurement of the ESR spectra. He acknowledges helpful discussions with Prof. W.J. Buma and Prof. E. J. J. Groenen.

4 Photobleaching of rhodamine 6G in poly(vinyl alcohol)

abstract – Photobleaching is a severely limiting factor in the optical study of single biomolecules. We investigate photobleaching of rhodamine 6G (R6G) ensembles in poly(vinyl alcohol) (PVA) as a function of illumination time, excitation intensity, the presence of oxygen and temperature. We observe non-exponential kinetics related to primary photobleaching through two dark states, the triplet state and a radical anion, and to secondary photobleaching after optical excitation of those dark states. Reactions of the metastable states with oxygen can either lead to photoproducts or to a recovery of the ground state. Oxygen can therefore enhance or reduce photobleaching, depending on the experimental conditions. At low temperature photobleaching is reduced although not completely suppressed. Despite the presence of the long-lived radical anion, we are able to observe single R6G molecules in PVA. At room temperature only relatively bleaching-resistant molecules are resolved as individuals. At low temperature the observation times become considerably longer. Our study shows that metastable states other than the triplet drastically affect photobleaching.

The contents of this chapter have been published:
R. Zondervan, F. Kulzer, M. A. Kol'chenko, and M. Orrit, *J. Phys. Chem. A* **108** (2004) 1657–1665.

4.1 Introduction

Although hardly any biological molecule intrinsically fluoresces at convenient excitation wavelengths, a biomolecule can be labelled with fluorophore(s) in a controlled manner for optical investigation. The study of biomolecules has become an important application of single-molecule optics especially at room temperature [5–7, 13, 84–88]. However, the time scales and the range of optical experiments on biological systems at room temperature are considerably limited by photobleaching. Bleaching is the irreversible conversion of a fluorescent molecule or particle into a non-fluorescent entity. In most cases this process is photo-induced and hence is called photobleaching. Two circumstances make photobleaching especially detrimental for the optical study of single biomolecules. The first one is working at room temperature. The photobleaching efficiency increases with temperature, because more reaction pathways become activated. The second one is the water(-like) environment required by biomolecules. In aqueous solution, fluorophores are easily attacked by small reactive molecules, such as oxygen or water itself.

The observation times in biological studies can be lengthened by removing oxygen with scavengers [86, 89]. Another option is to use semiconductor quantum dots as labels for biomolecules [17, 90], because they are generally more photostable than organic dyes and auto-fluorescent proteins [91]. Hydrophilic matrices other than water, for instance the polymer poly(vinyl alcohol) (PVA) and sugars such as trehalose, have also been applied as matrices for experiments on single biomolecules [92, 93]. These matrices have the advantage of allowing the incorporation of biomolecules in a rigid structure and in an environment less reactive than water. Nevertheless, the average observation time of single molecules in these matrices at room temperature [93], ten to twenty seconds, is still too short to study slow biological processes like protein folding by following one and the same molecule over the full range of relevant time scales [94]. In this paper we consider rhodamine 6G (R6G) in PVA as a model system to explore photobleaching mechanisms in hydrophilic matrices.

The photobleaching mechanisms of organic dyes are complex and mostly unknown. They probably follow different pathways involving various intermediates. For instance, the photobleaching of Cy5 in water [95] involves at least three metastable intermediates. Some of these bleaching reactions need oxygen, while others require optical excitation of an intermediate. It is therefore difficult to present a general description of photobleaching. A useful way to distinguish photobleaching pathways is to categorize them according to their dependence on experimental parameters. First of all, a given photobleaching pathway proceeds either by direct reaction from an excited state (singlet,

triplet or an other metastable state), or by a “secondary”, photo-induced reaction of one of these states, which thus requires the absorption of one or more additional laser photon(s). In principle, only the “primary” pathway should be observed at low enough intensities. However, the lifetime of dark states is sometimes so long that the two kinds of processes can be difficult to distinguish in practice. A further way to distinguish photobleaching mechanisms is to study the effect of atmosphere and temperature. The multiplicity of photobleaching mechanisms leads to a huge spread in the observation times of single molecules already at room temperature for different compounds and experimental conditions. To give an impression, the bleaching time can reach several hours for terrylene in *para*-terphenyl under an argon atmosphere [96], while it does not exceed some hundreds of milliseconds for tetramethylrhodamine (TMR) attached to DNA at a surface [97].

4.1.1 Primary oxygen-induced photobleaching

At room temperature oxygen is generally regarded as the most important reagent in photobleaching. Oxygen is believed to react in its singlet excited state, itself generated by reaction with the dye’s triplet state. The oxidation mechanisms and products are poorly known. Recently, Christ *et al.* [96] have proposed that some of the photo-oxidation products of single terrylene molecules are peroxides and diepoxides. In most single-molecule experiments in air atmosphere, the observed photobleaching can be attributed to photo-oxidation reactions [61, 70, 96–98]. In ensemble studies this is only the case at low dye concentrations (10^{-5} M and lower) [75, 99–103]. The diffusion constant and solubility of oxygen in the host matrix (the permeability to oxygen) are important factors in the efficiency of photo-oxidation reactions. In the case of PVA, oxygen diffusion is enhanced when water is present in the polymer, softening its structure [67, 70]. As the temperature also affects the rigidity of the polymer, photobleaching can be applied as a probe for the glass transition, as was done for PVA ($T_g = 350$ K) [75, 102, 104].

4.1.2 Primary photobleaching without oxygen

Photo-oxidation is not the only primary photobleaching pathway, since photobleaching is still observed in inert atmosphere [55, 61], in deoxygenated samples [53] or when oxygen scavengers are added [89]. However, the characteristic bleaching times are about 1 to 2 orders of magnitude longer. This photobleaching pathway is believed to proceed through reactions of the triplet state with matrix molecules or with impurities other than oxygen. Such “non-

oxygen-mediated” channels can become equally important as photo-oxidation, and lead to complex bleaching behavior. This has been observed for ensembles [99–103] as well as for single molecules [105, 106] of xanthene dyes, such as fluorescein.

4.1.3 Photobleaching of metastable states

Secondary photobleaching of metastable intermediates dominates the primary processes at high excitation intensities (above 1 MW/cm^2), where excitation of the excited singlet may also occur, but it can already take place at much lower intensities for long-lived metastable states [95]. The highly excited states generated by secondary excitation are very reactive and are therefore particularly prone to photobleaching [105, 107]. For the same reason, photobleaching is also enhanced by two-photon compared to one-photon excitation [108, 109] or when the molecule sees a high infra-red intensity, for example in an optical trap [110]. However, as a further complication, excitation of metastable states such as the triplet can repopulate the singlet state, e.g. by reverse intersystem crossing [111], potentially leading to a reduction of photobleaching.

4.1.4 Photobleaching and temperature

Lowering the temperature leads to a drastic decrease of photobleaching. Most photobleaching processes are chemical reactions which must overcome an activation barrier. The immobilization of reactive molecules such as water at lower temperatures can also further reduce photobleaching. Single terrylene molecules on a surface were shown to survive considerably longer below the freezing point of water [21].

In the previous chapter, we have studied the emissivity of an ensemble of R6G molecules in PVA under optical excitation. We could distinguish two parts in the time-decay: the faster component was reversible, and related to the photoblinking of individual molecules. The second component was irreversible, and related to photobleaching. We have identified the main transient species involved in the photoblinking as the radical anion of R6G, formed through the triplet. This metastable state must be considered in the discussion of the photobleaching of R6G in PVA. Here, we investigate the observed photobleaching kinetics as a function of time, intensity, temperature and the presence of oxygen. We again work with an ensemble, because it directly provides us with the overall photobleaching behavior, while a quantitative single-molecule study would require exhaustive statistics. We observe complex photobleaching be-

havior, which indeed involves the lowest triplet state and the radical anion of R6G. We extend our model of photoblinking to the photobleaching kinetics, and obtain qualitative agreement with the data. We perform single-molecule measurements to compare with the ensemble results. Single molecules can be observed despite the long-lived radical anion. The fluorescence dynamics of the single molecules are in good agreement with the ensemble results.

4.2 Experimental

The sample preparation has been described in Section 3.2. The concentration of R6G in the PVA films is 2.0×10^{-5} M in the ensemble experiments and 1.0×10^{-9} M in the single-molecule experiments. Fused-quartz substrates are used in the ensemble study because of their low fluorescence background, which allows us to observe the long-time “tail” of the photobleaching curves. Glass substrates suffice for the single-molecule experiments, because of the confocal background suppression. For the single-molecule experiments, the 1 wt-% PVA solution is “cleaned” by irradiation for a few hours with a 100 W xenon-arc, the output of which is sent through a water filter to remove the deep ultra-violet and infra-red parts. Furthermore, the single-molecule samples are dried overnight in a vacuum exsiccator. The excitation wavelength (continuous-wave) is 514.5 nm in both experiments.

The ensemble experiments are performed at variable intensity (2.5 to 320 W/cm²), atmosphere (nitrogen, helium or air) and temperature (10 to 295 K) in a set-up described in Section 3.2. As in our photoblinking experiments, we use a pinhole-array mask (prepared in the Laser Centre of Loughborough College, UK) with 10×10 holes of diameter 40 μ m to restrict the dimensions of the illuminated sample and to achieve a homogeneous excitation field over the studied area. To directly compare time traces recorded at different excitation intensities, we always normalize the measured fluorescence intensity to the excitation intensity. This normalized quantity is defined as the *emissivity* of the ensemble, which is in turn normalized to the emissivity of the given hole at 65 mW/cm² (to correct for slight differences in the area of the holes). To obtain the complete emissivity decay trace due to photobleaching at a given intensity, a trace with a high temporal resolution (1 to 100 ms, depending on the excitation intensity), and a short duration (up to 30 s after unblocking the laser) is combined with a low-resolution (2 s), long time trace (30 to 5 000 - 80 000 s after unblocking the laser).

The single-molecule experiments are performed at 295 K in air and nitrogen atmospheres and in liquid helium at 1.5 K with the home-built laser-scanning

confocal microscope of reference [112]. To the original set-up, we have added an optical shutter (Uniblitz, Vincent Associates), a laser-line clean-up filter (Laser Components LCS10-515-F), a dichroic beam splitter (AHF Analysentechnik HQ530LP) to separate the excitation and detection light, and in the detection path a spatial filter and a notch-filter centered on 514.5 nm (Kaiser Optical Systems HNPF-514.5). The detection and excitation are performed through an objective with a focal length of 2.45 mm and a numerical aperture of 0.9. The objective is placed in the cryostat and its focal spot has a full-width at half-maximum of approximately 600 nm.

The experiment is controlled by an ADWin-based system (Keithley Instruments), with which we can automatically position molecules in the excitation focus, while minimizing their exposition to the laser before recording time traces. From such a time trace, we obtain the bleaching time, i.e., the time it takes for the molecule to bleach under a given intensity of continuous irradiation. The excitation intensities reported in this paper are free-space intensities, which are not corrected for local field and index of refraction. Typical excitation intensities used in this work are 1.5 kW/cm^2 at room temperature and 0.4 kW/cm^2 in liquid helium. The images are recorded with higher intensities, up to 8 kW/cm^2 at room temperature. As the single-molecule experiments are mainly meant as a comparison to the results of the ensemble experiments, only 40 to 100 bleaching events are acquired for each set of conditions.

4.3 Results

4.3.1 Ensemble experiments

Figure 4.1 shows photobleaching traces recorded at three different excitation intensities in air and nitrogen at room temperature, and in helium at 10 K. Figure 4.2 compares photobleaching time traces recorded in air and inert atmosphere and traces at different temperatures. Both figures show that, as a result of photoblinking (cf. Chapter 3), the initial emissivity level decreases with the intensity. All traces strongly deviate from single exponentials (cf. Figure 4.1 a). Furthermore, the shape of the photobleaching traces clearly changes when the intensity increases.

Figure 4.2a shows that photobleaching is more efficient in air than in inert atmosphere at low intensity. This leads to a crossing of the curves. However, the same figure shows that the situation at high intensity is quite different. The bleaching curve in nitrogen stays below the one in air, at least during our observation time. This is a surprising result, because it implies that photobleaching is more efficient in inert atmosphere than in air at high intensity.

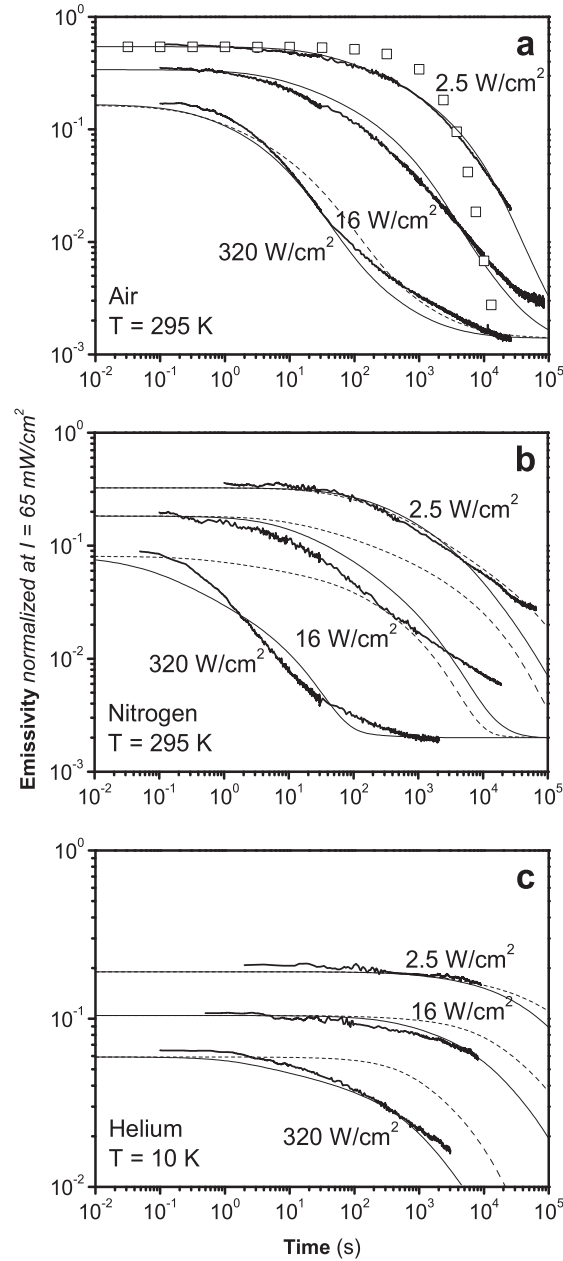


Figure 4.1: Emissivity decay traces due to photobleaching for 2.5, 16 and 320 W/cm^2 in air at 295 K (a), nitrogen at 295 K (b) and helium at 10 K (c). In (a) the trace of open squares indicates a single-exponential. Fits according to the model presented in Figure 4.6 and derived in the Appendix are indicated with dashed lines when they only take primary bleaching processes into account (b_1 and b_2) and with solid lines when they also take secondary bleaching processes through the excited states of D and T_1 (b_3 and b_4) into account. In (a) the dashed and solid lines overlap for the two lower intensities, so only the solid line is visible.

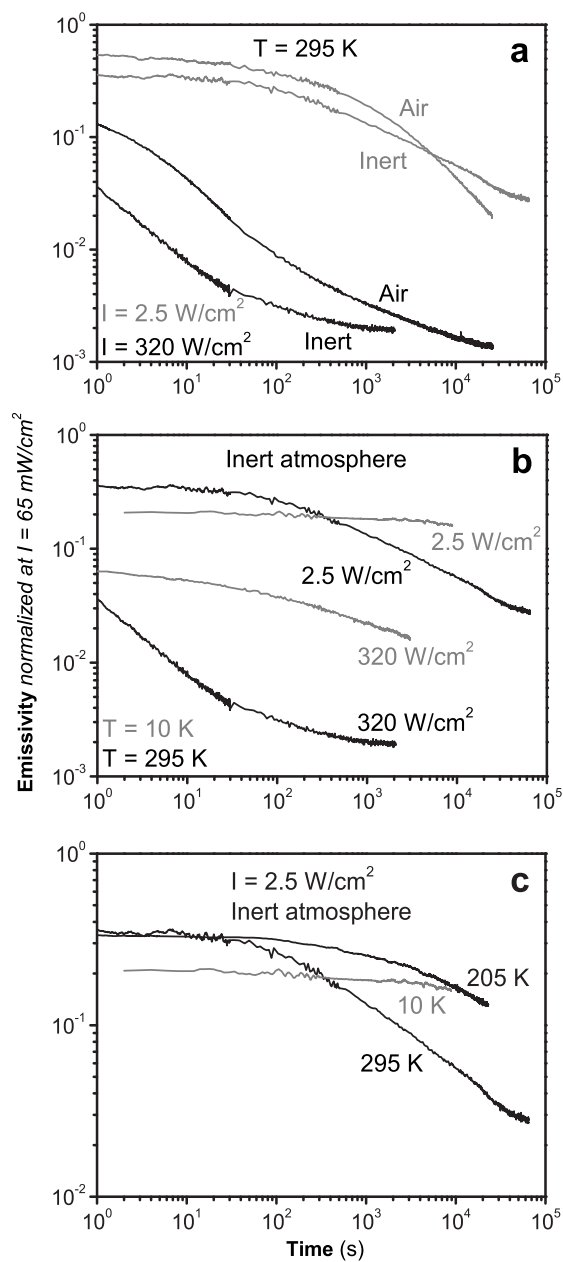


Figure 4.2: (a) Comparison of photobleaching time traces obtained in air or inert atmosphere (nitrogen) at room temperature at 2.5 and 320 W/cm^2 . (b) Photobleaching time traces obtained in inert atmosphere at 295 K and 10 K at 2.5 and 320 W/cm^2 . (c) Variation of photobleaching with temperature for 2.5 W/cm^2 . All traces, besides the one at 205 K (c), are also shown in Figure 4.1.

However, the two high-intensity traces (cf. Figure 4.2 a) come closer at longer times, which suggests that the most bleaching-resistant molecules are more stable in inert atmosphere than in air.

Figure 4.2 b shows the effect of temperature at low and high intensity. In our time window, at 10 K hardly any photobleaching is observed at 2.5 W/cm^2 , which is clearly not the case at 320 W/cm^2 , although the photobleaching is much reduced with respect to 295 K. Figure 4.2 c shows that the most pronounced change takes place between 295 and 200 K. This is also observed at the higher excitation intensities (data not shown).

4.3.2 Single-molecule experiments

Figure 4.3 shows a typical example of a $15 \times 15 \mu\text{m}^2$ fluorescence image generated by our set-up at 1.5 K in liquid helium.

From each spot in a given image we can obtain a fluorescence time trace; a few examples are shown in Figure 4.4. Only the traces consisting of the contributions of 1 or 2 R6G molecules are used for further analysis. In this way, 89 time traces have been obtained at 295 K in air, 58 at 295 K in nitrogen

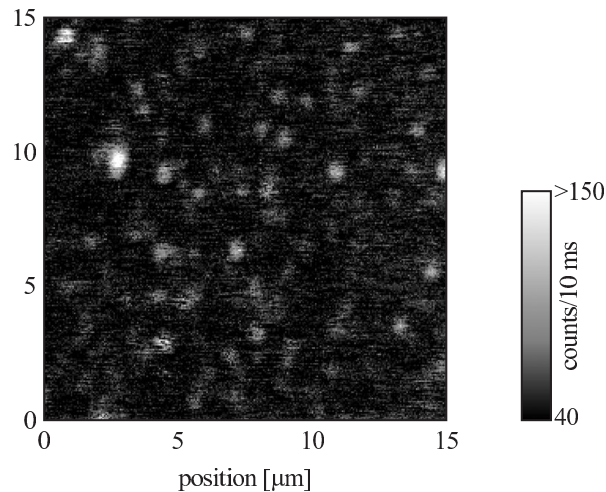


Figure 4.3: A $15 \times 15 \mu\text{m}^2$ confocally scanned fluorescence image of a poly(vinyl alcohol) film containing rhodamine 6G molecules measured at 1.5 K in liquid helium. The image consists of 256×256 points and is recorded with a time-resolution of 10 ms/point at an intensity of 0.8 kW/cm^2 . The sizes of the spots (about 600 nm) are limited by the optical quality of the objective in liquid helium. Most of them stem from single rhodamine 6G molecules.

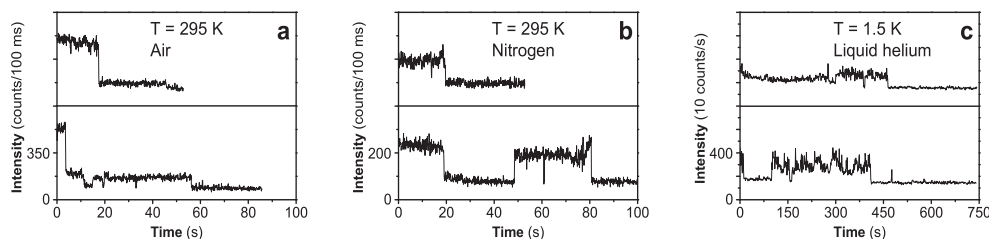


Figure 4.4: Examples of fluorescence time traces of single rhodamine 6G molecules in poly(vinyl alcohol) obtained in air at 295 K (a), in nitrogen at 295 K (b) and in liquid helium at 1.5 K (c). The time resolution is 100 ms at 295 K and 1 s at 1.5 K, and the intensities are 1.5 kW/cm^2 at 295 K and 0.4 kW/cm^2 at 1.5 K. Some of the time traces show contributions of two molecules, like the lower trace in (a).

and 37 at 1.5 K in liquid helium. In these traces step-like bleaching behavior is observed, which confirms that the signal arose from single molecules. The time traces of very bright spots (e.g. the top left corner of Figure 4.3) generally show multi-step photobleaching, which indicates the presence of several molecules. Besides bleaching, blinking can be observed in the time traces. The off-times can become very long, up to tens of seconds, as is for instance visible in the lower trace of Figure 4.4 b.

From every trace the bleaching time of the molecules is determined. Two remarks about these times have to be made: First, the bleaching time, defined previously as the total duration of the time trace until bleaching, is not the same as the total time the molecule emits, because of blinking. Second, we have to set a maximum waiting time to distinguish between bleaching and blinking with long off-times. This procedure introduces some arbitrariness in the results.

Figure 4.5 shows the histograms of the bleaching times obtained from the time traces recorded at the three different experimental conditions. The shape of the histograms differs significantly between room and low temperature. At room temperature the distributions of the bleaching times are fitted reasonably well with a single-exponential, although a significant non-exponential “tail” is present (cf. the insets in Figure 4.5 a and b). The average bleaching time in air is roughly half as long as in inert atmosphere, 11 s versus 22 s. At low temperature the histogram is completely different. The bleaching times are spread over orders of magnitude and one third of the molecules live longer than 1000 s. Some molecules were even found to bleach only after more than one hour.

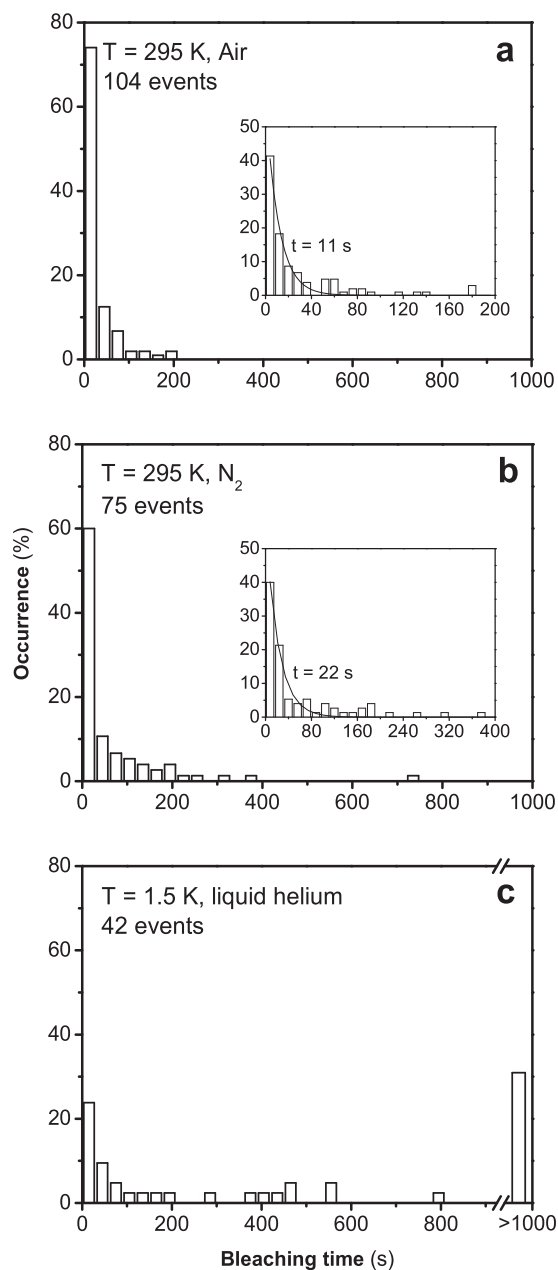


Figure 4.5: Histograms of bleaching times obtained in air at 295 K at 1.5 kW/cm^2 (a), in nitrogen at 295 K at 1.5 kW/cm^2 (b) and in liquid helium at 1.5 K at 0.4 kW/cm^2 (c). In each diagram the total number of studied bleaching events is indicated. The insets in (a) and (b) show single-exponential fits of the respective distributions, yielding an average bleaching time of 11 s in air at 295 K and 22 s in nitrogen at 295 K. Note that for both histograms a significant non-exponential “tail” remains at longer times.

4.4 Discussion

4.4.1 Simulations of the ensemble photobleaching

In the most naive model, photobleaching is a one-photon process with a constant quantum yield β , in which the number of surviving molecules, N , decays exponentially with the number of absorbed photons, σQt :

$$N = N_0 \exp(-\beta\sigma Qt) \quad (4.1)$$

where σ is the absorption cross-section of the dye and Q the number of photons per unit time and unit area. The cross-section σ is supposed to be independent of laser intensity as long as this intensity is much smaller than the saturation intensity of the three-level system including the triplet state. As pointed out in the Results Section, the curves of Figure 4.1 immediately show that this single-exponential behavior can in no way describe the observed photobleaching. Furthermore, the strong dependence of the shape of the curves on intensity shows that photobleaching is not a function of the photon dose, Qt , only, but that the cross-section must depend on the excitation intensity already at weak intensities. This latter conclusion is not surprising, since our study of photoblinking (Chapter 3) has demonstrated the importance of two dark states (triplet and radical anion) in the photophysics of rhodamine dyes under illumination. These dark states strongly affect the photobleaching kinetics.

To understand the observed photobleaching curves (Figures 4.1 and 4.2), we start from our photoblinking model for R6G in PVA as derived in Chapter 3. Most of the molecules (about 95%, which we call population 1), quickly go from their triplet state to the radical anion dark state, from where they return to the singlet ground state after a comparatively long radical lifetime (microseconds to seconds). The remaining molecules (approximately 5%, which we call population 2), do not form the radical anion, but decay directly from the triplet state to the singlet ground state. These dark states must be reactive intermediates in photobleaching, because if they were not, they would “protect” the molecules from bleaching. In that case, photobleaching would saturate as soon as the dark state(s) got populated, which happens already at very low intensities (Chapter 3). The data of Figure 4.1 show that photobleaching does not saturate, but proceeds at a lower and lower rate as time goes. We thus will have to introduce bleaching processes from the dark states. Let us first only consider that primary bleaching of the excited states takes place. Any of the three excited states, S_1 , T_1 , D_0 , can in principle be involved (S_0 is assumed to be stable in the absence of light, i.e., no bleaching is observed in the dark). Introducing bleaching rates from S_1 (b_0), T_1 (b_1) and D_0 (b_2) as

fitting parameters, we obtain the dashed curves in Figure 4.1. In the actual fitting procedure (details can be found in the appendix), b_0 cannot be fitted independently from b_1 and b_2 . Therefore we have neglected b_0 for the sake of simplicity. We have applied the known literature value for the bleaching quantum yield of R6G in aerated ethanol at low intensity [113] to describe the photobleaching of population 2. Moreover, we have distributed the bleaching rates to better account for the strong non-exponential character of the observed photobleaching curves (cf. Figure 4.1). The dashed curves simulate the photobleaching in air at room temperature satisfactorily, but very poorly when we apply this model to high intensities either in inert atmosphere or at low temperatures.

Photobleaching is obviously accelerated with intensity and we have to introduce secondary processes, in other words to assume that the molecules of population 1 can be excited from D_0 to a higher excited state D_n of the radical, from which they bleach with rate b_3 . We also have to introduce such a bleaching channel for population 2 (the 5% of the molecules with only the triplet as a dark state), with associated rate b_4 , to simulate the bleaching behavior at longer times. From the literature [46, 47] we have indications that both dark states indeed absorb at 514.5 nm. The complete model describing the photobleaching of both populations, 1 and 2, is shown in Figure 4.6. This model fits all photobleaching curves in a qualitative way. Note, however, that the shape of the fitted curves differs from that of the data, which may indicate that our logarithmic distributions (cf. Appendix) are not correct, or that our model is still incomplete, i.e., that more mechanisms and/or more intermediate levels should be considered. Our point here, however, is not to describe bleaching quantitatively, but rather to propose and discuss plausible mechanisms for the main dependence of bleaching on intensity, atmosphere, and temperature.

4.4.2 The non-exponential photobleaching kinetics

The observed non-exponential kinetics of all distinguishable photobleaching processes (primary bleaching and secondary photobleaching of dark states of the molecules in population 1 and 2, see the table in the Appendix) may be related to the many different reaction pathways probably contributing to each process. Comparable experiments on fluorescein [75, 99–103] also revealed non-exponential photobleaching dynamics, although the triplet was supposed to be the only reactive metastable state. In one of their papers, Talhavini and Atvars [75] fit the photobleaching of fluorescein at a comparable concentration in PVA with a single rate. However, their experiments have a limited dynamic

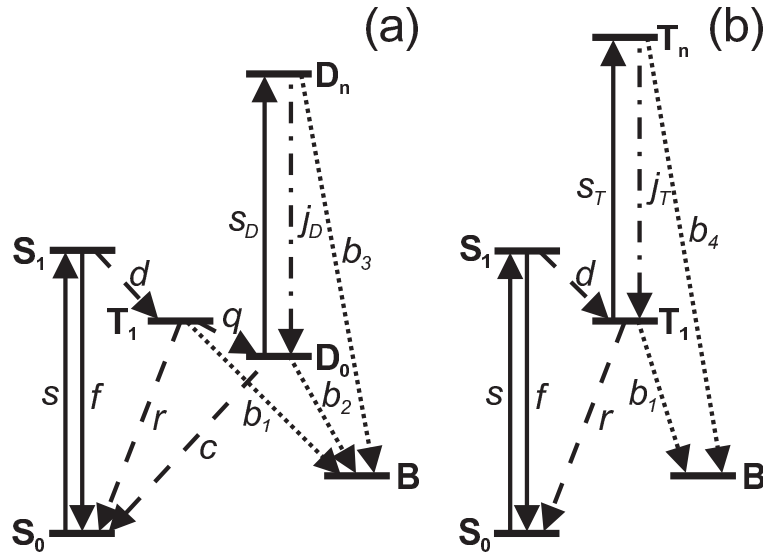


Figure 4.6: (a) Schematic energy-level diagrams of the six-level system describing the photobleaching of 95% of the rhodamine 6G (R6G) molecules in poly(vinyl alcohol) (a) and of the five-level system describing the photobleaching of the remaining 5% of the R6G molecules (b). Both schemes include the electronic ground state (S_0), the first excited singlet state (S_1), the lowest triplet state (T_1) and the bleached “state” (B). In addition (a) contains the radical anion of R6G in the ground state (D_0) and in an excited state (D_n) and (b) contains an excited triplet state (T_n) of R6G. Solid arrows indicate radiative transitions, dashed ones blinking transitions, dotted ones bleaching reactions, and the dashed-dotted ones internal conversion.

range, which makes it difficult to discern non-exponential behavior.

On grounds of our simulations it is impossible to determine which population (1 or 2) contributes to the tails of the bleaching curves (cf. Figures 4.1 and 4.2).

4.4.3 Photobleaching and excitation

The change in shape of the photobleaching curves, correctly reproduced by our model, is caused on the one hand by saturation of the radical population already at low intensity as observed in Chapter 3 and, on the other hand, by secondary photobleaching of this radical anion (and, less importantly, of the triplet state). Normally, secondary photobleaching of intermediate states is only significant at very high excitation intensities [105, 107]. However, as the radical anion has a much longer lifetime than triplet states, secondary photobleaching of the radical becomes already significant at 2.5 W/cm^2 (at least in

inert atmosphere). The secondary photobleaching of the triplet for population 2 mainly takes place at times longer than minutes, when the molecules have absorbed a comparable number of photons as in high-power but short-time experiments [105, 107].

4.4.4 Photobleaching and atmosphere

The primary bleaching from both dark states (triplet and radical anion) is, as expected, enhanced by oxygen (cf. the table in the Appendix). However, the secondary photobleaching from both dark states is so much reduced in air that it becomes negligible. This reduction leads to the paradoxical observation that at high intensity, photobleaching is much faster in inert atmosphere than in air (Figure 4.2 a)! At first sight, the reduction seems the effect of the shortened lifetime in air of both the radical anion (Chapter 3), by one order of magnitude, and of the triplet state [46, 59], by two orders of magnitude. For the triplet photobleaching, this shortening indeed explains the observed decrease. However, this is not the case for the radical photobleaching, which is reduced by almost three orders of magnitude between inert and air atmosphere. As the bleaching rate (b_3) of the excited state of the radical (D_n) itself can only increase with oxygen, the lifetime of D_n has to decrease with oxygen. Quenching of D_n by oxygen seems unlikely because D_n should have a very short lifetime (it is expected to relax quickly by internal conversion), unless oxygen forms a complex with the dark state, in which case the reaction with oxygen is not diffusion-limited. Since we have no means to experimentally test the quenching pathway of the excited radical, this scheme remains a mere speculation. More intermediates might be involved.

4.4.5 Photobleaching and temperature

The main decrease in photobleaching efficiency with temperature takes place between 295 and 200 K (Figure 4.2 c) in agreement with earlier observations that water plays an important role in photobleaching [21, 67, 70]. That photobleaching remains significant at 10 K shows that at least some bleaching processes have no activation barrier or very low ones. Possible candidates are hydrogenation of the dye by a proton that tunnels from the matrix, or electron transfer from or to a nearby donor site. Hydrogenated intermediates have been observed at low temperature in a fluorescence study of pentacene [114].

4.4.6 Photobleaching of single molecules

Our single-molecule study is intended as a qualitative comparison to the ensemble results. At room temperature the histograms of the observed bleaching times in the single-molecule experiments (excitation intensity 1.5 kW/cm^2), can be fitted with a single bleaching time (cf. Figure 4.5 a and b) of 11 s in air and 22 s in inert atmosphere. Although both histograms are clearly not single-exponential, the fit provides us with an average bleaching time. Both average bleaching times are considerably longer than those observed in the ensemble experiments at 320 W/cm^2 (cf. lower plots in Figure 4.2 a). Furthermore, the bleaching times of the single molecules are shorter in air, in contrast to the bulk (Figure 4.2 a). The longer bleaching times indicate that the single molecules constitute a relatively bleaching-resistant subpopulation. These molecules contribute to the ensemble curves of Figure 4.2 b mainly in the region after 10 s (the intensity in the single molecule experiments is five times higher). As has been pointed out previously, these molecules bleach faster in air than in inert atmosphere, in agreement with the single-molecule observations. The reduction factors of photobleaching efficiency on going from air to inert atmosphere, 1.5 for the ensemble curves (between 30 and 100 s) and 2 for the single-molecule experiments, are in reasonable agreement. In inert atmosphere, more molecules bleach at low illumination doses. This is expected to lead to lower numbers of detectable molecules, but we have not tested this experimentally.

The average bleaching time in air at 1.5 kW/cm^2 , 11 s, agrees well with times reported earlier for similar excitation conditions. Mei et al. [93] report 15 s for R6G in trehalose at roughly 1 kW/cm^2 , Hou et al. [70] 12 s for Nile red in PVA at approximately 1 kW/cm^2 and Hernando et al. [83] 11 s for tetramethylrhodamine-5-isothiocyanate in PVA at 4.5 kW/cm^2 . For the data in nitrogen no direct comparison is available, but for systems with the triplet as the only dark state, the reduction in bleaching efficiency relative to air is at least one to two orders of magnitude [53, 55, 61, 89]. Therefore, the observed reduction by a factor of 2 excludes that the single molecules are those with the triplet as the only dark state. The smaller factor of 2 probably stems from secondary photobleaching of the radical anion in inert atmosphere (see the discussion of the ensemble experiments). The reduction of photobleaching is so small that it is doubtful whether removing oxygen is any help at all to detect single molecules. We expect more resolvable molecules in air and shorter off-times in photoblinking.

At 1.5 K, the histogram of the bleaching times reveals a very broad distribution (Figure 4.5 c), in which one third of the molecules survive longer than 1000 s.

In the ensemble experiment at 10 K (Figure 4.2 b), performed at a comparable intensity (320 W/cm^2 in the ensemble versus 400 W/cm^2 in the single-molecule experiment), 25 % of the molecules live longer than 1000 s. This suggests that, as compared to room temperature, a larger fraction of molecules are observed as single ones at low temperatures. This is no hard proof, however, because we might still look at a subpopulation with the same distribution of bleaching times as the total population. Further studies at variable temperatures are necessary to compare the numbers of discernable single molecules at low temperature and at room temperature.

4.4.7 Photoblinking of single molecules

Regarding photoblinking, it is interesting to investigate how the slow recovery rate from the radical anion D (with median values from 4 s^{-1} in air at 295 K to 0.2 s^{-1} below 80 K as found in Chapter 3), manifests itself at the single-molecule level. In principle there are two extreme possibilities: there could be “bright” and “dark” molecules, corresponding to short and long recovery times of their dark states, respectively, or each molecule could present both short and long dark periods in its fluorescence. In the first case, only the bright molecules will appear in a single-molecule experiment and their fluorescence time traces will only present relatively short off-times. The second case resembles the photoblinking of semiconductor nanocrystals [56,57], where long and short off-times are found in the fluorescence time trace of each individual nanocrystal. The fluorescence time traces of single R6G molecules in PVA (Figure 4.4) only occasionally reveal photoblinking with off-times longer than our time-resolution of 100 ms, sometimes up to tens of seconds. Such long off-times have also been observed earlier, for tetramethylrhodamine-5-isothiocyanate in PVA by Hernando *et al.* [83] and for R6G in poly(methyl methacrylate) by Vargas *et al.* [69]. However, as most time traces do not display such long off-times, single molecules seem brighter than the “average” molecule observed in the ensemble experiments. This suggests that photoblinking mainly leads to the existence of bright and dark molecules, i.e., it reduces the number of observable single molecules.

Off-times shorter than 100 ms, our time resolution, can be probed by comparing the on-levels between air and inert atmosphere. An effect is expected because the recovery from D (and also from the triplet) is accelerated by oxygen as shown in Chapter 3. Figure 4.7 shows histograms of the average on-levels in air and nitrogen atmosphere at room temperature. The brightness is approximately 1.5 times lower in inert atmosphere than in air, which confirms that the off-times are indeed on average longer in inert atmosphere.

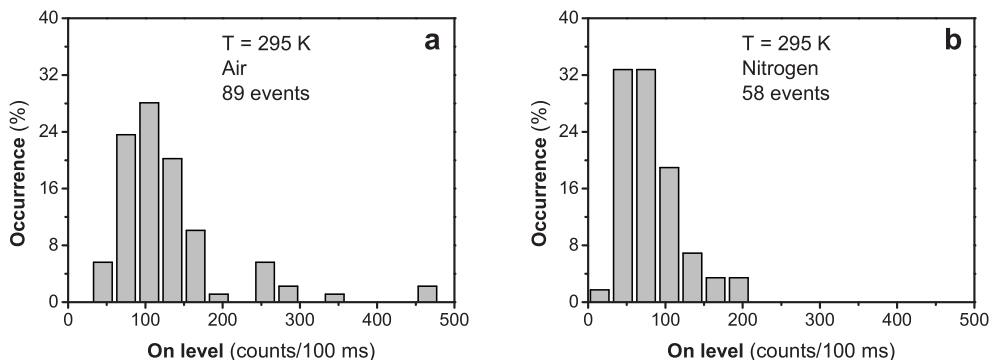


Figure 4.7: Histograms of the average on-levels of the fluorescence time traces recorded in air (a) and nitrogen (b) at room temperature. The applied excitation intensity was 1.5 kW/cm^2 .

If the photobleaching would be completely related to the triplet, a ratio of 3 would be expected between the average on-levels in air and inert atmosphere at 1.5 kW/cm^2 . (This number can be calculated by taking the ratio of the steady-state emissivities (Equation (4.2) in the appendix) with the appropriate parameters for the triplet of R6G in air and in inert atmosphere.)

Although the radical anion as an additional dark state drastically alters the photophysics and photochemistry of R6G molecules in PVA, its effect on the observed single molecules does not seem that strong. We attribute this to the bias towards “bright” and stable molecules in the single-molecule experiments. Nevertheless, some differences remain with molecules that have the triplet as their only dark state. Long-off-time blinking events appear occasionally, and the reduction in the photobleaching quantum yield between air and inert atmosphere is only a factor of two, while it is 1 or 2 orders of magnitude for molecules with only a triplet dark state [53, 55, 61, 89].

4.5 Conclusion

We have studied the photobleaching of R6G in PVA on large ensembles of molecules with continuous-wave excitation. We have simulated our results with a kinetic model involving the triplet of R6G, the radical anion and their excited states. We have distinguished four different photobleaching processes, which all exhibit non-exponential kinetics. Oxygen has been shown to play a double-sided role in the photobleaching. On the one hand it stimulates bleaching by reacting with the metastable states, but on the other hand it reduces bleaching by shortening their lifetimes. This explains the counterintuitive

observation that the main part of the ensemble bleaches faster in inert atmosphere than in air at higher intensities. The small, bleaching-resistant part of the population, seen as single molecules, are only marginally more stable in inert atmosphere. Photobleaching decreases significantly at low temperatures, but does not vanish altogether. The results of the single-molecule experiments are in good agreement with the ensemble results. Photoblinking and photobleaching appear to reduce the number of observable single molecules rather than to shorten their observation times.

Our study demonstrates once more how complex photobleaching is. Although our findings strictly apply to R6G in PVA, we believe that some of them, like the double role of oxygen and the occurrence of photobleaching processes with very low activation barriers, are of general value. The matrix PVA may also favor long-lived radical ion intermediates for other fluorophores and for labelled biomolecules.

Acknowledgements

The author thanks Dr. M. A. Kol'chenko, G. Mathies, E. van der Togt and A. Nicolet for their contributions to the experiments and acknowledges helpful discussions with Prof. E. J. J. Groenen.

4.6 Appendix – derivation of bleaching rates

The starting point of the derivation of the expression for the photobleaching decay is the steady-state emissivity before the onset of photobleaching (cf. Chapter 3). For population 1 this steady-state emissivity A_{4LS} reads:

$$A_{4LS}(I) = \frac{\sigma N \eta}{f} \left(1 + \frac{s}{f} \left(1 + \frac{d}{c} \right) \right)^{-1} \quad (4.2)$$

with s being the pump-rate of the S_0 - S_1 transition:

$$s = \sigma N I \quad (4.3)$$

where σ is the absorption cross-section of R6G in PVA ($3.0 \times 10^{-16} \text{ cm}^2$, determined in Chapter 3) at 514.5 nm, N is the number of photons in 1 J (2.59×10^{18} photons/J) at 514.5 nm, I is the absolute excitation intensity (in W/cm^2), η is the fluorescence quantum yield of R6G (drops out eventually in the normalization of the emissivity), and f is the fluorescence rate of R6G ($2.5 \times 10^8 \text{ s}^{-1}$ [46]). The pump rates s_D of the D_0 - D_n and s_T of the T_0 - T_n

transitions (see Figure 4.6) obey similar equations as (4.3) with σ replaced by σ_D and σ_T , respectively, the (unknown) absorption cross-sections of these transitions at 514.5 nm. For population 2 the expression of the steady-state emissivity, A_{3LS} , has the same form as Equation (4.2) with c replaced by r . The inter-system crossing rate d of R6G is approximately $1.0 \times 10^6 \text{ s}^{-1}$ [46,47] (independent of temperature and atmosphere), the triplet recovery rate r is roughly $2.5 \times 10^5 \text{ s}^{-1}$ in air [59] and $2.5 \times 10^3 \text{ s}^{-1}$ in inert atmosphere [46] (independent of temperature). In Chapter 3, the recovery rate from the radical anion (D), c , has been found to be distributed. To provide an estimate of the magnitude of c , we give the median values of the obtained distributions: 4 s^{-1} in air at 295 K, 0.4 s^{-1} in inert atmosphere at 295 K and 0.2 s^{-1} in inert atmosphere below 80 K. (The median of a distribution is the value of the distributed parameter at which one half of the total integral of the distribution can be found at higher or equal and the other half at lower or equal values.) The general expression for the emissivity decay due to photobleaching, Ω , is found by considering the bleached state as an extra level (as indicated in Figure 4.6) and applying the steady-state approximation to the rate equations associated to all other levels. We neglect d and all bleaching rates with respect to f . For population 1 we obtain Ω_{4LS} :

$$\Omega_{4LS}(I, t) = A_{4LS}(I) \exp(-\omega_{4LS}(I)t) \quad (4.4)$$

with total bleaching rate ω_{4LS} :

$$\omega_{4LS}(I) = P_{4LS}(I) (X_1 + IY_1) \quad (4.5)$$

with saturation parameter P_{4LS} :

$$P_{4LS}(I) = \frac{s}{f} \left(1 + \frac{s}{f} \left(1 + \frac{d}{c} \right) \right)^{-1} \quad (4.6)$$

and the effective bleaching parameters X_1 and Y_1 :

$$X_1 = \frac{d}{q} b_1 + \frac{d}{c} b_2 \quad (4.7)$$

$$Y_1 = \frac{d}{c} \left(\frac{\sigma_D N}{j_D} \right) b_3 \quad (4.8)$$

For population 2 similar equations can be derived. The emissivity decay Ω_{3LS} has the same form as Equation (4.4) with A_{4LS} and ω_{4LS} replaced by A_{3LS} and ω_{3LS} , respectively. The total bleaching rate ω_{3LS} equals:

$$\omega_{3LS}(I) = P_{3LS}(I) (X_2 + IY_2) \quad (4.9)$$

with the saturation parameter $P_{3\text{LS}}$ resembling Equation (4.6) with c replaced by r , and the effective bleaching parameters X_2 and Y_2 :

$$X_2 = \frac{d}{r} b_1 \quad (4.10)$$

$$Y_2 = \frac{d}{r} \left(\frac{\sigma_{\text{T}} N}{j_{\text{T}}} \right) b_4 \quad (4.11)$$

To reproduce the photobleaching decay traces we need the total emissivity decay normalized to the emissivity at intensity $I_0 = 65 \text{ mW/cm}^2$. At this intensity no photobleaching is observed on a time-scale of hours, so that we effectively normalize to the steady-state emissivity related to photoblinking at this intensity. The normalized total emissivity decay due to photobleaching, Ω' , then reads:

$$\Omega'(I, t) = \frac{0.95\Omega_{4\text{LS}}(I, t) + 0.05\Omega_{3\text{LS}}(I, t)}{0.95A_{4\text{LS}}(I_0) + 0.05A_{3\text{LS}}(I_0)} \quad (4.12)$$

Simulations are carried out for three distinct experimental conditions: air at 295 K, inert atmosphere at 295 K and inert atmosphere at 10 K. The effective bleaching parameters X_1 (4.7), Y_1 (4.8), X_2 (4.10) and Y_2 (4.11) are used as fit parameters. When just the distribution of c (Chapter 3) is taken into account, it is impossible to satisfactorily reproduce the experimental data (simulations not shown). Therefore the effective bleaching parameters are all allowed to be distributed and besides that to change with atmosphere and temperature. The distributions are supposed to be uniform and broad on a logarithmic scale. We approximate this by the following summation:

$$\langle f(k) \rangle = \frac{1}{N} \sum_{i=1}^N f(k_i) \quad (4.13)$$

where $\langle f(k) \rangle$ is the average over individual functions $f(k_i)$ of k_i , which are elements of the distribution of k . The elements k_i obey

$$k_i = \exp \left(\ln(C_k) + \frac{1}{N} \ln(W_k) \left(i - \frac{N+1}{2} \right) \right) \quad (4.14)$$

with C_k the center value and W_k the width of the distribution of parameter k . Reasonable accuracy is obtained when N is chosen equal to 10.

Two kinds of simulations are performed. First, only X_1 and X_2 are used as fit parameters to reproduce the data. We suppose that the value of X_2 is approximately 300 s^{-1} in air, as the bleaching quantum yield of R6G in ethanol

is known to be roughly 10^{-6} [113]. Furthermore, X_2 is expected to be at least one order of magnitude lower in inert atmosphere [53, 55, 61, 89]. The results are shown in Figure 4.1. For all three conditions it is possible to fit the data at the lowest intensity. However, a direct extrapolation to higher intensities is feasible with the obtained parameters only for air at 295 K (Figure 4.1 a).

The data in inert atmosphere can only be fitted by including Y_1 and Y_2 (Figures 4.1 b and c). For air (Figure 4.1 a), the inclusion of Y_1 and Y_2 is also investigated. We suppose Y_2 to be reduced by a factor of 100, due to the change in triplet lifetime. The introduction of Y_1 and Y_2 only affects the trace at 320 W/cm^2 , but does not really improve the fit. Better fits might be obtained with other distributions than the uniform distribution in logarithmic space (Equation (4.13)).

The table below reports the values of X_1 , Y_1 , X_2 and Y_2 used in the simulations shown in Figure 4.1. All parameters are distributed. The width of the respective distribution is indicated between square brackets after each number, which itself gives the center value of the distribution on a logarithmic scale (cf. Equations (4.13) and (4.14)). The data in inert atmosphere at 295 K require secondary bleaching processes (Y_1 and Y_2) and a change of the primary bleaching parameter X_1 . Both sets of parameters are given in the table.

Conditions	X_1 (s^{-1}) [width]	Y_1 (cm^2/J) [width]	X_2 (s^{-1}) [width]	Y_2 (cm^2/J) [width]
Air 295 K	300 [10^3]	0.1 [10^2]	300 [10^2]	3×10^{-2} [10^3]
Inert 295 K (1)	500 [10^2]	..	3 [10^2]	..
Inert 295 K (2)	50 [10^4]	50 [10^2]	3 [10^2]	3 [10^3]
Inert 10 K	5 [10^4]	0.5 [10^2]	0.3 [10^3]	4×10^{-3} [10^6]

5 Local temperature determination by Raman spectroscopy

abstract – We demonstrate local temperature determination by Raman spectroscopy on poly(methyl methacrylate) substrates with an accuracy ($\pm 2\sigma$) of around ± 1 K at ambient temperature. Although we do successfully apply Raman spectroscopy to monitor laser-induced local heating by absorption of a thin metal coating, the required accumulation time, 100 to 1000 s, is too long to allow temperature calibration at a reasonable rate.

5.1 Introduction

To reproducibly perform a temperature-cycle experiment as proposed in Section 1.3, we require a tool to calibrate the temperature of the hot spot generated by the focused heating laser. In this chapter we consider Raman spectroscopy. As an optical method it has the advantage that it automatically probes a spot with dimensions comparable to those of the heating spot. A further advantage of Raman spectroscopy is that it provides the absolute temperature. Raman scattering is the inelastic part of light scattering. It was discovered in 1928 by C. V. Raman together with his students [115–117]. Although it is a weak effect, Raman scattering is used in many ways [118, 119]. From the beginning on [120], it was realized that the Raman spectrum contains information on the temperature of the scattering region through the ratio of the blue-shifted Anti-Stokes and the red-shifted Stokes line of each vibration. The exact relation is given by:

$$T = -\frac{\Delta E}{k_B} \left(\ln \left[\left(\frac{I_{AS}}{I_S} \right) / \left(\frac{\nu_{AS}}{\nu_S} \right)^4 \right] \right)^{-1} \quad (5.1)$$

with ΔE the vibrational energy, k_B Boltzmann’s constant, 1.38×10^{-23} J/K, I_{AS} and I_S the intensities of the corresponding anti-Stokes and Stokes lines and ν_{AS} and ν_S their frequencies. The frequency term corrects for the higher scattering efficiency at the frequency of the anti-Stokes line than at that of the Stokes line. Nowadays, Raman scattering is used to determine the temperature of microparticles [121], flames [122], nanotubes [123], aerosol particles [124], and of various other systems [125, 126]. Furthermore, comparisons of Raman scattering with finite-element model predictions for temperature determination have been done [127, 128], as well as direct temperature calibrations [129, 130].

We measure the Raman scattering of the polymer poly(methyl methacrylate) (PMMA) at 514.5 nm and 785 nm. PMMA has a characteristic Raman spectrum with clear, relatively narrow lines (see for instance the Jobin Yvon Raman spectra of polymers at www.spectra.galactic.com). The lines we consider in our experiment are the ones with Raman shifts of 355, 475, 590 and 805 cm^{-1} . Their associated vibrational energies are still low enough to provide for reasonably intense anti-Stokes lines around room temperature. Our first goal is to determine the accuracy of local-temperature measurements by Raman spectroscopy. In this work, we are able to reproduce the surrounding temperature with an accuracy of $\pm 1.1 \text{ K}$ ($\pm 2\sigma$) at 514.5 nm with a total acquisition time of 1000 s. Secondly, we wish to apply Raman spectroscopy

to calibrate the temperature in a laser-induced hot spot. For experimental purposes we require the Raman spectrum at 785 nm, where the Raman effect is 6 times weaker resulting from a lower scattering efficiency. Nevertheless, we are able to observe the local heating, even with an acquisition time of 100 s, albeit with a rather low temperature accuracy (± 10 K).

5.2 Accuracy of Raman-determined temperatures

We measure Raman scattering at 514.5 nm of a 200 μm thick round PMMA substrate with a diameter of 20 mm. The substrate is mounted in the sample holder of the temperature-cycle microscope (Chapter 2), and kept in the cryostat at room temperature (under an air atmosphere). The back-reflected laser light is filtered by a notch filter at 514.5 nm (Kaiser Optical Systems HNPF-514.5) and subsequently analyzed by a spectrograph (Acton Spectra Pro 500i equipped with a back-illuminated Princeton Instruments CCD camera) to measure the Stokes and anti-Stokes parts of the Raman spectrum. We use a grating of 1800 lines/mm, an accumulation time of 100 s for the Stokes side and 900 s for the anti-Stokes side, and a laser intensity of 175 kW/cm². This high intensity is required because of the low cross-section of Raman scattering.

In Figure 5.1, we show a typical spectrum obtained from the Stokes side of the Raman spectrum of PMMA in the region from 300 to 900 cm⁻¹ revealing

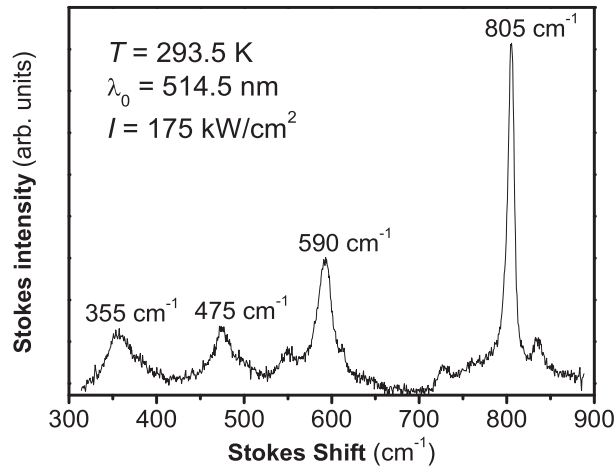


Figure 5.1: Stokes side of the Raman spectrum of PMMA between 300 and 900 cm⁻¹ revealing Raman lines at 355, 475, 590, and 805 cm⁻¹.

the four expected lines. The anti-Stokes side is considerably weaker and here we are hindered by the background of the laser. We can quite reasonably fit this background with a Gaussian profile and subtract that from the data. Nevertheless, this correction procedure seems to be too arbitrary to reproducibly recover the lines at 355 and 475 cm^{-1} , leaving only the lines at 590 and 805 cm^{-1} for temperature determination.

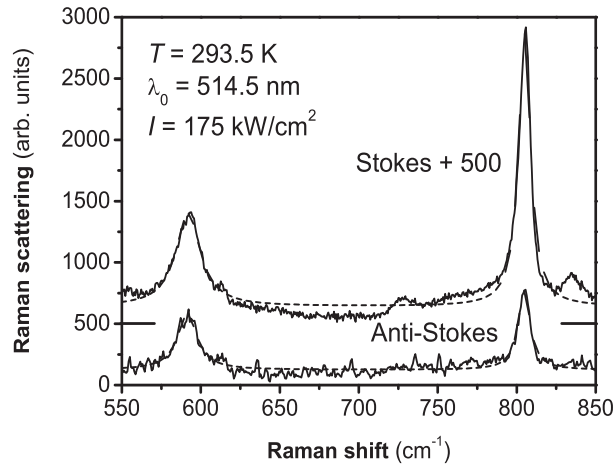


Figure 5.2: Stokes and anti-Stokes (corrected for laser background) sides of the Raman spectrum at 514.5 nm of PMMA between 550 and 850 cm^{-1} at 293.5 K . An offset of 500 is introduced on the Stokes data for reasons of clarity. The acquisition time of the anti-Stokes spectrum was nine times longer than that of the Stokes spectrum. Lorentzian fits of both spectra are shown as dashed lines.

To determine the accuracy of temperature determination at room temperature by Raman spectroscopy under our experimental conditions, we record 6 consecutive spectra while the cryostat temperature is kept at 293.5 K . Figure 5.2 shows one example displaying the Stokes and the corrected Anti-Stokes side between 550 and 850 cm^{-1} . We fit both lines in each spectrum with a Lorentzian line shape. Figure 5.2 reveals good agreement between fit and data. From the fits the required ratios are determined and subsequently the temperature. This procedure is followed for each of the two lines in the six pairs of spectra. From this we obtain on average $(294.8 \pm 1.4)\text{ K}$ based on the 590 cm^{-1} line and $(310.7 \pm 1.8)\text{ K}$ based on the 805 cm^{-1} line. The errors indicate the 95% confidence interval, $\pm 2\sigma$, for a single measurement. Obviously, the procedure introduces a (small) systematic error on the data, probably due to the spectral response of our experimental configuration, for which we simply correct by multiplying the obtained temperature with 0.996 at 590 cm^{-1}

and 0.945 at 805 cm^{-1} . Thus, the highest obtainable accuracy in one measurement at room temperature is $\pm 1.1\text{ K}$ when the corrected temperatures obtained from the 590 and the 805 cm^{-1} lines are averaged.

The accuracy of temperature determination by Raman spectroscopy will obviously improve at higher temperatures, since the intensity of the anti-Stokes line will increase. For our purposes, it is more interesting to estimate what the lowest temperature would be that could be probed by Raman spectroscopy. For the 590 cm^{-1} line, the ratio between Stokes and anti-Stokes intensity is 0.07 at room temperature. From Figure 5.2, we judge the signal-to-background ratio to be approximately 4.5 (we take the complete signal without background subtraction to determine the ratio) for an acquisition time of 900 s. When we require this ratio to be at least 2 to maintain reasonable accuracy, the temperature sensitivity of this line will extend down to about 230 K. For the 805 cm^{-1} line, following similar arguments, we find also 230 K for the lower boundary since the higher intensity of the Raman line compensates for the lower population in the vibrationally excited state.

5.3 Calibration of laser-induced local heating by Raman spectroscopy

The next step is to show that Raman spectroscopy can be applied to reliably measure the temperature in a laser-induced hot spot. Since in the actual temperature-cycle experiment the substrate will face the heating laser (i.e., it will point upwards in Figure 2.1), we have to resort to Raman scattering of the PMMA substrate at 785 nm. This means, a priori, a loss of accuracy since the efficiency of Raman scattering is 6 times lower at 785 nm than at 514.5 nm. In any case, even if the Raman spectrum could be probed from the visible (down) side of the sample, the very high intensity needed to observe Raman scattering would intolerably enhance photobleaching of the fluorophores under investigation.

We measure Raman scattering at 785 nm again from a $200\text{ }\mu\text{m}$ thick round PMMA substrate with a diameter of 20 mm but this time coated with a 50 nm NiCr film (see Section 2.1.1). The substrate is mounted such that the coated side points to the bottom of the cryostat away from the NIR laser, and kept at room temperature (under an air atmosphere). The back-reflected NIR laser light is filtered by a notch filter at 785.0 nm (Kaiser Optical Systems HSPF-785.0) and subsequently analyzed by the spectrograph. Here, we use a grating of 300 lines/mm, accumulation times of 50 s for both the Stokes and the anti-Stokes side, and NIR powers of respectively, 1.5, 3.0, 4.5, or 6.0 mW. A NIR

power of 3 mW corresponds to approximately 250 kW/cm^2 on the substrate. To determine the effect of NIR absorption by the metal layer, we determine Raman spectra from the uncoated (front side with respect to the NIR laser) and the coated side. In this study, we have only considered the 805 cm^{-1} line. Figure 5.3 shows an example of the response at the metal film when a laser power of 3 mW is applied. To determine the temperature, the same procedure is followed as in the previous section. Due to the low accuracy of the anti-Stokes intensity determination, we expect an inaccuracy of at least $\pm 10 \text{ K}$ ($\pm 2\sigma$). Within this accuracy, we find no systematic error in our temperature determination.

Figure 5.4 shows the response of the temperature in the NIR focus to the laser power at the coated and at the uncoated side of the PMMA substrate. We have indicated the estimated inaccuracy of $\pm 10 \text{ K}$ in the two curves of Figure 5.4. Nevertheless, we seem to retrieve the environmental temperature of 293 K quite reliably as is indicated by the relatively low scattering of the “uncoated” data points. The data points from the coated side clearly reveal a substantial temperature increase owing to absorption of the NIR laser by the metal film. The first three points follow a linear relation with a slope of 38 K/mW. The last point is clearly off which probably reflects the degradation of PMMA at this temperature (460-470 K), which is not surprising since the polymer’s glass-transition temperature lies around 378 K [131].

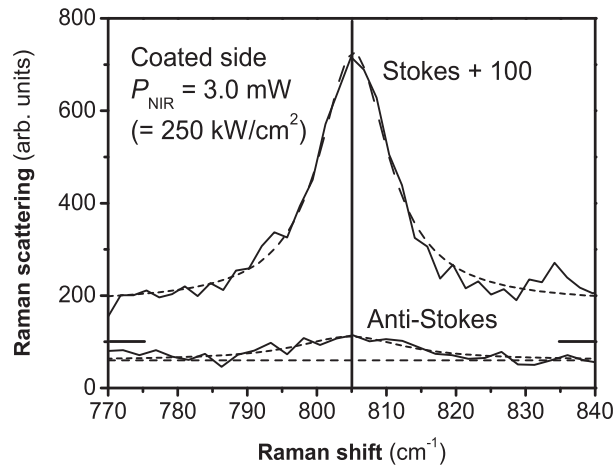


Figure 5.3: Stokes and anti-Stokes sides of the Raman spectrum at 785 nm of PMMA around 805 cm^{-1} at an intensity of 3 mW. Lorentzian fits of the spectra are shown as dashed lines. An additional dashed line indicates the background level in the anti-Stokes spectrum to discern the Raman line from the background.

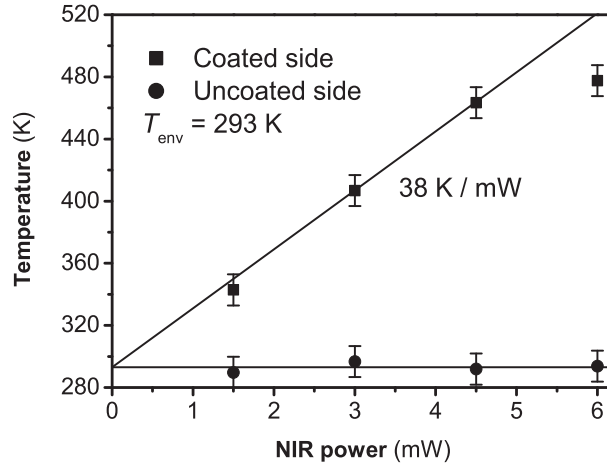


Figure 5.4: Response with NIR power of the temperature in the focus at the coated and at the uncoated side of the PMMA substrate. As it should, the temperature at the uncoated side remains that of the environment even at the highest power. The temperature at the metal side shows a linear increase of 38 K/mW for the first three points. The deviation of the last point is probably due to a change in material properties of the PMMA. The error bars indicate the estimated uncertainty of ± 10 K ($\pm 2\sigma$) for each data point.

5.4 Conclusion

We have shown that Raman scattering at 514.5 nm of a 200 μm thick PMMA substrate yields the absolute temperature with a confidence of ± 1.1 K ($\pm 2\sigma$) around room temperature. We have argued that Raman spectroscopy should be able to probe the temperature reasonably accurately down to 230 K. However, to retrieve this accuracy and temperature sensitivity, an excitation intensity higher than 100 kW/cm^2 and a total accumulation time of 1000 s are required. Subsequently, we have applied Raman spectroscopy to calibrate local heating induced by 785 nm laser light focused onto an absorbing metal coating. We have found that Raman spectroscopy at 785 nm still yields the local temperature even with a reduced accumulation time of 100 s, albeit with a rather low accuracy of ± 10 K ($\pm 2\sigma$). The resulting calibration demonstrates efficient local heating from 295 up to 450 K in our temperature-cycle configuration (Chapter 2).

Raman spectroscopy provides the local temperature quite accurately and does not depend on experimental conditions. Nevertheless, we deem the technique too inconvenient to fully characterize the proposed temperature cycles, because its accumulation time is too long to provide for a temperature cali-

bration with reasonable throughput. However, the feasibility of temperature cycles by laser-induced local heating in our experimental configuration has been demonstrated.

Acknowledgements

The author wishes to thank E. van der Togt for her contributions to the experiments and the analysis of the acquired data.

6 Relaxation in supercooled glycerol near T_g probed by rotational diffusion

abstract – We report fluorescence polarization autocorrelation experiments on a perylene dye in supercooled glycerol at 5 to 25 K above glycerol’s glass-transition temperature (T_g), 190 K. These experiments yield the characteristic timescale of the fluorophore’s rotational diffusion and thereby probe the relaxation dynamics in the supercooled liquid. We present results of both ensemble and single-molecule experiments. We have also studied the same individual molecules at various temperatures. Our results indicate the presence of extremely long-lived spatial inhomogeneities in supercooled glycerol probably related to very slow, larger-scale dynamics. Further, we observe a smoothly increasing dispersion of the single-molecule rotation times upon approach of T_g . We conclude that a supercooled “liquid” should be viewed upon as a structure of alternating fluid and glass-like domains, already at temperatures significantly above T_g .

The contents of this chapter will be published.

6.1 Introduction

Supercooled glycerol is one of the archetypical glass-forming liquids. Although it is possible to crystallize glycerol, its high viscosity, 10^3 times that of water at room temperature [132, 133], favors the formation of a supercooled liquid. This high viscosity of glycerol is related to its complex structure of highly branched intermolecular hydrogen bonds. Between 291.8 K, the melting temperature of crystalline glycerol [134], and 190 K, its glass-transition temperature (T_g) [135–137], the viscosity of supercooled glycerol increases by ten orders of magnitude [136, 137]. Throughout this temperature range, based on shear-force viscosity measurements [136–138], glycerol is believed to retain its normal liquid structure, although its dynamic properties change drastically upon approaching T_g . Not only do the relaxation processes in the liquid slow down enormously, they also reveal highly non-exponential kinetics. In this work, we will only consider α relaxation, the common indicator for intermolecular relaxation processes.

The generally accepted view on glass formation is that it is related to cooperative motion of the molecules in the glass-forming liquid. The role of cooperativity in glass formation has been first suggested by Adam and Gibbs [139]. In this view, the overall non-exponential relaxation is the result of a spread in the sizes of these cooperative domains and glass formation arises from a structural arrest following a divergence of their sizes. Experimental support for this picture has arisen from the observation of spatially inhomogeneous dynamics in many glass-forming systems, varying from simple liquids [140–145] to polymers [14, 146–152]. In the particular case of supercooled glycerol, spatially inhomogeneous dynamics have been identified by dielectric hole-burning [153, 154], nuclear magnetic resonance (NMR) [155], and stimulated Brillouin gain spectroscopy experiments [156, 157]. Since glass-forming systems are supposed to remain liquid until the glass transition, the regions with different relaxation dynamics are expected to exchange with one another to provide for ergodicity. We will refer to this larger-scale relaxation as environmental exchanges. Although environmental exchanges are believed to occur in most glass forming systems [14, 140, 144, 145, 148–152, 154], their typical timescale, mechanism, and role in glass formation have remained unclear.

Recently, Deschenes and Vanden Bout have applied a single-molecule approach to investigate the nature of the spatially inhomogeneous dynamics in glass-forming systems [14, 145, 150, 151]. They studied the rotational diffusion of individual fluorescent guest molecules (rhodamine 6G) in three glass-forming hosts, the polymers poly(methyl acrylate) [14, 150, 151] and poly(*n*-butyl methacrylate) [150], and the liquid *ortho*-terphenyl [145]. Single-molecule

optics is a well-established tool to study rotational diffusion of fluorescent molecules [8, 158–164]. In these experiments, the reduced linear dichroism of a single molecule is followed in real time. The linear dichroism reveals fluctuations owing to rotational diffusion that can be quantified by autocorrelation analysis. In the particular case of glass-forming systems, rotational diffusion will probe the relaxation of the host because the rotation of the dopant molecules is subject to this relaxation. Since the single-molecule approach not only yields the average but also the distribution of rotation times, it directly probes the extent of spatially inhomogeneous dynamics in the host. For short experimental observation times, Deschenes and Vanden Bout found almost mono-exponential single-molecule correlation functions yielding a broad distribution of single-molecule rotation times. This result is consistent with the picture of spatial inhomogeneities as the main source of non-exponential relaxation kinetics. For longer observation times, they detected sudden jumps in the single-molecule rotation rates. They found the average time between two jumps in rotation rate to be 10 to 25 times the typical rotation time, for all three systems they studied. They attributed these jumps to the aforementioned environmental exchanges. Furthermore, they found the overall relaxation (including the environmental exchanges) to be ergodic by observing a narrowing with increasing observation time of the initial broad distribution of single-molecule rotation times towards the average (ensemble) value. Their results on poly(methyl acrylate) have recently been successfully verified by Schob *et al.* [152]. In their work, Deschenes and Vanden Bout also dwell on the implications of two distinct timescales in α relaxation. For the polymers [14, 150, 151], two timescales might simply arise because the probe molecule is much smaller than the polymer chains. On the contrary, in the case of the simple liquid *ortho*-terphenyl, the probe is larger than the host molecules, so that the observed dispersion of environments indicates intermolecular organization. Deschenes and Vanden Bout [145] suggest that the liquid consists of a mosaic of heterogeneous regions, each of which behaves as a homogeneous liquid. However, this is not a satisfying picture because it remains unclear what the boundaries are between the liquid domains, which are crucial to explain the observed spatially inhomogeneous dynamics.

We will study the relaxation of supercooled glycerol closely above T_g (190 K) by analyzing the rotational diffusion of inserted fluorophores, perylenedicarboximide (PDI), at the ensemble and single-molecule levels. Since Deschenes and Vanden Bout have only studied fragile (weak intermolecular interactions) glass formers, we aim to gain more insight into the origin of the spatial inhomogeneities by studying a glass former with strong intermolecular interactions

(hydrogen bonds). In this work, we first characterize the system by an ensemble study, for which we make use of fluorescence anisotropy autocorrelation spectroscopy (FACS). This technique allows, for small ensembles of typically 10 to 30 molecules, the measurement of rotational diffusion through fluctuations of the steady-state fluorescence anisotropy around its average value. Those fluctuations can be quantified through an autocorrelation function yielding the characteristic rotation correlation time [165–167]. Second, we perform single-molecule experiments at static temperatures, slightly above T_g (190 K), following the experimental scheme of Deschenes and Vanden Bout [150]. Additionally, we study the rotation of individual molecules as a function of the temperature, which will provide a detailed picture of the relaxation in glycerol at the single-molecule level.

6.2 Experimental

6.2.1 Sample preparation

We prepare N,N' -bis(2,5-di-*tert*-butylphenyl)-3,4,9,10-perylenedicarboximide (PDI) in glycerol at a concentration of 10^{-7} M for the ensemble experiments and 10^{-9} M for the single-molecule experiments. The structure of this substituted perylene chromophore is indicated in Figure 6.1. In both cases the glycerol solution, which contains about 6 to 8% water, is directly spincoated at 6000 rpm on a round glass plate with a diameter of 20 mm. In order to allow the formation of a stable glycerol film, the glass surface, just before spincoating, is cleaned and completely oxidized in a UV-ozone cleaner (Jelight, model 42-220). The estimated film thickness is around 1 to 3 μm . The viscosity of glycerol changes dramatically with water content [132,133]. Accordingly, prior to use, the samples are dried in the cryostat by repeatedly pumping and flushing with helium gas. Furthermore, we keep the films under a dry and inert helium atmosphere throughout all experiments. By fluorescence anisotropy measurements (which provide a measure for the viscosity) we have established the water content of several glycerol films dried in this manner to be significantly less than 1%. However to reproduce the behavior of pure glycerol, the water content of the glycerol films should be less than 0.1%. This will be checked by comparing the results of the ensemble FACS experiments in this work with literature values for the viscosity of glycerol with less than 0.1% water content.

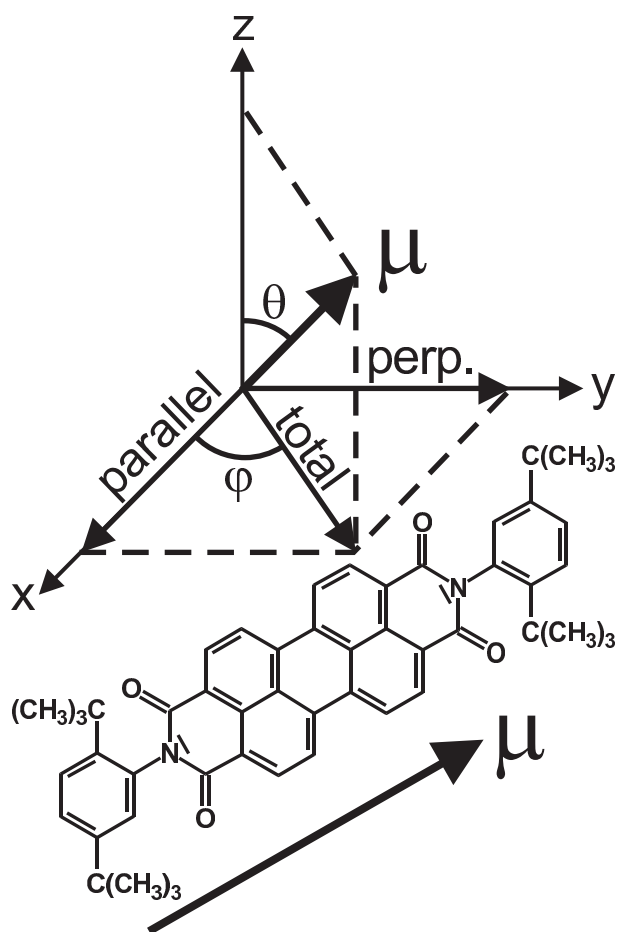


Figure 6.1: Structure of the investigated PDI fluorophore with an indication of the direction of its transition dipole moment μ . Above the molecule, a diagram shows the decomposition of the molecule's dipole moment into detectable components. The excitation laser propagates along the z -axis. The two Euler angles θ and ϕ will fluctuate upon rotational diffusion of the molecule. In the ensemble experiments, we apply a linearly polarized laser, along x , and detect the two orthogonal components "parallel" and "perpendicular" of "total". Although we do not probe directly the component of μ along z , ensemble averaging will provide this component to be approximately equal to the "perpendicular" component. Consequently, fluctuations in the fluorescence anisotropy, Equation (6.1), will relate to full three-dimensional rotation. For an individual molecule, the projection of μ on the z -axis is unknown, so that we can only probe fluctuations in ϕ and θ separately. To observe the fluctuations of ϕ , in-plane rotation, we determine the reduced linear dichroism (Equation (6.5)) by measuring the "parallel" and "perpendicular" components. To make the excitation probability independent of ϕ , we excite the single molecules with circularly polarized light.

6.2.2 Experimental configuration

Our experimental setup is described elsewhere (Chapter 2). As an addition, we have inserted an electro-optical modulator (EOM, Con Optics 200) in the excitation beam, which allows us to alternate the polarization of the excitation laser and thereby to determine the orientation of the molecules in the polarization plane of the laser. In the work of Deschenes and Vanden Bout [150], the influence of the NA of the microscope objective on the measured rotational diffusion is extensively discussed, since previous work by Fourkas [168] had shown that the use of a high NA objective ($NA > 1$) induces a significant depolarized background. For this reason, Deschenes and Vanden Bout have applied a microscope objective with an NA of 0.6. Our special low-temperature microscope objective has an NA of 0.85, which will give a depolarized background of about 10 % of the signal. For the single-molecule experiments, this background will be subtracted from the polarized fluorescence time traces prior to calculation of the reduced linear dichroism.

6.2.3 Ensemble analysis

We study rotational diffusion at the ensemble level by analyzing fluctuations in the fluorescence anisotropy upon excitation by a linearly polarized laser at 514.5 nm. The polarization of the laser is chosen horizontal, along the x -axis in Figure 6.1 ($\phi = 0$). The steady-state fluorescence anisotropy r is the normalized difference between the parallel (F_{\parallel}) and perpendicular (F_{\perp}) detection channels [169]:

$$r = \frac{F_{\parallel} - F_{\perp}}{F_{\parallel} + 2F_{\perp}} \quad (6.1)$$

When i) the fluorophores in the sample are randomly oriented, ii) the rotational diffusion is much slower than fluorescence emission, and iii) the excitation and emission dipole moments overlap, r will have the value of 0.40 [169]. In our experimental configuration, we find on average 0.35. This small deviation stems from depolarized contributions to the signal, see previous subsection. The three-dimensional rotation of individual molecules will induce fluctuations of the anisotropy of a small ensemble. These can be quantified by calculating the (modified) autocorrelation function $C'_r(t)$ of a fluorescence anisotropy time trace. We will refer to this technique as fluorescence anisotropy correlation spectroscopy (FACS). We obtain the ensemble (average) rotation correlation time $\langle \tau_R \rangle$ by adjusting a single exponential to the

autocorrelation function:

$$C'_r(t) = \frac{\langle r(t'+t)r(t') \rangle}{\langle r(t') \rangle^2} - 1 \approx \frac{\langle c_{\text{SM}} \rangle}{N} \exp\left(-\frac{t}{\langle \tau_{\text{R}} \rangle}\right) \quad (6.2)$$

with $\langle c_{\text{SM}} \rangle$ the average contrast of the rotation autocorrelation of the individual molecules, and N the number of molecules in the focus. The fluorophore concentration in FACS is very critical: If chosen too low, shot noise will overcome the rotation fluctuations, while when too high, the autocorrelation contrast will vanish, see Equation (6.2). We choose our concentration 10^{-7} M, so that for the expected film thickness of about $2 \mu\text{m}$, and an excitation spot size of 450 nm (cf. Section 2.3), we will have $N \approx 10$. This means that the maximum achievable contrast (obtained when most molecules sample all orientations so that $\langle c_{\text{SM}} \rangle \approx 1$) will be around 0.10. We note that in a homogeneous liquid, the FACS autocorrelation functions would be exactly single-exponential, because the fluctuations of the fluorescence anisotropy directly probe the three-dimensional rotation of the molecules. If the fluorophores are supposed to be spherical and to rotate isotropically, $\langle \tau_{\text{R}} \rangle$ obeys the Debye-Stokes-Einstein relation:

$$\langle \tau_{\text{R}} \rangle = \frac{V\eta}{k_{\text{B}}T} \quad (6.3)$$

with V the hydrodynamic molecular volume of the fluorophore, η the viscosity of glycerol, and k_{B} Boltzmann's constant. Accordingly, we expect the temperature dependence of the ensemble rotation time to predominantly follow that of the viscosity of glycerol. The temperature relation of the latter can be approximated by a Vogel-Fulcher-Tammann-Hesse (VFTH) law [136,170–172]:

$$\eta = \eta_0 10^{\left(\frac{B}{T - T_0}\right)} \quad (6.4)$$

with $\eta_0 = 7.9 \times 10^{-8} \text{ Pa s}$, $B = 1260 \text{ K}$ and $T_0 = 118 \text{ K}$. The presented parameters are obtained in reference [136] to reproduce shear-force viscosity measurements of glycerol between 213 and 283 K but are found to closely represent the shear-force measured viscosity down to 195 K, close to T_{g} . To relate these parameters to $\langle \tau_{\text{R}} \rangle$ we need to estimate the hydrodynamic molecular volume of PDI. The molecular volume is on the order of 1 nm^3 , but the hydrodynamic molecular volume will be smaller because of the cylindrical shape of the molecule, so that we insert 0.5 nm^3 for V in Equation (6.3). Figure 6.3 shows, on grounds of these parameters, the expected temperature dependence of the rotation correlation time for PDI in glycerol between 190 and 240 K.

6.2.4 Single-molecule analysis

For a single molecule, we can probe part of its rotation directly by following the time evolution of the signals in the parallel and perpendicular (defined by the linearly polarized excitation in the ensemble experiment) detection channels upon circularly polarized laser excitation. Figure 6.1 illustrates that out-of-plane rotational diffusion (along θ) induces fluctuations of the total intensity. However, for in-plane rotational diffusion (along ϕ) the total component will remain unchanged (circularly polarized excitation!) leading to typical anti-correlated fluctuations in the signals of the parallel and perpendicular detection channels. Since the orientation of the fluorophore in the axis system of Figure 6.1 is completely arbitrary, the in-plane and out-of-plane rotational diffusion probe exactly the same set of rotational degrees of freedom. Since the measurement of out-of-plane rotational diffusion requires the analysis of total intensity fluctuations, other processes that influence the total intensity, like photoblinking, undermine quantitative analysis. Therefore, we prefer to probe the in-plane rotational diffusion which is analyzed through the (reduced) linear dichroism A , a quantity that is unaffected by total intensity fluctuations:

$$A = \frac{F_{\parallel} - F_{\perp}}{F_{\parallel} + F_{\perp}} = \cos 2\phi \quad (6.5)$$

Note that in this scheme we cannot distinguish between ϕ and its complementary angle. For this, an additional polarization component (in the xy -plane) should be measured which we have done in a few cases by means of an EOM (Section 6.2.2). This has allowed us to confirm that the observed fluctuations in linear dichroism are indeed related to reorientation of the molecules. However, to determine a rotation correlation time, the linear dichroism suffices. Similarly to the ensemble case, we calculate the modified autocorrelation function $C'_A(t)$ of a linear-dichroism time trace and adjust a single-exponential to obtain the rotation correlation time in the given time window. To prevent normalization issues we correlate the quantity $A + 1$:

$$C'_A(t) = \frac{\langle (A(t' + t) + 1)(A(t') + 1) \rangle}{\langle A(t') + 1 \rangle^2} - 1 \approx c \exp\left(-\frac{t}{\tau_R}\right) \quad (6.6)$$

with c the contrast of the autocorrelation function, which varies between 0 and 1. In the particular case of purely Brownian rotational diffusion, $c = 1$ signifies that all orientations are sampled by the fluorophore. We should note that the linear dichroism, contrary to the fluorescence anisotropy, does not probe the three-dimensional rotation of the fluorophore but a non-trivial

projection of this rotation onto two dimensions (cf. Figure 6.1). As a result, the autocorrelation of the linear dichroism of a homogeneously rotating spherical fluorophore is not even single-exponential [173]. In our case, an additional source of non-exponentiality is the elongated shape of PDI. To analyze the inhomogeneous environments in supercooled glycerol, we need to detect the possibly occurring environmental exchanges as well. For this purpose, we will also determine time traces of the rotation rate. These are retrieved by calculating the in-plane angle change (through Equation 6.5) between two consecutive time bins and dividing the result by the bin time [150].

6.3 Results

6.3.1 Ensemble experiments

We record fluorescence anisotropy time traces of 10^{-7} M PDI in glycerol. Between 190 and 215 K, we apply an observation time of 1800 s and an excitation intensity of 150 W/cm^2 and obtain a time resolution of 10 ms. In the temperature region of 210 to 240 K, we adjust the excitation intensity to 1.5 kW/cm^2 , which allows a time resolution of 1 ms. However, above 220 K we require a time resolution of 30 to 100 μs . This is achieved by averaging the response obtained at 25 different sample positions, for which we pay with a reduced contrast in the autocorrelation functions. Figure 6.2 a shows, as an example, an anisotropy time trace recorded at 206.1 K.

By FACS analysis of the fluctuations in the anisotropy time traces, we obtain a series of autocorrelation functions, a few of which are shown in Figure 6.2 b. The autocorrelation of the non-averaged anisotropy time traces (below 220 K) all show approximately the same contrast of about 0.10 which agrees very well to what we expect on grounds of the concentration and film thickness (cf. Section 6.2.3). Although all autocorrelation curves are clearly non-exponential, we adjust a single-exponential function to obtain the average rotation correlation time for each temperature.

Figure 6.3 presents the resulting ensemble rotation time as a function of temperature, compared to the expected rotation-time temperature dependence based on shear-force viscosity measurements (cf. Section 6.2.3). Between 200 and 240 K, the agreement between expectation and experiment is close to perfect. The data also show that the rotation time does not depend on excitation intensity, as even a FACS measurement at 30 W/cm^2 produces a point right on the model curve. Consequently, the rotation times are exclusively influenced by the relaxation of the host. The ensemble results seem to indicate that on a local scale supercooled glycerol behaves as a liquid with a bulk viscosity. A

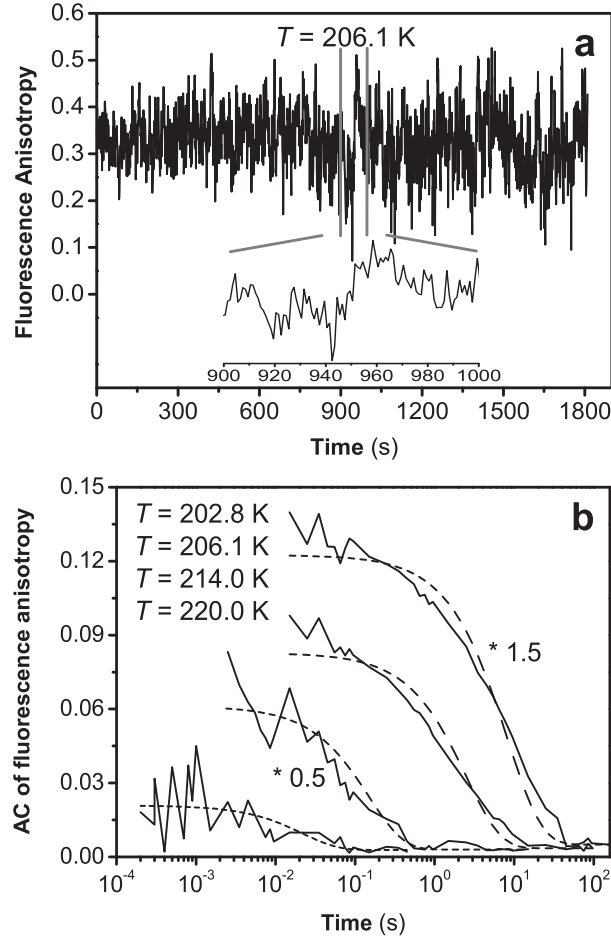


Figure 6.2: Ensemble results: (a) Fluorescence anisotropy time trace recorded at 206.1 K with a time resolution of 1 s and an excitation intensity of 150 W/cm^2 . The average anisotropy is 0.35, reasonably close to the theoretically expected 0.40. The inset shows a magnification of the region between 900 and 1000 s to illustrate that the fluctuations are much larger than shot noise. (b) Autocorrelation functions of the fluorescence anisotropy (FACS) at 202.8, 206.1, 214.0, and 220.0 K along with the best-fitting single-exponential functions. The functions at 202.8 and 214.0 K are multiplied with 1.5 and 0.5, respectively, for reasons of clarity. The time resolution of the original anisotropy time trace was 10 ms at 202.8 and 206.1 K, 1 ms at 214.0 K, and $100 \mu\text{s}$ at 220.0 K. The excitation intensity was 150 W/cm^2 for the two lowest temperatures and 1.5 kW/cm^2 for the highest two. The reduced contrast at 220 K is a result of the averaging procedure to obtain a higher time resolution.

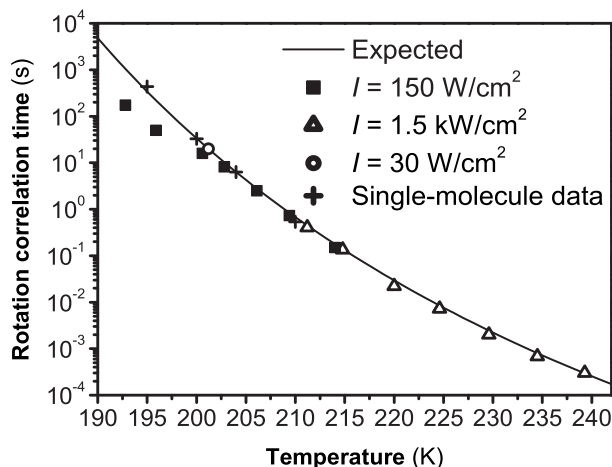


Figure 6.3: The average rotation correlation times obtained by ensemble (FACS) and single-molecule analysis accompanied by a simulation (solid line) based on shear-force viscosity data for glycerol (cf. Section 6.2.3). The ensemble data, at least above 200 K, and the single-molecule data agree well with the solid curve which indicates that the shear-force (large-scale) viscosity predicts the local relaxation of supercooled glycerol very well. The ensemble experiments have been performed at 150 W/cm^2 (squares), 1.5 kW/cm^2 (open triangles), and 30 W/cm^2 (open circle) revealing no excitation-intensity dependence of the rotational diffusion. Below 200 K the ensemble data start to deviate from the model curve. We attribute this to photobleaching making the rotation times appear shorter than these actually are. This is confirmed by the single-molecule data, where we can discard fast bleaching molecules. In that case, the average single-molecule rotation times follow the solid line up to 195 K.

similar behavior has been observed for the liquid *ortho*-terphenyl [145] and for the polymer poly(methyl acrylate) [151]. From the rotation-time temperature dependence, we can also conclude that the water content of our glycerol films is negligible, since our data scale with shear-force viscosity measurements that have been obtained on glycerol that had a water content of less than 0.1% [136].

At 200 K and lower, the apparent rotation times become shorter than expected on grounds of the shear-force viscosity. We attribute this to the onset of photobleaching events which become shorter than the average rotation correlation time. Although the fluorescence anisotropy (cf. Equation (6.1)) is in principle independent of intensity, a bleaching (or blinking) event will have the same effect as a molecule turning its dipole moment to the axis orthogonal to that of the laser polarization. Obviously, this makes the rotation times appear shorter than they actually are. Since in a single-molecule experiment, we can discard

these fast bleaching molecules, we will be able to explore the region close to T_g more reliably.

6.3.2 Single-molecule experiments at static temperatures

In the static-temperature, single-molecule experiments, we obtain confocally scanned fluorescence images at a given cryostat temperature, from which we select the single molecules for analysis. For each single molecule, we record time traces of two orthogonally polarized fluorescence components and determine from these the reduced linear dichroism and the rotation rate. We perform autocorrelation analysis to retrieve rotation correlation times and we analyze the rotation rate for jumps indicating environmental exchanges. Such analysis is performed on 24 molecules at 195 K, 51 at 200 K, 70 at 204 K, and 83 at 210 K. The temperature window corresponds to $T_g + 5$ K to $T_g + 20$ K ($T_g = 190$ K). The excitation laser light is circularly polarized. The excitation intensity, the time resolution, the observation time, and the measurement procedure of the time traces are adjusted to the expected rotation time. At

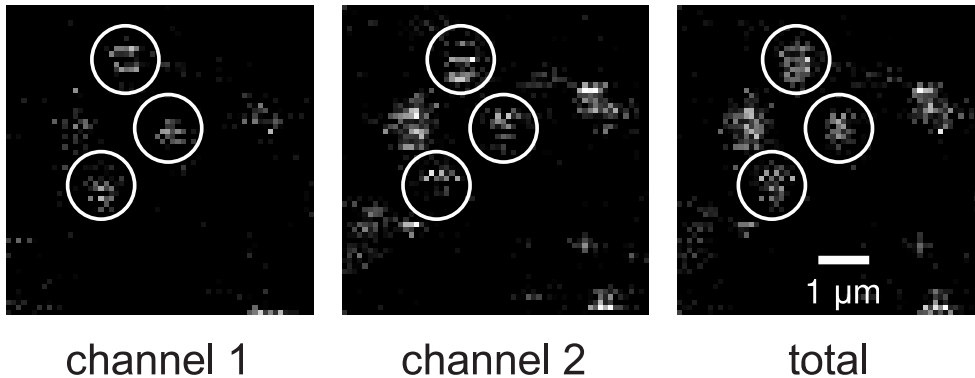


Figure 6.4: $6 \times 6 \mu\text{m}^2$ confocally scanned images of 10^{-9} M PDI in glycerol at 209.6 K recorded with a resolution of 10 ms/point and 100 nm/point at an excitation intensity of 4.5 kW/cm^2 . The intensity scale is a linear gray scale between 20 and 100 counts/10 ms for the two orthogonally polarized fluorescence images (left and center image), and between 40 and 150 counts/10 ms for the sum of these two images. In the polarized images, the intensity in the line scans of the three bright spots is clearly anti-correlated, which is the fingerprint of single-molecule rotational diffusion (cf. Section 6.2.4). The anti-correlation is confirmed in the right (“total”) image, showing the sum of the two orthogonal polarized fluorescence images, where nearly Gaussian spots are retrieved. The remaining noisy, blinking-like appearance is caused by out-of-plane rotation.

204 and 210 K, the fluorescence time traces are recorded at 150 W/cm^2 with a time resolution of 100 ms and an observation time of 300 s (204 K) and 180 s (210 K) or sometimes shorter due to photobleaching. At 195 and 200 K, observation times are so long that we cannot excite the molecules continuously. At 200 K, we repeatedly probe a molecule for 0.5 s at 150 W/cm^2 and keep it subsequently for 2 s in the dark. The total experimental duration time per molecule is 3600 s (with an illumination time of 720 s). At 195 K, we probe the molecule for 1 s at 75 W/cm^2 and keep it in the dark for 19 s. The total experimental duration time is 7200 s (longer is not possible in our experimental configuration).

Figure 6.4 shows typical examples of fluorescence images revealing single molecules. Since these particular images have been recorded at 209.6 K, the fluorophores have had the opportunity to reorient during scanning. This leads to anti-correlated, striped spots in the two orthogonally polarized fluorescence images. When the two images are added, the stripes disappear revealing nearly Gaussian spots, that are still rather noisy due to out-of-plane rotational diffusion. The anti-correlation is also apparent in the fluorescence time traces, of which Figure 6.5 a shows an example at 204.4 K. To illustrate the anti-correlation,

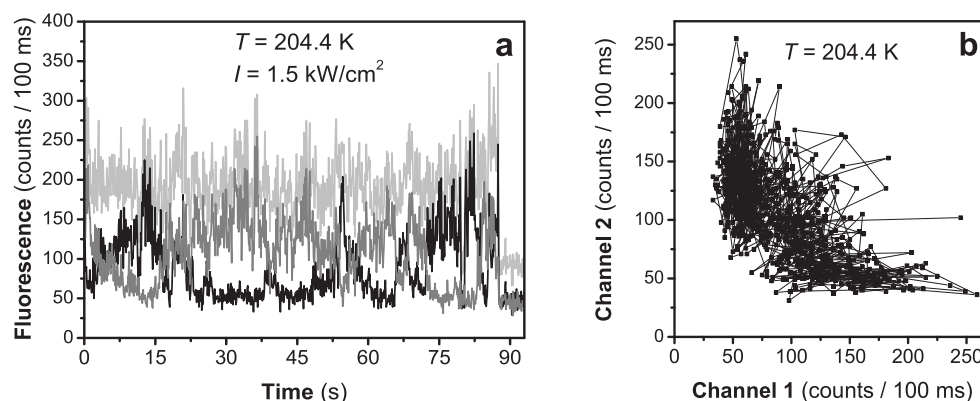


Figure 6.5: (a) Single-molecule fluorescence time traces revealing rotational diffusion: The black and the dark-grey traces show the fluorescence response in two orthogonally polarized fluorescence detection channels revealing anti-correlation, the signature of in-plane single-molecule rotational diffusion (cf. Section 6.2.4). The light-gray trace is the sum of the two orthogonally polarized traces. Its fluctuations are related to out-of-plane rotational diffusion. (b) Correlation plot of the two orthogonally polarized fluorescence traces of (a) to illustrate the observed anti-correlation. Please note that a constant fluorescence signal with random angle ϕ would give a line with slope -1 in this plot.

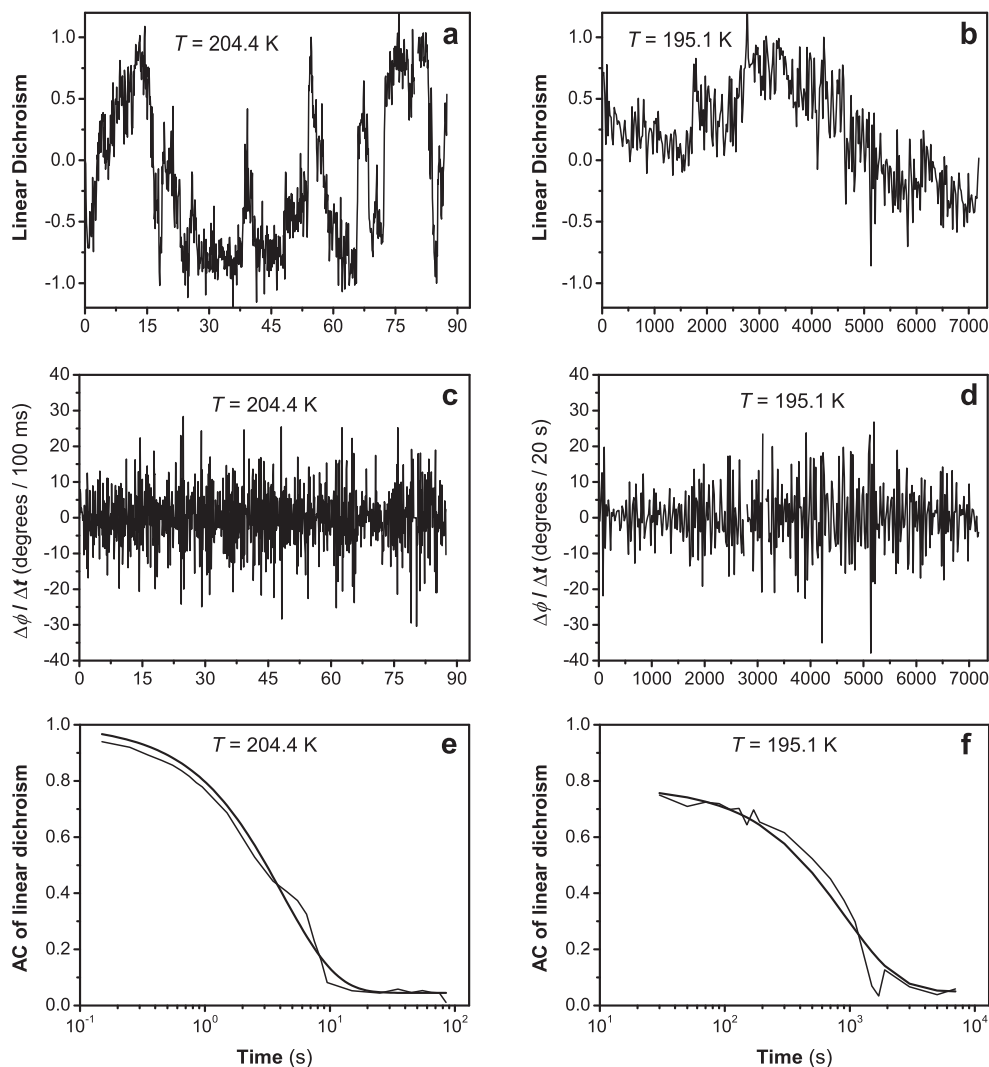


Figure 6.6: Single-molecule analysis: Two examples of single-molecule time traces of the reduced linear dichroism (a and b) and the rotation rate (c and d) at 204.4 K and 195.1 K. The data at 204.4 K stem from the time traces shown in Figure 6.5. The molecule at 204.4 K clearly samples the full angular space (a) and shows no exchanges of environment (c). On the other hand, the molecule at 195.1 K seems not to sample the complete angular space anymore (b) but it also undergoes no environmental exchanges (d). Plots (e) and (f) show the autocorrelation functions calculated from the linear dichroism traces of (a) and (b). In both cases, the functions are very close to their single-exponential fits, another indication that the environment is largely preserved throughout the observed time window.

Figure 6.5 b shows the two orthogonally polarized fluorescence traces in a correlation plot.

From the orthogonally polarized fluorescence traces, we calculate the reduced linear dichroism and the rotation rate (cf. Section 6.2.4). Figure 6.6 shows an example at 204.4 K (same data as Figure 6.5) and 195.1 K. The linear-dichroism data (Figures 6.6 a and b) at those two temperatures are distinctly different. Apart from the completely different time scales of the rotational diffusion, the fluorophore at 204.4 K clearly samples all orientations within the glycerol, while this is not the case for the one at 195.1 K. Upon analysis of all our data, we find that, at 204 and 210 K, virtually all molecules sample all possible orientations. At 200 K, we find already a significant amount (about 20 %) to present restricted orientational diffusion, while this fraction approaches 100 % at 195 K.

Figures 6.6 c and d show rotation-rate time traces. If the rotating molecule experienced an (observable) change of its environment, its rotational diffusion would either become easier or more difficult leading to either larger or smaller excursions of its rotation rate. In both traces, we see that the rotation rate does not reveal any distinct changes in its amplitude. This is not only the

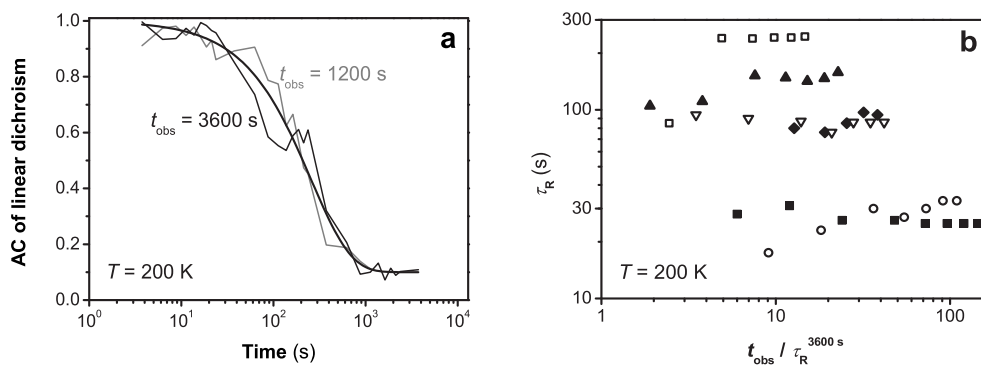


Figure 6.7: Illustration of the absence of environmental exchanges: (a) Autocorrelation functions of the same individual molecule at 200 K calculated from data points of the first 1200 s and from the complete time trace (3600 s). Both autocorrelation functions are fitted by the same single-exponential indicating the absence of environmental exchanges during observation. (b) Six sets of single-molecule rotation times as a function of the single-molecule observation time. The time axis shows the observation time normalized to the single-molecule rotation time obtained after an experimental duration of 3600 s, by which the axis basically gives the “number of effective rotations”. None of the six sets shows any sign of an environmental exchange. The lower value of the rotation time that is sometimes observed for short observation times (a few rotations) is related to the limited experimental time.

case for these data, but for all our data at the four temperatures. In some cases, we have observed for up to 300 times the average rotation time, and still found no jump in rotation rate. Figure 6.7 presents a more quantitative illustration of the absence of environmental exchanges. The figure shows the observation-time dependence of the rotation time of six individual molecules at 200 K. Although the rotation times are clearly broadly spread from molecule to molecule, not a single environmental exchange is observed. Therefore, we can conclude that the environmental exchanges in glycerol, if present at all, are at least 100 times slower than the average rotation times and thus significantly slower than the ones in the different glass formers investigated by Deschenes and Vanden Bout [14, 145, 150, 151] (cf. Section 6.1).

Since no environmental exchanges are present that significantly influence the data, rotation correlation times of each single molecule are determined from a full-length autocorrelation function of its reduced linear dichroism. Figures 6.6 e and f show two examples. We find the majority of the single-molecule autocorrelation functions, regardless of the temperature, to be very close to a single exponential, but we do observe a broad distribution of the rotation rates at each temperature. This again strongly suggests that the environments of the fluorophores, although clearly inhomogeneous, are completely preserved

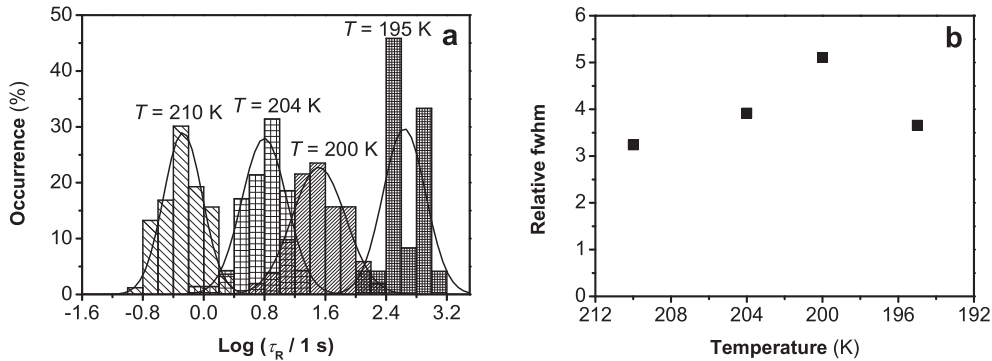


Figure 6.8: (a) Histograms of the single-molecule rotation times obtained at 210, 204, 200, and 195 K plotted on a logarithmic axis. The histograms stem from 83 molecules at 210 K, 70 at 204 K, 51 at 200 K, and 24 at 195 K. The first three histograms are reasonably fitted by a Gaussian distribution of $\log(\tau_R)$ yielding average rotation times of 535 ms, 6.28 s and 32.7 s. The last histogram, at 195 K, does not represent a distinct Gaussian shape but we fit one nonetheless to determine the average of the distribution, 435 s. The four averages are compared in Figure 6.3 to the ensemble data and agree well with them. (b) Plot of the full-width at half-maximum (fwhm) relative to the average of each distribution as a function of temperature. Except for the data at 195 K, the plot suggests that the distributions broaden towards lower temperature.

throughout our experimental window, on average 100 rotation periods. Figure 6.8 a shows histograms of the resulting single-molecule rotation times at 210, 204, 200, and 195 K. The distributions are fit by Gaussian distributions of $\log(\tau_R)$. From these fits, we determine the average rotation time at each of the four temperatures. These average rotation times are compared in Figure 6.3 to the ensemble data and found to agree very well with them. This indicates that the single-molecule experiments probe a comparable set of rotating molecules as the ensemble experiments. The fact that the average at 195 K is still on the model curve, confirms that photobleaching has caused the underestimation of the rotation times in the ensemble data below 200 K. The distributions in Figure 6.8 a appear to broaden from 210 to 200 K, as is indicated in Figure 6.8 b. This trend is discontinued at 195 K, but we think that this is an experimental artifact due to the small amount of events and the limited observation time.

6.3.3 Single-molecule experiments at variable temperatures

Until now, our single-molecule analysis has been similar to that of Deschenes and Vanden Bout [150] (cf. Section 6.1), albeit over a much broader dynamic range. Here, we present an additional study of the rotational diffusion of individual molecules as a function of the (cryostat) temperature. For the variable-temperature analysis, it is crucial to find the same molecules back at each temperature. Figure 6.9 shows a series of total-fluorescence ($F_{\parallel} + F_{\perp}$) images at the same sample position at the applied temperatures of 205.0, 207.5, 210.0, and 212.5 K. The images clearly reveal identical spots and illustrate our ability to follow the same single molecule throughout this temperature window. An other constraint to the experiment is that a reasonable fraction of the molecules should survive until the end. Therefore, the temperature window is limited to about 215 K on the high side, because at more elevated temperatures such high excitation intensities are required to obtain the rotation time that photobleaching becomes significant. On the other side, at temperatures lower than 205 K, the required observation times become so long that only a few molecules could be studied per day. Given these considerations, we analyze the rotational diffusion of the same single molecules at 205.0, 207.5, 210.0, and 212.5 K. The experimental settings are adjusted to the expected rotation time and are: an observation time of, respectively, 30, 10, 3, and 2 s for 205.0 to 212.5 K, a time resolution of 100, 30, 3, and 2 ms, and an excitation intensity of 150, 450, 1500 and 3000 W/cm². During the experiment, we find 105 molecules of 142 to survive until the end, of which 69 yield autocorrelation functions with reasonable signal-to-noise given the rather short linear dichro-

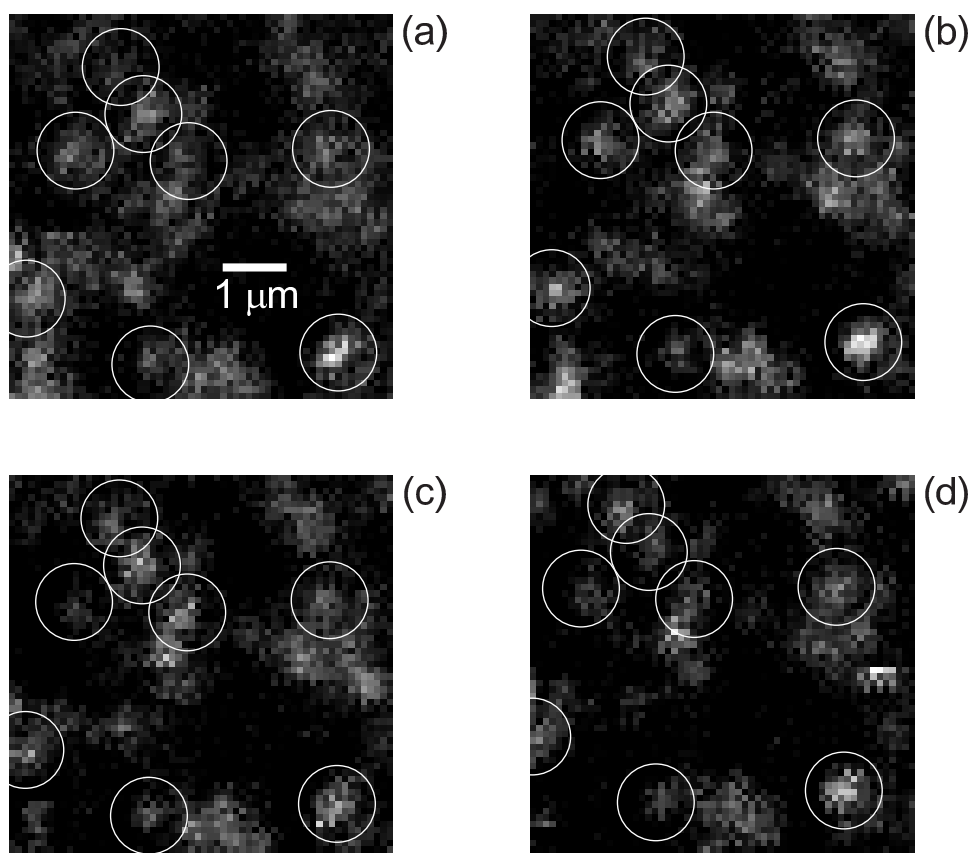


Figure 6.9: Four $6 \times 6 \mu\text{m}^2$ confocally scanned total-fluorescence images of the same sample position at 205.0 (a), 207.5 (b), 210.0 (c), and 212.5 K (d). Although the images look rather noisy, due to out-of-plane rotation, several isolated spots are discernable throughout the complete temperature range. The molecules that have been used for further analysis are indicated with white circles. The intensity scale is a linear gray scale between 20 and 200 counts/10 ms. The resolution is 10 ms/point and 100 nm/point and the excitation intensity $1.5 \text{ kW}/\text{cm}^2$.

ism traces. Figure 6.10 shows three series of autocorrelation functions at the four temperature for a fast, a medium, and a slow rotating molecule. Like in the static-temperature experiments, the autocorrelation functions are again close to a single exponential. To establish that we are probing a representative subset of molecules, we construct histograms of the obtained rotation correlation times of the 69 molecules at the four temperatures (data not shown). We find them quite similar to the histograms obtained in the static temperature experiments.

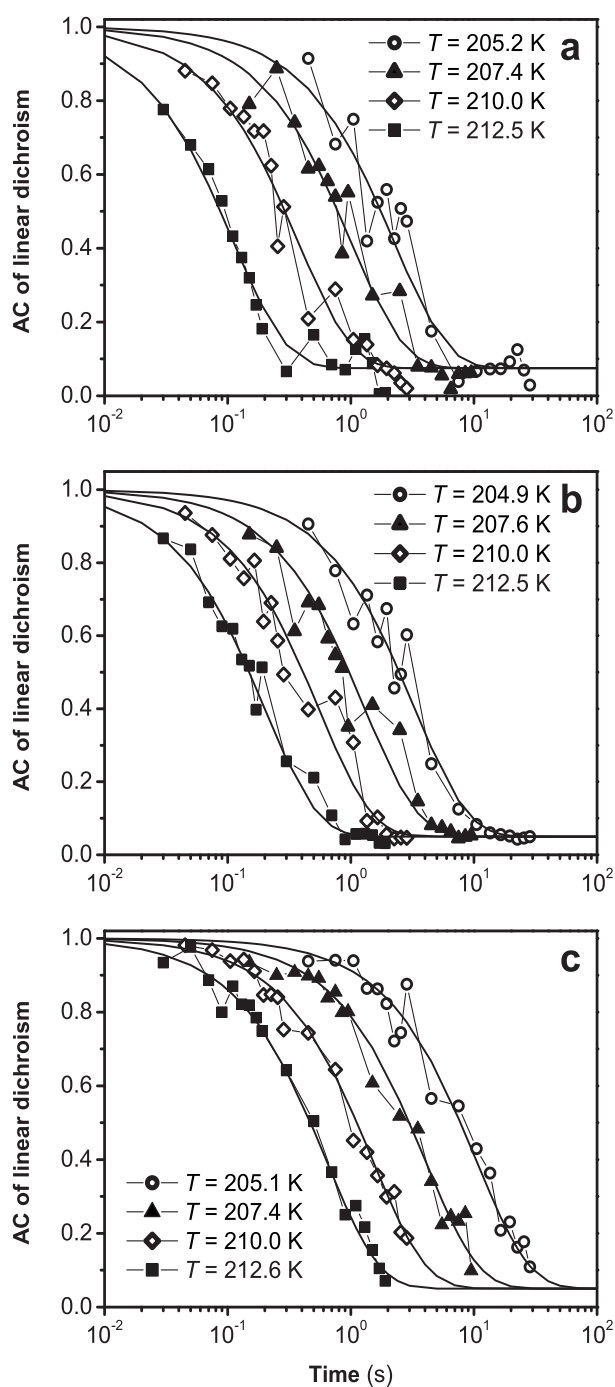


Figure 6.10: Three examples of autocorrelation functions obtained from the reduced linear dichroism of the same individual molecules at 205, 207.5, 210, and 212.5 K. The functions in (a) reveal rotation times faster than average, the ones in (b) are approximately average, and the ones in (c) are clearly slower.

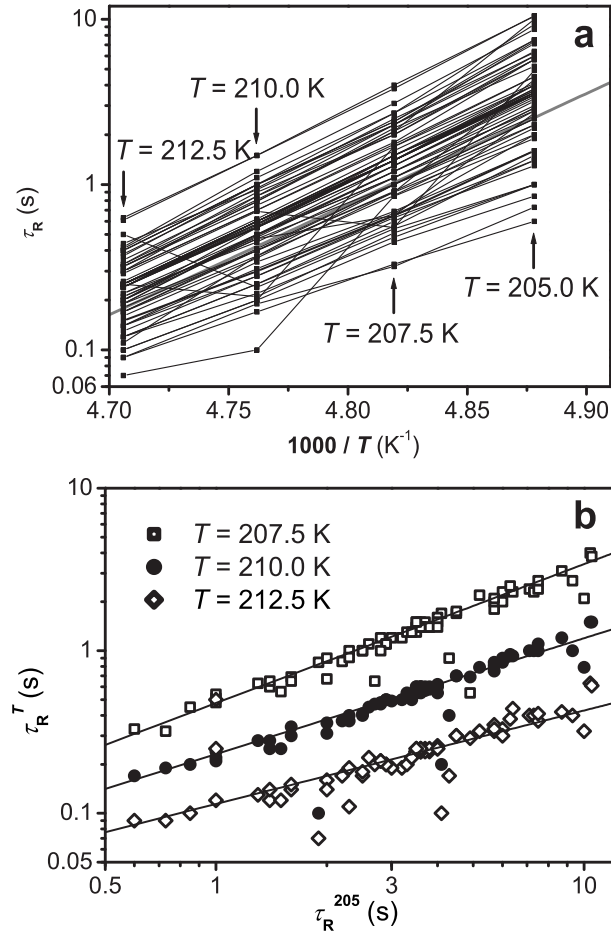


Figure 6.11: Results of the variable-temperature single-molecule experiments: (a) Arrhenius-like plot of all rotation times obtained from the 69 analyzed individual molecules. The grey line indicates the average which agrees well with the model curve in Figure 6.3. Although the complete experimental time is about 5 hours, only few of the molecules show an abrupt change in their temperature dependence which means that even at 212.5 K the spatial inhomogeneities persist for hours. Furthermore, the plot indicates the tendency of the distribution of rotation times to narrow down at higher temperatures. (b) Correlation plot between the single-molecule rotation times at 205.0 K and those at the three higher temperatures. This plot contains the same information but presents it in a more perceivable way. First of all, there is a very strong correlation, meaning that slow molecules remain slow and fast ones remain fast. Second, the slope of the correlation is clearly increasing towards lower temperatures indicating a gradually increasing dispersion of the single-molecule rotation times.

Figure 6.11 shows the resulting rotation-time temperature dependences of the 69 remaining molecules in two ways. Figure 6.11 a presents them Arrhenius-like, the log of the rotation time as a function of the inverse of the temperature. This curve illustrates that only a few of the molecules show jumps in their rotation times. This is an important observation because it means that we are probing the temperature dependence of rotational diffusion of individual molecules within a fixed environment. This indicates that the average environmental exchange time has to be a few hours even at 212.5 K, i.e., at least 10^5 times slower than the average rotation time! Unfortunately, the temperature interval from 205.0 to 212.5 K is so small, that only a slope and an offset can be fitted which makes it impossible to distinguish between the various laws, Arrhenius, VFTH, or others. Therefore, we can only present a qualitative analysis of the single-molecule rotation temperature dependence. To illustrate this dependence, Figure 6.11 b shows the same data in a correlation plot between the rotation time at 205.0 K and the ones at 207.5, 210.0, and 212.5 K. This plot reveals a strong correlation, i.e., the slow molecules remain slow and the fast ones remain fast. This memory is a direct consequence of the absence of environmental exchanges on our experimental time scale. We also observe that the rotation-time distributions clearly broaden towards lower temperatures. This was already suggested by the static-temperature experiments, but the variable-temperature data show it more convincingly. Furthermore, they also reveal that this dispersion from the average is a gradual process for each individual molecule.

6.4 Discussion

Comparing our data on supercooled glycerol to those of Deschenes and Vanden Bout on the fragile glass former *ortho*-terphenyl [145] (cf. Introduction, both experiments are in the same temperature regime relative to T_g), we find that the data agree on the whole: We also observe a VFTH-like dependence of the ensemble rotation times, a broad distribution of single-molecule rotation times, and a broadening of these distributions towards T_g . Additionally to their conclusions, we have shown this broadening to be related to a smoothly increasing dispersion of the single-molecule rotation times upon approach of T_g . Clearly, both *ortho*-terphenyl and glycerol reveal the presence of spatially inhomogeneous relaxation dynamics. However, we also find one important difference, namely that the environmental exchanges in glycerol are at least three to four orders of magnitude slower than in *ortho*-terphenyl. Since the conservation of inhomogeneous regions for hours in a completely fluid environ-

ment seems highly unlikely, we have to suppose the presence of both fluid and “solid” structures in supercooled glycerol. (These structures should be rigid at least on the timescale of the environmental exchanges.)

Before we can address any implications of these solid structures on the properties of glycerol, we have to rule out that they are probe-induced. In principle, one could imagine that glycerol might form a persistent solvation shell around the fluorophore and that the resulting structure would rotate as a whole in an otherwise homogeneous liquid. The spread in rotation times would then not stem from different environments, but from a distribution in the size of the rotating entities. We can discard this explanation on two grounds: i) According to Equation (6.3), we expect a spread in hydrodynamic molecular volume of the rotators to lead to a spread in the offsets and not in the slopes of the rotation times versus temperature, contrary to what we observe in Figure 6.11 a; ii) We should find a much larger absolute value for the average hydrodynamic molecular volume than that of a typical organic fluorophore (cf. Figure 6.3).

We therefore conclude that the postulated solid domains are intrinsic to glycerol. Both the ensemble and single-molecule experiments suggest that the fluorophores are exclusively in a liquid-like environment at least at temperatures higher than 200 K. At these temperatures, we do not find any fluorophores in solid domains. This segregation seems reasonable since there are distinct structural and chemical differences between the probe and the host. We do not expect PDI to form strong hydrogen bonds with glycerol.

We will now try to account for the emergence of glassy domains by using concepts from glass-formation theories. We start from the Adam and Gibbs concept of cooperativity [139]. Differences in size of cooperative regions will result in spatially inhomogeneous dynamics. It is not clear that this cooperativity model would account for the large difference between microscopic relaxation times and the extremely long exchanges we have observed. Let us now consider the free volume model of Cohen and Turnbull [174]. The free volume is the amount of space in the sample that is not occupied by molecules. Relaxation can only occur if sufficient free volume is present for a molecule to change its position. The free volume in the system is supposed to go down with decreasing temperature in the fashion of a standard thermally induced volume contraction. In this view, cooperativity can be seen as molecules sharing their accessible free volume to allow motion of one of them. A crucial ingredient is the assumption that the free volume exchange presents self-inhibitory dynamics [175]. As soon as a given cooperative region does not contain enough free volume for relaxation to occur, it comes to a dynamical arrest. This state is long-lived, because the arrest itself inhibits the entrance

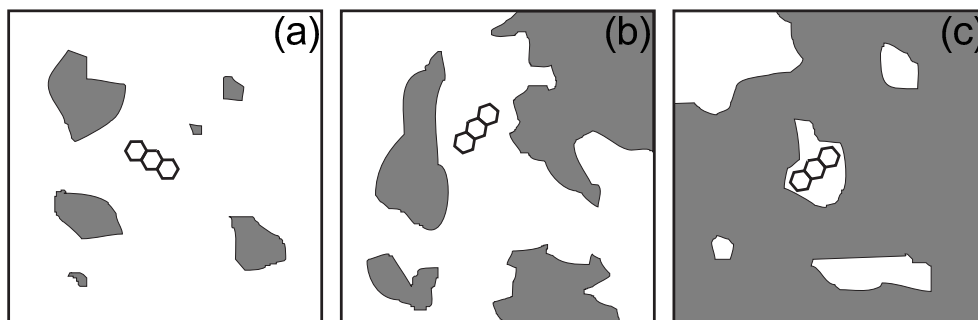


Figure 6.12: An artist’s impression of solid domains in a supercooled liquid, at (a) a high temperature where they are still small and their influence on the relaxation dynamics in the fluid is negligible; (b) a medium temperature where they have grown significantly but the overall structure is still that of a liquid; and (c) a lower temperature where the structure has become completely solid with ever shrinking fluid lakes. The anthracene molecule indicates a fluorophore. Obviously, its rotational diffusion will increasingly be affected by the solid domains when going from (a) to (c).

of free volume. Therefore, the self-inhibitory character may naturally explain the occurrence of two very different timescales. The afore-described model is qualitative, a more quantitative picture may be expected from mode-coupling theory (MCT). MCT analysis has, for instance, been successfully applied to explain the dielectric permittivity spectrum of glycerol [176, 177]. Recently, Götze *et al.* have performed MCT calculations on the colloidal glass transition [178]. They found that the onset of glass formation depends very critically on the volume fraction and the interaction strength of the colloids. Such a formalism may also be applicable to predict the influence of the solid domains in glycerol on glass formation. However, it remains difficult to relate the outcome of MCT analysis to a microscopic picture of the glass-forming system.

Until now, we have not included temperature in our discussion. We expect the average size of the solid domains to increase with decreasing temperature, as a direct result of the decrease of available free volume. Consequently, we propose the following scenario for glass formation, which is schematically drawn in Figure 6.12. At high temperatures, free volume is still abundant in the supercooled liquid, which behaves as a purely Newtonian liquid. Only small solid domains are occasionally formed and quickly disappear. At lower temperature, free volume becomes scarcer and the solid domains grow, possibly until they contain a significant fraction of the glycerol molecules. As long as interactions between the domains are negligible, the system will still behave as a liquid with a modified viscosity. The viscosity of such a colloidal suspension

is given by the Einstein-Roscoe equation [179–182]:

$$\eta = \eta_0 \left(1 - \frac{f}{f_\infty}\right)^{-2.5} \quad (6.7)$$

with η_0 the intrinsic viscosity of the liquid, f the volume fraction of the glassy particles in the liquid, and f_∞ the volume fraction at which the viscosity becomes infinite which is 0.74 for uniformly spherical particles [181]. This correction factor becomes significant only for large volume fractions and would therefore be difficult to notice on the logarithmic scale of shear-force viscosity measurements. Finally, at still lower temperatures, the solid domains reach percolation and the system resembles a macroscopic solid with ever shrinking liquid lakes.

Our scenario for glass formation leaves many questions open. First, when does the actual glass transition occur? It will not be before the percolation of the solid domains. However, it is possible that the percolating structure is too fragile at this point to significantly affect the shear-force viscosity measurements that are usually performed at relatively large shear rates [136–138]. The other extreme would be the temperature at which all fluid domains have disappeared. Second, how do we relate our measurements to this scenario? At the highest temperature, all molecules see the pervading liquid phase: dynamics are homogeneous. Our variable-temperature, single-molecule results (cf. Figure 6.11) suggest that this regime exists down to 225 K ($T_g + 35$ K), since the data seem to converge at this temperature when all individual single-molecule temperature dependences (cf. Figure 6.11 a) are fitted with an Arrhenius law (fits not shown). This homogeneous situation should persist as long as communication between liquid pockets remains easy. At some temperature, liquid pockets do not exchange free volume anymore. Consequently, they start to present different local viscosities and heterogeneity appears in the probe rotation times. When the size of the liquid lakes becomes comparable to that of the probe, the rotation starts to be hindered. Our results indicate that this is predominantly the case at 195 K, 5 K above T_g . Eventually, all probes are frozen at low enough temperature. Third, is this scenario consistent with previous measurements on ensembles? Strong support for the intrinsic heterogeneity of the liquid pockets comes from NMR and dielectric hole-burning experiments [138, 153–155]. Although they do not involve probe molecules, these methods indicate a broad distribution of the fluid-like relaxation times in glycerol up to 20 K above T_g . However, none of these report environmental exchange times as long as found here. In these ensemble experiments, the slow environmental exchanges could easily be hidden, since they had to be

detected as a slow change of a much faster fluctuating variable. Furthermore, at least NMR is intrinsically not sensitive to very slow changes. Apparently, a single-molecule approach proves crucial to observe the persistence of the inhomogeneous environments.

The slow environmental exchanges in glycerol suggest that already around 215 K the solid domains have percolated (Figure 6.12 c). However, this seems contradictory with the overall liquid picture suggested by shear-force viscosity measurements [136–138]. An obvious possibility is that the percolating system behaves as a yield-stress solid. To verify this proposition and thereby present an independent proof of our domain model, we plan to measure the compliance of glycerol at much lower shear rates than those applied in the standard shear-force measurements (10^{-6} instead of 10^{-2} rad/s). If our model is correct, we expect to find a regime at lower shear rates where glycerol behaves as a solid, i.e., as soon as the shear becomes too weak to break the domains apart. At even lower shear, glycerol is expected to become liquid-like again, when the shear rate no longer exceeds the environmental exchange rate. Similar effects have been observed in force measurements on colloidal clay [183, 184] and carbon/oil suspensions [185].

Since glass formation is a general phenomenon, we believe that our domain picture should also apply to most other glass formers. However, the exchange rate between glassy and fluid domains may differ from system to system, related to the nature (strength) of the intermolecular interactions, the absolute temperature, and other specific factors. In that view, the very slow relaxation of the glassy domains in glycerol may very well be an extreme. However, its observation is crucial because it convincingly shows that a model describing a glass-forming liquid has to present two distinct timescales of α relaxation. We have shown that the self-inhibitory character of the α relaxation explains these two timescales. It seems natural to replace the mosaic picture of Deschenes and Vanden Bout with our domain model to account for the spatially inhomogeneous dynamics in *ortho*-terphenyl [145] (see Introduction). Additional support for the domain picture comes from the work of Weeks *et al.* [186] on the glass transition of colloidal suspensions. Here, the building blocks are not molecules but micron-sized beads. Accordingly, the translational diffusion of each single unit can be directly observed by optical microscopy. In the super-cooled state, Weeks *et al.* found only a small fraction of very mobile particles, while the majority of the molecules hardly moved. From time to time, exchanges were observed between the fluid and glassy domains, but these were on a distinctly slower timescale than the relaxation in the fluid domains.

6.5 Conclusion

We have performed ensemble and single-molecule experiments to analyze rotational diffusion of a fluorophore (PDI) in supercooled glycerol, 5 to 50 K above its glass-transition temperature of 190 K. We have used rotational diffusion as a probe for relaxation in the glycerol. Although we found the average rotation times to agree with the macroscopic viscosity, we have observed a broad distribution of single-molecule rotation times, related to the presence of spatial inhomogeneities in the liquid. Contrary to other systems, the exchange of the environments was found to be much slower than the experimental time. This allowed us to study the rotational diffusion of individual molecules as a function of temperature. Although the temperature window was rather limited, we have been able to establish that the individual rotation times smoothly diverge from the average upon approaching T_g , thereby supplying a single-molecule picture to the broadening of the rotation-time distributions on the road to glass formation.

To account for our results we have postulated the presence of solid domains in glycerol. These solid domains are the result of a subtle interplay between molecular cooperativity and the self-inhibitory character of the relaxation dynamics. We have argued that as long as these solid domains do not interact, the bulk character of the system will stay liquid-like with a finite viscosity as observed in shear-force viscosity measurements. We have shown that the fluorophores are segregated into the fluid regions. The solid domains divide the liquid region into pockets with different local relaxation dynamics. This picture of solid boundaries accounts for the extremely slow environmental relaxation in glycerol. This picture should also apply to other glass-forming systems, although the extreme differences in timescale between local relaxation and environmental exchanges in supercooled glycerol have been instrumental to convincingly support the domain model.

Acknowledgements

The author wishes to thank J. Berkhout who, during his master research project (ON 4), carried out a significant part of the experiments, and Dr. M. Lipitz for the development of the data-acquisition software and his continuing support. Further, he acknowledges helpful discussions with Prof. M. E. Cates, Prof. W. van Saarloos, and Dr. C. Storm.

7 Demonstration of laser-driven microsecond temperature cycles

abstract – We demonstrate a novel technique to achieve fast thermal cycles of a small sample (a few femtoliters): Modulating a continuous near-infrared laser focused on a metal film, we can drive the local temperature from 130 K to 300 K and back, within a few microseconds. By fluorescence microscopy of dyes in a thin glycerol film, we record images of the hot spot, calibrate its temperature, and follow its variations in real time. The temperature-dependence of fluorescence anisotropy, due to photoblinking and rotational diffusion, gives a steady-state temperature calibration between 200 and 350 K. From 200 to 220 K, we monitor temperature more accurately by fluorescence autocorrelation, a probe for rotational diffusion. Time-resolved measurements of fluorescence anisotropy give heating and cooling times of a few microseconds, short enough to supercool pure water. We designed our method to repeatedly cycle a single (bio-)molecule between ambient and cryostat temperatures with microsecond time-resolution. Successive measurements of a structurally relevant variable will decompose a dynamical process into structural snapshots. Such temperature-cycle experiments which combine a high time resolution with long observation times can thus be expected to yield new insights into complex processes such as protein folding.

The contents of this chapter will be published:

R. Zondervan, F. Kulzer, H. van der Meer, J. A. J. M. Disselhorst, M. Orrit, *accepted for publication in Biophys. J.*

7.1 Introduction

In Section 1.3 we have introduced the temperature-cycle concept. In this chapter we demonstrate and characterize the proposed laser-induced temperature cycles between 130 K and ambient temperature. To determine the efficiency of the laser-induced local heating, we optically measure the spatial temperature profile of the hot spot, and the kinetics of heating and cooling. In Chapter 5, we have tried Raman scattering from poly(methyl methacrylate) cover slides, coated by an absorbing metal film. This technique probes the local temperature rather accurately (up to ± 1 K), but requires minutes of acquisition. Translational and rotational diffusion of fluorophores are two other optically accessible quantities depending on temperature. This dependence can be extended to a broader temperature range in glassy and supercooled liquid matrices such as glycerol, in which the viscosity varies by many orders of magnitude between 200 and 350 K [132, 133, 136, 137]. Translational diffusion is often measured by fluorescence correlation spectroscopy (FCS), which has the disadvantage that the observed diffusion time depends on the effective focal volume [187, 188]. Rotational diffusion is a more convenient probe of local temperature, because it only depends on intrinsic parameters. It leads to a reduction of the steady-state fluorescence anisotropy when the rotation time approaches the fluorescence lifetime [169]. At lower temperatures and low fluorophore concentration, rotational diffusion of the emitters induces observable fluctuations in fluorescence polarization that yield the characteristic rotation time through autocorrelation analysis (fluorescence anisotropy correlation spectroscopy, FACS) [165–167]. We have used FACS already in Chapter 6 and we apply it here to provide for an additional temperature calibration.

In this work, laser-induced local heating is visualized and characterized at a cryostat temperature of 130 K by fluorescence and fluorescence anisotropy imaging experiments of a rhodamine 6G (R6G) solution in glycerol deposited on an absorbing substrate. The fluorescence (anisotropy) of R6G in glycerol is mainly a probe of rotational diffusion, but is also affected by photoblinking. This leads to a continuous change of steady-state anisotropy with temperature above 200 K. A more accurate temperature calibration between 200 and 220 K is provided by FACS measurements on perylenedicarboximide (PDI) in glycerol. Finally, the heating and cooling kinetics in the center of the laser-induced hot spot are studied in real-time by the fast responses of both the fluorescence intensity and the fluorescence anisotropy of R6G in glycerol.

7.2 Experimental

The setup to perform the temperature cycles is presented in Chapter 2. For their demonstration, we perform steady-state fluorescence anisotropy measurements on 10^{-5} M R6G in glycerol and FACS experiments on 10^{-6} M PDI in glycerol. The sample preparation is equal to that described in Section 6.2.1.

7.3 Theory – temperature measurements through molecular diffusion

The viscosity of glycerol increases by ten orders of magnitude between room temperature and its glass-transition temperature (190 K), which makes for an extremely sensitive temperature probe [136, 137]. The exact temperature dependence of the viscosity η of glycerol can be approximated by a Vogel-Fulcher-Tammann-Hesse (VFTH) law [136, 170–172]:

$$\eta = \eta_0 10^{\left(\frac{B}{T - T_0}\right)} \quad (7.1)$$

with below 283 K, $\eta_0 = 7.9 \times 10^{-8}$ Pa s, $B = 1260$ K, $T_0 = 118$ K, and above 283 K, $\eta_0 = 3.54 \times 10^{-6}$ Pa s, $B = 780$ K, $T_0 = 153$ K [136]. (The treatment follows that of Section 6.2.3.)

In this work, we visualize the temperature dependence of the viscosity through the rotation of fluorescent molecules in glycerol. Supposing the fluorophores to rotate isotropically, we obtain the following expression for the rotation correlation time τ_R [169]:

$$\tau_R = \frac{V\eta}{k_B T} \quad (7.2)$$

with V the hydrodynamic molecular volume, 0.419 nm^3 for rhodamine 610 (a molecule quite similar to R6G) [189] and k_B the Boltzmann constant. The “rotation” curve in Figure 7.1 shows the expected rotation correlation time of a typical organic fluorophore (rhodamine 610) in glycerol between 190 and 360 K based on Equations (7.1) and (7.2). The experimental points obtained in the ensemble study of the rotational diffusion of PDI in glycerol, which are discussed in Section 6.3.1, are also indicated (squares).

The rotation correlation time of a fluorophore can be measured through the steady-state fluorescence anisotropy r , when this time is on the order of the fluorescence lifetime [169]. The anisotropy is the normalized difference between

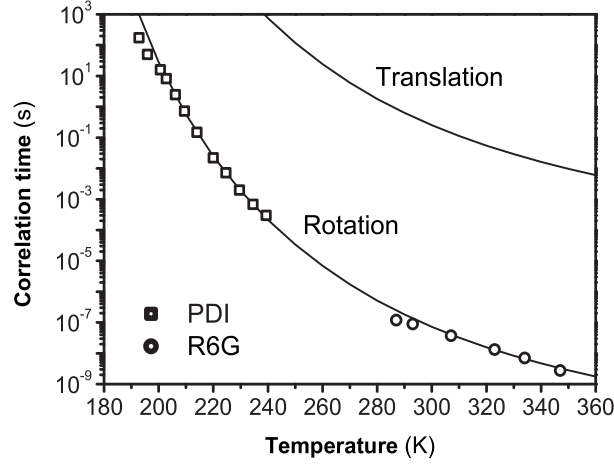


Figure 7.1: Solid lines: Calculated temperature dependence of the rotation (bottom curve) and translation (top curve) correlation times for rhodamine 610 in glycerol, based on viscosity data from reference [136]. For translational diffusion, the spot size a (Equation (7.7)) is chosen equal to $1\ \mu\text{m}$. The rotation curve is compared to experimental results obtained in this work. The circles stem from steady-state fluorescence anisotropy measurements on R6G in glycerol. The squares represent FACS measurements on PDI in glycerol which have been presented in Section 6.3.1. Both data sets are in good agreement with the model curve.

the signal from the parallel (to excitation) F_{\parallel} and that from the perpendicular detection channel F_{\perp} and is defined as follows:

$$r = \frac{F_{\parallel} - F_{\perp}}{F_{\parallel} + 2F_{\perp}} \quad (7.3)$$

The anisotropy decreases from its maximum value r_0 with decreasing rotation correlation time (and thereby with increasing temperature) according to Perrin's law [169]:

$$\frac{1}{r} = \frac{1}{r_0} \left(1 + \frac{\tau_F}{\tau_R} \right) = \frac{1}{r_0} \left(1 + \frac{k_B \tau_F T}{V \eta} \right) \quad (7.4)$$

with τ_F the fluorescence lifetime, 4×10^{-9} s for R6G [46]. In practice this decrease is only measurable at temperatures where the rotation time is not larger than about 100 times the fluorescence lifetime, i.e., at temperatures higher than 280 K for a small organic dye in glycerol (Figure 7.1). Steady-state fluorescence anisotropy of an ensemble is easy to measure within milliseconds. Scanning the confocal volume provides a temperature map with high spatial resolution in a reasonable time.

The rotation correlation time can also be determined by analyzing temporal fluctuations of the fluorescence anisotropy in a small volume by FACS [165–167]. This technique is fully described in Section 6.2.3. We present here only the expression for the resulting modified autocorrelation function of the fluorescence anisotropy $C'_r(t)$ from which we derive the rotation correlation time τ_R by adjusting a single exponential to it:

$$C'_r(t) = \frac{\langle r(t'+t)r(t') \rangle}{\langle r(t') \rangle^2} - 1 \propto \exp\left(-\frac{t}{\tau_R}\right) \quad (7.5)$$

We apply it here for an additional temperature calibration between 200 and 220 K. We expect FACS to provide for a more accurate temperature calibration, because the rotation curve depends very steeply on temperature in this region (Figure 7.1). Nevertheless, the time-averaging required to sample enough rotation events (at least 10 times the rotation correlation time) makes the method too slow for temperature imaging.

Fluorophores do not only rotate, they also diffuse spatially. Although we do not use translational diffusion as a temperature probe, it becomes important at high heating powers and may affect our results. The translational diffusion constant D [187]:

$$D = \frac{k_B T}{6\pi\eta R} \quad (7.6)$$

depends on R the hydrodynamic molecular radius, 0.464 nm for rhodamine 610 [189]. A characteristic diffusion time is fixed by the volume through which a molecule diffuses, i.e., the focal volume in FCS. For three-dimensional isotropic diffusion, the translation correlation time τ_T is approximately:

$$\tau_T = \frac{a^2}{6D} \quad (7.7)$$

with a the size of the spot through which the molecule diffuses. For a typical laser spot size, $a = 1 \mu\text{m}$, we obtain the “translation” (top) curve in Figure 7.1. It shows that below 240 K, translation may be neglected on the timescale of our experiments, several minutes.

7.4 Temperature calibration of the fluorescence anisotropy

Figure 7.2a shows the variations with temperature of the steady-state fluorescence anisotropy of 10^{-5} M R6G in glycerol. We will use this curve to

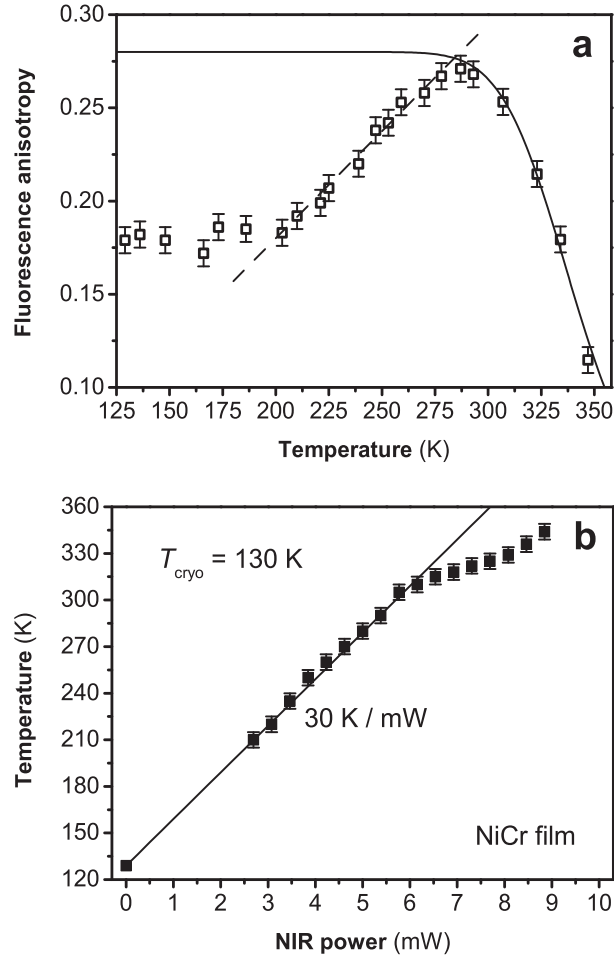


Figure 7.2: (a) Variations of the fluorescence anisotropy of R6G in glycerol with temperature. The anisotropy values have been averaged over a $20 \times 20 \mu\text{m}^2$ image (visible laser intensity 50 W/cm^2 , step size 200 nm , acquisition time 10 ms/point). The solid line is the expected dependence of the steady-state anisotropy due to rotational diffusion, see Equation (7.4). The dashed line guides the eye through a variation mainly due to photoblinking (see text). The error bars are 95% confidence intervals ($\pm 2\sigma = \pm 0.007$). (b) Actual temperature calibration with anisotropy in the center of the heating spot, as a function of heating power. The temperature first scales linearly with applied power with a slope of 30 K/mW (solid line). The deviation above 300 K is probably due to coupled matter and heat transport out of the heated spot when glycerol becomes very fluid. The accuracy of the calibration is $\pm 5 \text{ K}$, indicated by error bars.

determine the steady-state temperature in the center of the laser-heated spot. Each point is generated by taking the average anisotropy value of a complete $20 \times 20 \mu\text{m}^2$ image. To be completely consistent with images presented later, we use the same experimental conditions, excitation intensity (50 W/cm^2), scanning step (200 nm), and acquisition time (10 ms/point). Under our specific experimental conditions, the anisotropy signal is independent of temperature below 200 K. Between 200 and 280 K it increases from 0.18 to approximately 0.27, then rapidly decreases again to 0.11 at 345 K.

Between 200 and 280 K, glycerol is too viscous for significant reorientation of the dye during its fluorescence lifetime. We attribute the observed variation of the anisotropy to reversible photo-induced processes (photoblinking), causing the typical flickering of single-molecule signals. This is confirmed by behavior similar to that seen in Chapter 3 for R6G in poly(vinylalcohol), i.e., sub-linear dependence of fluorescence with excitation intensities, and recovery of the fluorescence signal in the dark after illumination. This recovery is accompanied by that of the anisotropy. As discussed in Chapter 3, saturation at intensities as low as 50 W/cm^2 cannot be due to inter-system crossing alone. Here, too, we attribute it to electron transfer from glycerol to the excited rhodamine, leading to the radical anion of R6G, a long-lived dark state. Being excitation-dependent, photoblinking influences fluorescence anisotropy. If a molecule's transition dipole lies along the laser field, it will be excited more often and will have a larger probability to convert to the dark state. The ratio of F_{\parallel} to F_{\perp} thus decreases, leading to a weaker apparent anisotropy. Thermally activated recovery from the dark state, as observed for R6G in poly(vinyl alcohol) in Chapter 3, reduces the discrepancy when the temperature increases from 200 to 280 K (dashed straight line in Figure 7.2 a). Below 200 K tunneling dominates activation (Chapter 3), and the apparent anisotropy becomes independent of temperature.

Above 280 K, the anisotropy closely follows Perrin's equation (7.4) as the rotation time quickly shortens and becomes comparable to the fluorescence lifetime. Due to the interplay of photoblinking and rotational diffusion, we cannot reliably measure the maximum fluorescence anisotropy r_0 of R6G in glycerol. Although the theoretical maximum r_0 of anisotropy in a rigid medium is 0.40, this value is only observed for purely electronic S_0-S_1 transitions, where the emission and absorption dipole moments are parallel. Vibronic components in emission and absorption may possess dipole moments with different orientations with respect to the molecular axes (e.g., parallel or perpendicular to the axis in the case of a molecule with C_2 symmetry). This effect, which is often represented by an average angle $\bar{\alpha}$ between excitation and emission moments,

leads to a reduced r_0 [169]:

$$r_0 = \frac{2}{5} \frac{\overline{3\cos^2\alpha} - 1}{2} \quad (7.8)$$

In the (ionic) rhodamine dyes, this effect yields a value of $\bar{\alpha}$ around 30° [189], and a value of 0.25 for r_0 . We have measured r_0 for R6G in the rigid polymer poly(vinyl-alcohol) [67, 70, 104] at room temperature (sample preparation described in Section 3.2). Our experimental conditions (confocal scan with step size $1\ \mu\text{m}$, acquisition time 10 ms/point, and excitation intensity $30\ \text{W}/\text{cm}^2$) were chosen such that photoblinking is negligible (Chapter 3). We find $r_0 = 0.28$, in good agreement with the above value from literature (0.25). We obtain the solid line in Figure 7.2 by inserting $r_0 = 0.28$ and the temperature dependence (Equation 7.1) of the viscosity η in Equation (7.4), and find an excellent agreement with experimental results from 280 to 350 K. The deduced rotation correlation times appear as the circles in Figure 7.1. The sudden disappearance of photoblinking effects at temperatures higher than 280 K can be ascribed to an even more efficient recovery process from the dark state, the diffusion and recombination of the geminate ions.

7.5 Imaging the laser-induced hot spot

We image the laser-induced hot spot with either total fluorescence ($F_{\parallel} + F_{\perp}$) or fluorescence anisotropy, Equation (7.3). We use the latter images to determine the temperature in the center of the hot spot as a function of heating power. The cryostat temperature is 130 K, the visible excitation intensity $50\ \text{W}/\text{cm}^2$, the image size $20 \times 20\ \mu\text{m}^2$, the step size 200 nm, and the acquisition time 10 ms/point. The NIR laser is applied continuously during each scan, and its power is varied from 0 up to 10 mW by steps of about 0.4 mW.

Figure 7.3 shows confocal images of the total fluorescence of $10^{-5}\ \text{M}$ R6G in glycerol with NIR laser powers of either 0, 5.0 or 8.5 mW applied at a fixed position. At 0 mW the image is uniformly bright, as expected for a fairly concentrated sample. The image recorded at 5 mW NIR power shows a bright spot at the heating location with a maximum intensity twice that at 130 K and a full width at half-maximum (fwhm) of approximately $4\ \mu\text{m}$. This fluorescence increase is caused by the activated recovery from the dark state (see previous subsection). At higher heating power, the hot spot turns darker and is surrounded by a bright ring. This ring is found to be persistent. It is formed when R6G molecules start to translationally diffuse over the time- and length-scales of the experiment. The strong temperature gradient around the heated

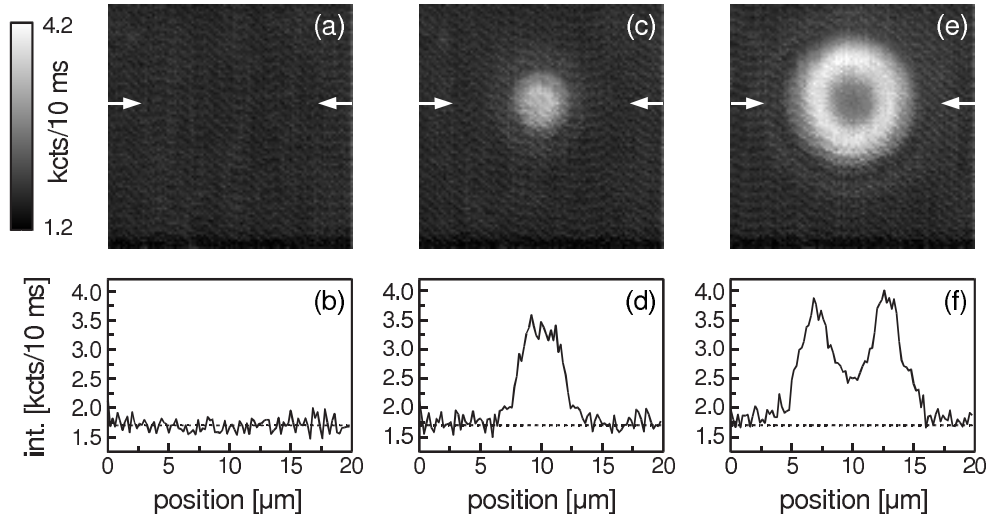


Figure 7.3: Intensity images: $20 \times 20 \mu\text{m}^2$ confocal fluorescence images of a glycerol film doped with R6G for NIR heating powers of 0 mW (a), 5 mW (c), or 8.5 mW (e). Graphs (b), (d) and (f) show the cross sections of images (a), (c) and (e) through the center of the heating spot. The total fluorescence images reveal the formation of a bright spot at first (c), then of a darker center surrounded by a bright and persistent ring (e).

spot induces a diffusion-time gradient (short time in the center, long at the surroundings), which traps the molecules at the colder edge and depopulates the center. The moment the heating abruptly ceases, the molecules are stuck, making the ring a permanent feature. A diffusion distance of $2 \mu\text{m}$ within a heating time of 50 s (half the scan time), allows us to estimate an average temperature of 270 K over the diffusion area (Figure 7.1). The maximum temperature in the center must be somewhat higher, but cannot be determined accurately in this way.

From the same data used for Figure 7.3, we calculate the steady-state fluorescence anisotropy images (Equation (7.3)) shown in Figure 7.4. At 0 mW, anisotropy is uniform. Heating first increases the anisotropy, again due to photoblinking. At still higher power, a high-anisotropy ring is formed, while the anisotropy in the center drops below its initial value. This image agrees with the temperature calibration of Figure 7.2a, with an initial increase between 200 and 280 K and a decrease above 280 K due to rotational diffusion. Note that this ring has a completely different origin from that of Figure 7.3 e, since the anisotropy is normalized to total intensity. Indeed, it disappears as soon as heating is switched off.

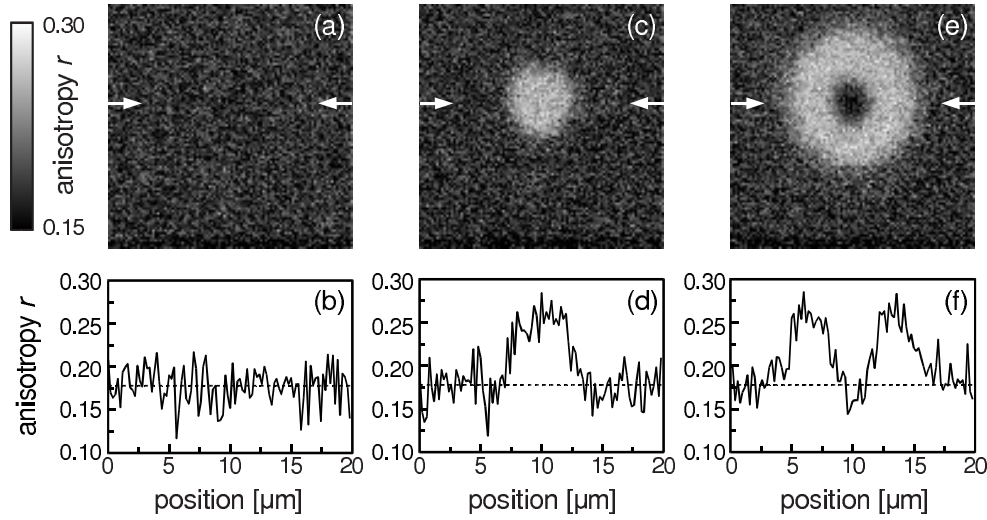


Figure 7.4: Anisotropy images: The data of Figure 7.3 provide $20 \times 20 \mu\text{m}^2$ images of fluorescence anisotropy. Graphs (b), (d) and (f) show cross-sections of images (a), (c) and (e) through the center of the heating spot. The images show first a high-anisotropy spot (c). Then, the anisotropy at the center decreases below the initial level, but is still above it in a (non-persistent) ring (e). The temperature calibration curve of Figure 7.2 yields the temperature in the center, 280 K for 5 mW (c) and 335 K for 8.5 mW (e).

The center temperature is calibrated from the fluorescence anisotropy as a function of NIR power in a series of images at varying NIR power. The corresponding temperatures follow from Figure 7.2 a, first from the dashed line (photoblinking) as long as the anisotropy increases, then from the solid curve (rotation) when it starts to decrease. The resulting local-temperature calibration is shown in Figure 7.2 b. The images in Figures 7.4 c and e yield two points in that calibration curve. The accuracy ($\pm 2\sigma$) of the points in Figure 7.2 b is approximately ± 5 K. The local temperature is found to vary linearly with the NIR power until 310 K. The slope is 30 K/mW for the NiCr film (Figure 7.2 b). Around 310 K the heating suddenly becomes less efficient. Since the thermal transport properties of glycerol and BK 7 glass do not significantly vary around this temperature [134, 135], we attribute the change to increased convective transport. We indeed have observed that the glycerol film breaks and irreversibly retracts from the heating location at a NIR heating power of around 10 mW (data not shown).

The fwhm of the feature at 5 mW NIR power (Figure 7.4 c) is approximately $5 \mu\text{m}$ and the temperature in the center 280 K. This corresponds to a maximum

temperature gradient of about 50 K/ μm . Accordingly, we expect the heating and cooling times to be in the microsecond domain. In Section 7.7, we directly probe the heating and cooling kinetics with time-resolved fluorescence intensity and anisotropy measurements.

7.6 Steady-state local temperature from FACS

At temperatures below 240 K, the rotational diffusion of fluorophores in glycerol becomes slow enough to allow rotation-time determination by anisotropy correlation, FACS. To reduce interference from photoblinking fluctuations, we replaced R6G by the more stable dye PDI for these measurements. The autocorrelation function $C_r'(t)$ (Equation (7.5)) of the fluorescence anisotropy is calculated from polarized intensity time-traces and fitted by a single-exponential, which gives the rotation correlation time directly.

Here, we use FACS measurements for an independent temperature calibration of the hot spot between 200 and 220 K, obtained from anisotropy time-traces of 100 s with 10 ms resolution. The cryostat temperature, 182 K, was chosen low enough to practically freeze out rotation on the experimental time scale in the absence of heating, as can be deduced from Figure 7.1. Upon heating with variable power (between 0 and 4 mW), reorientations give rise to fluctuations of the anisotropy signal, whose correlation yields the rotation correlation time and hence the temperature at the center of the hot spot, cf. Equations (7.5) and (7.2). Figure 7.5 a shows four autocorrelation functions with their single-exponential fits. Figure 7.5 b displays the resulting calibration curve of the temperature in the center of the hot spot as a function of NIR power. The relation is linear with a slope of 10.3 K/mW (the heating is less efficient here because the metal film is pure Cr instead of NiCr). In this limited temperature window (200 to 240 K), the steep temperature dependence of the rotation time considerably improves the temperature determination over fluorescence anisotropy (Figure 7.1). The accuracy ($\pm 2\sigma$) becomes ± 0.5 K instead of ± 5 K.

7.7 Kinetics of heating and cooling

Here, we investigate the heating and cooling kinetics of the hot spot using fluorescence intensity and anisotropy of R6G in glycerol. To achieve a satisfactory signal/noise ratio with a time resolution of 1 μs , we chop the NIR intensity with an AOM and average the heating and cooling transients of many bright and dark periods, with a Picoquant TimeHarp 200 photon-counting card. To

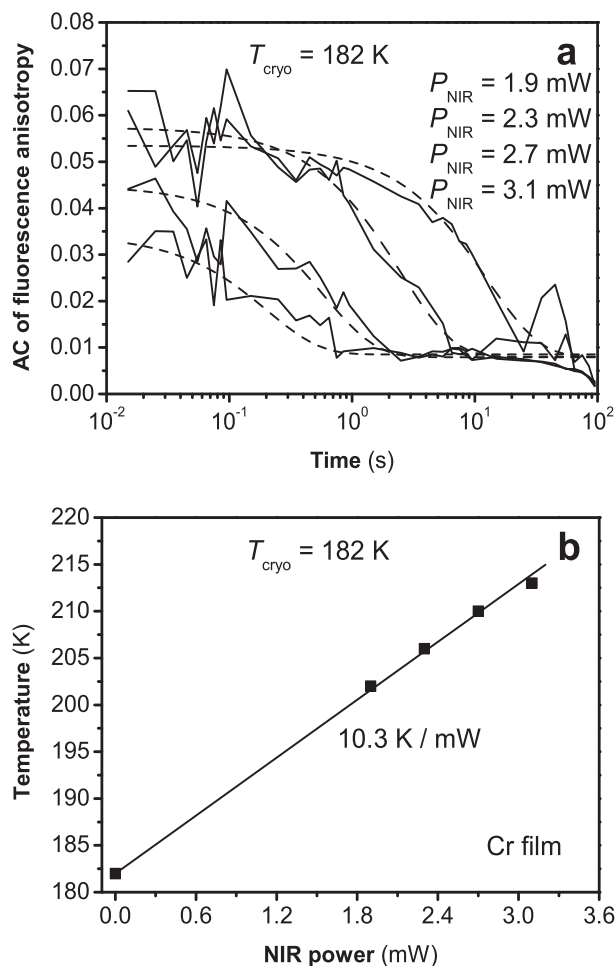


Figure 7.5: (a) Autocorrelation functions of the fluorescence anisotropy of PDI in glycerol at the center of the heating spot for NIR powers of 1.9, 2.3, 2.7, and 3.1 mW. The fluorescence anisotropy is recorded for 100 s with a time resolution of 10 ms. The dashed lines are fits to Equation (7.5) yielding rotation correlation times of 12.5, 2.5, 0.58, and 0.20 s. (b) Calibration of the temperature at the hot spot's center with heating power. The dependence is again linear (solid line) with a smaller slope, 10.3 K/mW, than in Figure 7.2 because of the weaker absorption of the chromium film. The typical inaccuracy ($\pm 2\sigma$) of the fits in (a) is about $\pm 20\%$, but the steep temperature dependence of the rotational diffusion (Figure 7.1) leads to a very precise determination of temperature with an accuracy of $\pm 0.5 \text{ K}$ (about the size of the symbols).

avoid spurious effects from long-term heating, we first determine the minimum cooling time required after each heating phase. Setting the cooling time to 100, 200, 500, or 1000 μs , with a constant heating time of 200 μs , and averaging the heating anisotropy transient for 100 ms at a NIR power of 11 mW, we find a constant anisotropy average of 0.14 for cooling times longer than 200 μs . We obtain a significantly lower value of 0.12 with the shorter cooling time of 100 μs . We therefore measure the kinetics with a square modulation of the NIR power at 2.5 kHz (200 μs heating followed by 200 μs cooling). The visible intensity is 50 W/cm², the NIR power is either 5.4, 7.0, or 11 mW, and the total observation time 600 s (1.5×10^6 periods).

Figure 7.6 a shows the time-resolved total fluorescence (parallel and perpendicular channels added) in the center of the NIR focus for R6G in glycerol, during heating (first 200 μs with NIR power high) and cooling (second 200 μs with no NIR power). The total intensity gradually increases upon heating and reaches a higher final value for elevated NIR powers. Upon cooling, the intensity reverts to its initial value at a rate much higher than for heating. This pronounced asymmetry stems from the highly nonlinear dependence of fluorescence on temperature, complicated by the slow time-response of photobleaching to temperature changes. This also manifests itself in the non-linear dependence of fluorescence on heating power (compare the initial signal at 130 K with its maxima for 5.4, 7.0 and 11 mW).

The fluorescence anisotropy is expected to be less sensitive to photobleaching than the total intensity. Figure 7.6 b shows anisotropy calculated from the same data. The initial anisotropy value, 0.132, is distinctly lower than 0.178, observed in the imaging experiments at 130 K (Figures 7.2 a and 7.4 b). This is probably a consequence of photo-induced processes (we remain for 600 s at the same sample position instead of 10 ms as in the imaging experiments). For 5.4 mW NIR power, the anisotropy variation due to heating is barely detectable. For the two higher heating powers, the variation appears clearly, but with an extreme asymmetry between apparent heating and cooling kinetics. This asymmetry obviously follows from the steady-state temperature variations of anisotropy (see Figure 7.2 a). Upon heating, the initial anisotropy increase, due to photobleaching, is suppressed since the bleaching kinetics are too slow to follow heating on a microsecond timescale (Chapter 3). The drop in anisotropy due to molecular rotation at temperatures higher than 280 K, on the contrary, is very fast. Therefore, our fast anisotropy-based thermometer only works above 280 K, i.e., for high enough heating powers, and then only at the end of the heating period and at the beginning of the cooling period.

To convert the anisotropy plots into temperature traces, we can neglect pho-

toblinking and only consider the effect of rotational diffusion described by Perrin's equation (7.4), see solid curve in Figure 7.2 a. Figure 7.7 shows the temperature responses during heating and cooling for 7.0 and 11 mW, calculated from the data of Figure 7.6 b. Below 280 K, the temperature cannot be determined and the plots are very noisy. Between 280 and 300 K the accuracy is low because of the large uncertainty in r_0 . Above 300 K the accuracy in the temperature determination is $\pm 2\sigma = \pm 3$ K.

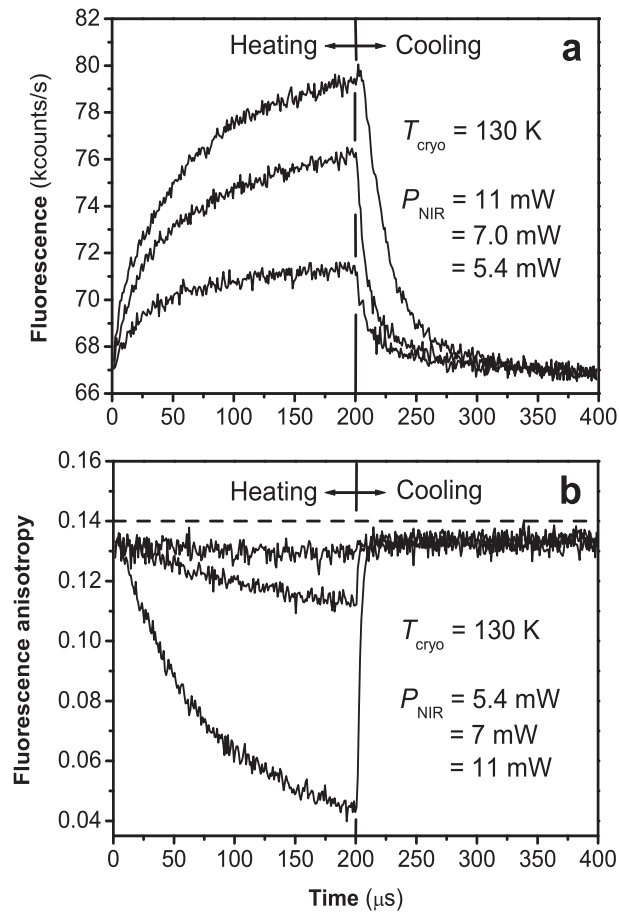


Figure 7.6: (a) Total fluorescence intensity response for R6G in glycerol at the center of the hot spot during heating (first 200 μs) and subsequent cooling (second 200 μs) at NIR powers of 5.4, 7.0, and 11 mW. The time resolution is 1 μs . (b) Corresponding time-dependence of the anisotropy, calculated from the same data.

For discussion purposes, we characterize the heating and cooling kinetics by the time $t_{1/2}$ needed to reach half of the final temperature difference. In order to fit the experimental temperature traces of Figure 7.7, we solve the heat equation [190] in an approximate way with a micrometer-sized point source heating the semi-infinite glass substrate (the heat diffusivity of glycerol is about 5 times lower than that of glass [135]) at a constant power during

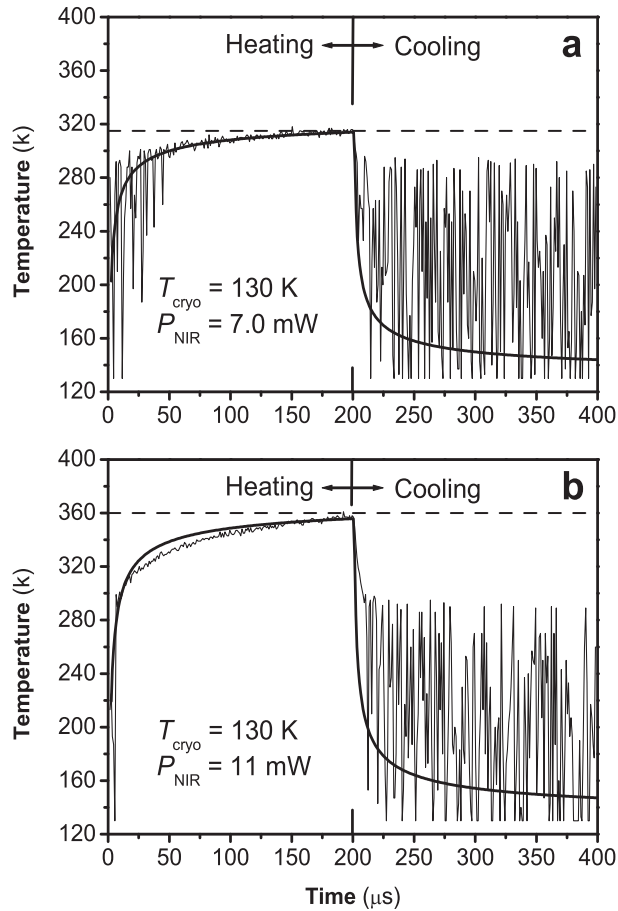


Figure 7.7: Temperature response during heating (first 200 μs) and cooling (second 200 μs) for NIR heating powers of 7.0 mW (a), and 11 mW (b). The plots are derived from the anisotropy traces in Figure 7.6 b. The time resolution is 1 μs . The smooth lines are simulations of the temperature response according to the heat equation, cf. Equations (7.9) and (7.12). The fit of the data in (a) is nearly perfect, yielding a $t_{1/2}$ of about 3.5 μs . The deviation of the simulation in (b) is assigned to the different regime of heat transport in fluid glycerol above 310 K.

$\tau_1 = 200 \mu\text{s}$, and turned off during the rest of the period (second $200 \mu\text{s}$). The solution during the heating period is:

$$T(t) = T_{\text{cryo}} + A \left(\frac{1}{\sqrt{\tau_0}} - \frac{1}{\sqrt{t}} \right) \quad (7.9)$$

with $T_{\text{cryo}} = 130 \text{ K}$ and

$$\tau_0 = \frac{a^2}{6\kappa} \quad (7.10)$$

a is the radius of the initial heating spot and κ the thermal diffusivity of the heated medium (glass).

$$A = \frac{P}{2c(\pi\kappa)^{3/2}} \quad (7.11)$$

with P the heating power and c the volume-specific heat of the hot spot. The solution during the cooling periods ($t > \tau_1$) is:

$$T(t) = T_{\text{cryo}} + A \left(\frac{1}{\sqrt{(t - \tau_1)}} - \frac{1}{\sqrt{t}} \right) \quad (7.12)$$

Excellent agreement to the curve at 7.0 mW (cf. Figure 7.7 a) is obtained with $\tau_0 = 1 \mu\text{s}$ and $A = 0.20 \text{ K s}^{1/2}$. The τ_0 value corresponds to a heating spot size of 3 to $4 \mu\text{m}$ which is in good agreement with what we have observed in the imaging experiments. The value of A is 75% of the value obtained when literature values [134] for glass are inserted for c and κ and the absorption coefficient of the metal film is 30% . With the same parameters, we calculate the expected profile for 11 mW heating power. As shown in Figure 7.7 b, there is a significant deviation from the experimental data. We attribute this to the change in transport properties of the glycerol film at temperatures higher than 300 K (see Figure 7.2b). From the theoretical curve at 7.0 mW , we can determine a $t_{1/2}$ value of $3.5 \mu\text{s}$.

In the previous paragraph, we have established that temperature changes of up to 200 K are possible in a few microseconds. Reaching the equilibrium temperature within a few K may still take $150 \mu\text{s}$. However, for an actual temperature-cycle experiment as proposed in Section 1.3, the time resolution is only limited by the time it takes to reach T_{quench} , the temperature where the process of interest is frozen. If the cryostat temperature T_{cryo} is chosen such that $T_{\text{quench}} = (T_{\text{cryo}} + T_{\text{high}})/2$, this quenching time is $t_{1/2}$, i.e., a few

microseconds. Let us illustrate this by the supercooling of water. The ice-formation rate is $3\text{ K}/\mu\text{s}$ for pure water but orders of magnitude less when cryoprotectants like glycerol or trehalose are added [191–193]. When liquid water is cooled at this rate well past its freezing point, supercooled water is obtained. Let us take $T_{\text{quench}} = 260\text{ K}$. Under our current experimental conditions, $T_{\text{cryo}} = 130\text{ K}$, it would take less than a microsecond to reach 260 K from room temperature (295 K). The average freezing rate is about $50\text{ K}/\mu\text{s}$, fast enough to supercool even pure water. The ability to supercool water is also of experimental interest, since it means that large biomolecules, like DNA and proteins, can be reversibly temperature-cycled. If the cooling were too slow, these molecules would be damaged by the expanding ice.

7.8 Conclusion

We have directly shown that local heating by a focussed laser generates a micrometer-sized hot spot with temperature changes of several hundreds of K in a few microseconds. We have imaged the hot spot through the polarized fluorescence of a dye. This method has enabled us to calibrate the temperature between 200 and 350 K with an accuracy ($\pm 2\sigma$) of $\pm 5\text{ K}$. In this broad temperature range, various temperature-dependent processes can be used, e.g. reversible photo-induced processes (photoblinking), or rotational diffusion. In the limited temperature range 200–220 K, we could calibrate the temperature more accurately ($\pm 0.5\text{ K}$) by analyzing rotational diffusion through fluorescence anisotropy correlation spectroscopy (FACS). Owing to the fast response of rotational diffusion above 280 K, we have measured the high-temperature parts of the heating and cooling responses in real time. The heating and cooling are characterized by a half time of about $4\mu\text{s}$. These results show the feasibility of temperature jumps of up to 200 K in about one microsecond.

The next step of the present work will be to apply temperature cycles to study the dynamics of single molecules at room temperature. The dynamical process of interest will be decomposed into a series of freeze-measure-thaw-evolution cycles, where the duration of the steps will be varied (cf. Section 1.3). Our method has three potential advantages over room-temperature single-molecule experiments : i) It will yield a longer observation time of each single molecule, because the optical probing is performed at low temperature where photobleaching is considerably reduced (Chapter 4); ii) Its time resolution does not depend on the fluorescence rate but is limited to the heating and cooling times. This will result in a time resolution of microseconds in the best cases. In a conventional single-molecule experiment, such a time resolution

would require very high excitation intensities, which would dramatically reduce the observation time; iii) The local (high) temperature can be adjusted quickly. This will significantly speed up mechanistic analysis, during which the temperature is varied to monitor the activation energies of different reaction pathways. The temperature-cycle experiment seems particularly promising for the single-molecule analysis of protein folding, a process extending over many timescales [20], and to follow repeated folding events of one and the same single protein.

Acknowledgements

The author wishes to thank E. van der Togt and J. Berkhout for their contributions to the experiments and Dr. M. Lippitz for the development of the data acquisition software and his continuing support. He acknowledges the preparation of the initial metal films in his institute by M. B. S. Hesselberth in the group of Prof. J. Aarts.

8 Thermal manipulation of single-molecule dynamics

abstract - We show and discuss examples of thermal triggering of rotational diffusion in supercooled glycerol. We provide a perspective for the application of temperature-cycle microscopy to the study of single-protein dynamics.

8.1 Triggering of single-molecule rotational diffusion by temperature jumps

Here, we have used local heating to manipulate rotational diffusion of single fluorophores in glycerol. The samples were 10^{-9} M rhodamine 6G (R6G) in glycerol and 10^{-9} M perylenedicarboximide (PDI) in glycerol. The structures of the fluorophores are shown in Figures 3.1 and 6.1, respectively. The samples were prepared as described in Section 6.2.1, the sole difference being that we spincoated the samples onto a metal-coated substrate. The metal film provided for local heating by efficient absorption of a NIR laser as discussed in Section 2.1.1. We have performed the experiments on the temperature-cycle microscope which is presented in Chapter 2. The rotational diffusion of single fluorophores was characterized by measuring rotation correlation times through autocorrelation analysis. The procedure is described in detail in Section 6.2.4.

First, we have applied laser-induced local heating to switch the steady-state temperature around individual molecules in glycerol to manipulate their rotational diffusion. Figures 8.1 a to e show, as an example, time traces of the reduced linear dichroism of a single R6G molecule at a cryostat temperature of 130 K. From trace to trace, the near-infrared (NIR) heating power was alternated between 0 and 2.5 mW. Since we had prepared the glycerol film on a NiCr coated substrate, we expected the temperature to alternate between 130 and roughly 205 K (cf. Figure 7.2). Accordingly, the molecules should be immobile when no NIR power is applied, and rotate during the periods with 2.5 mW heating power. Figures 8.1 b and d reveal indeed bigger excursions of the linear dichroism than these observed when no NIR power is applied, see Figures 8.1 a, c and e. However, this particular molecule never seemed to sample all possible orientations and values of its linear dichroism. To quantify, we show the corresponding autocorrelation functions of the linear dichroism in Figure 8.1 f. The autocorrelation analysis revealed the absence of rotational diffusion when no NIR power is applied and rotational diffusion, albeit with a low contrast, when the molecule is exposed to 2.5 mW of heating power. The reduced contrast of the rotation autocorrelation and the limited excursions in the linear dichroism unambiguously show that the rotational diffusion of the single molecule was restricted. Comparison to Figures 6.3 or 7.1 indicates that the average rotation time should be 3.6 s at 205 K (the rotation time seems indifferent to whether R6G or PDI is used). Since we measured in Chapter 6 that the full-width at half-maximum of the rotation-time distributions is roughly 3 to 4 times the average, a single-molecule rotation time of 2.2 s is

8.1 Triggering of single-molecule rotational diffusion by temperature jumps

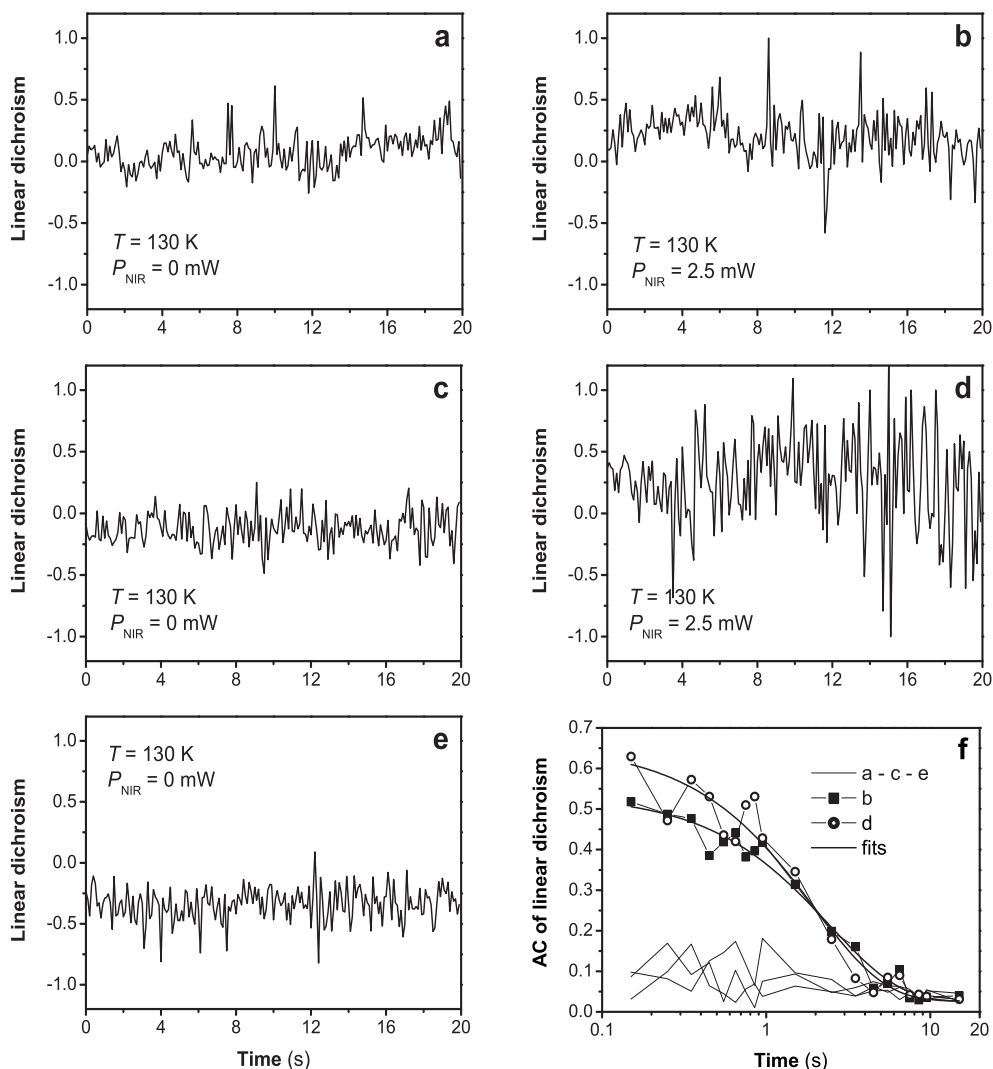


Figure 8.1: (a-e) Linear-dichroism time traces of a single R6G molecule in glycerol while alternately a NIR heating power of 0 (a,c,e) or 2.5 mW (b,d) is applied. The substrate is a NiCr coated glass plate. The time resolution is 100 ms/point, the visible (514.5 nm) intensity 2.5 kW/cm^2 , and the cryostat temperature is 130 K. The traces recorded during exposure to the NIR laser (b,d) clearly show larger excursions of the reduced linear dichroism than when no NIR power is applied (a,c,e). f) Autocorrelation functions of the five linear-dichroism time traces shown in a to e. When no NIR power is applied, no rotation is observed. At a NIR power of 2.5 mW, molecular rotation, albeit restricted, is observed with a characteristic time of about 2.2 s.

well within the reasonable range.

We have repeated this experiment on many individual molecules, but only occasionally did we observe rotational diffusion upon heating. When present, the number of reorientations were limited (compare Figures 8.1 d and 8.2 a).

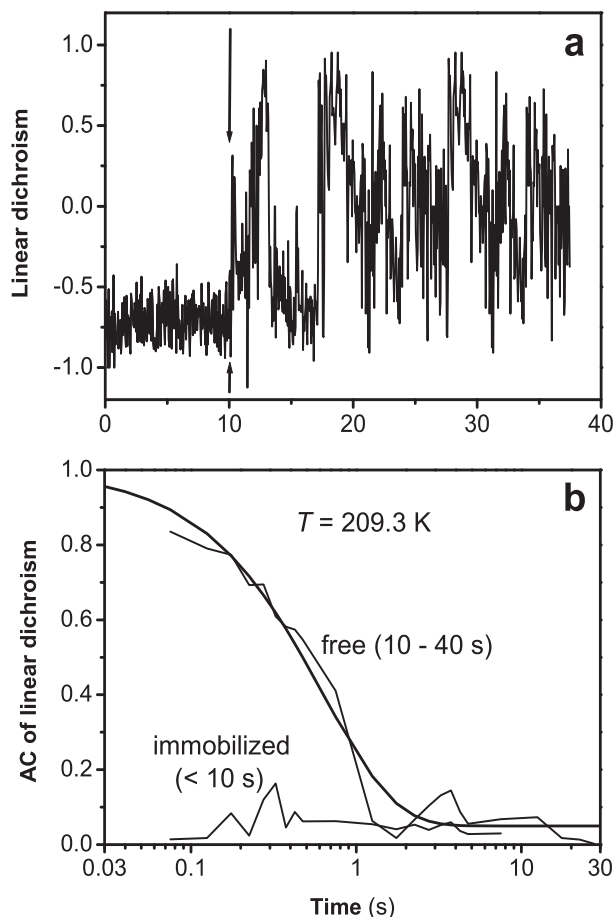


Figure 8.2: Heat-induced reactivation of a single PDI molecule in a 50 nm glycerol film on a Cr/silica coated substrate: (a) Time trace of the reduced linear dichroism of an initially immobilized PDI molecule. At $t = 10$ s, a 10 μ s, 350 nJ NIR “pulse” is given (indicated by the two arrows), after which the linear dichroism makes full excursions. The time resolution is 50 ms and the excitation intensity 500 W/cm². (b) Autocorrelation functions of the time trace in (a) before and after the heat pulse revealing no autocorrelation beforehand and a typical autocorrelation function for a freely rotating molecule afterwards. The latter autocorrelation function is accompanied by a single-exponential fit (solid line) giving $\tau_R = 630$ ms.

We attributed these problems to the tendency of the molecules to stick to the exposed metal film. Since this problem had not been observed in the samples of Chapter 6, we changed to the Cr substrates coated with an additional silica layer to isolate the fluorophores from the metal. Furthermore, we substituted R6G with PDI, because it is a more stable fluorophore and we expected it to be less attracted to the polar (oxidized in the UV-ozone cleaner, cf. Section 6.2.1) glass substrate. However, only in thick glycerol samples (1 to 3 μm as used in Chapter 6) did we always find rotating molecules. When the films were made thinner (approximately 50 nm) by adding water to the glycerol solution before spincoating, even the PDI molecules were found immobilized. However, the thick samples presented a high background, which was not a problem for autocorrelation analysis but far from a promising starting point for complicated temperature-cycle experiments.

Upon closer analysis of the 50 nm glycerol films, we found that when the sample was stored at room temperature under a dry atmosphere, the translational diffusion of the PDI molecules had the same characteristic time as that in a thick film, even when the film was kept for days (data not shown). However, after a cool-down to a typical temperature where single-molecule rotational diffusion in glycerol can be easily measured (205-210 K), we found that the majority of the fluorophores were immobilized and did not rotate. Initially, we supposed the immobilization to be the result of adsorption to the surface, from which came the idea to desorb individual molecules by a temperature jump. To explore this, we prepared thin glycerol films (roughly 50 nm) by spincoating a 10/90 glycerol/water solution containing 10^{-9} M PDI (with respect to glycerol) on a silica coated Cr covered glass substrate. After a cool-down to 210 K, we indeed found that most of the present fluorophores were immobilized. The next step was to try to reactivate the rotational diffusion of individual molecules by a 10 μs , 350 nJ NIR “pulse”. As before, we performed autocorrelation analysis of the reduced linear dichroism to determine whether a molecule was rotating.

Figure 8.2 shows an example of a heat-induced reactivation event of a single molecule. The top diagram (Figure 8.2 a) shows a time trace of the reduced linear dichroism of a single, initially immobilized PDI molecule, the rotational diffusion of which was reactivated by a temperature jump at $t = 10$ s. To confirm this reactivation, Figure 8.2 b shows the autocorrelation functions before and after the jump. The single-exponential fit of the autocorrelation function afterwards yields $\tau_{\text{R}} = 630$ ms, which is reasonable compared to the expected average rotation time of 730 ms at 209.3 K. However, in most cases we found the molecules to remain immobilized after the temperature jump, although some of them had changed their orientation. This is surprising because the

temperature jump brings the local environment of the molecule well above room temperature, so that when adsorption to the substrate is the cause of the immobilization, the majority of the fluorophores should be redissolved in the glycerol. Accordingly, we conclude that the immobilization (at least for PDI) is not the result of adsorption but related to the glass-forming properties of supercooled glycerol. In Chapter 6 we have argued that already at 210 K supra-molecular structures exist in supercooled glycerol. In this way, we may compare our thin glycerol film (50 nm) to a thin polymer film. For poly(methyl methacrylate) and polystyrene films of comparable thicknesses, the glass transition has been found to shift to either lower or higher temperatures [194–196]. A shift to higher temperature, as we observed here, can easily amount to 20 K and indicates a strong interaction with the substrate. In our case of glycerol on fused silica, this seems reasonable as we have fully oxidized the silica surface prior to spincoating. Consequently, for reactivation to occur, the heat pulse has to melt a significant part of the glassy film around the molecule under analysis, during which a large enough fluid domain has to be created to allow free rotation of the fluorophore afterwards. Obviously, this process has a low probability so that reactivation of rotational diffusion is only expected for a small fraction of the molecules, as was observed. To further investigate the mechanism of glass formation in thin glycerol films, comparable experiments should be performed at elevated temperatures.

We have shown as a proof-of-principle of our temperature-cycle method, the feasibility of thermal triggering of single-molecule rotational dynamics in glycerol. We have observed thermally induced single-molecule rotational diffusion and we have applied temperature jumps to reactivate the rotational diffusion of immobilized single molecules. Due to the poor quality of the thick glycerol films and the shifted glass-transition temperature in thin glycerol films, we have not been able to pursue the experiments in a more quantitative fashion.

8.2 Perspective for temperature-cycle analysis of single-protein dynamics

The dynamics of protein folding is a subject of great interest in biology. Proteins are able to fold into very complex structures in an environment containing a lot of similar molecules (the cytoplasm of the cell) and only by this folding process do they acquire their specific function [94]. One particular folding process may involve many substeps evolving on different timescales varying from picoseconds to hours [20]. To retrieve all details of such a complex and intrinsically heterogeneous process under equilibrium conditions, single-molecule

analysis is crucial, as was pointed out in Sections 1.1 and 1.2. Although an impressive amount of single-molecule optical work has been done on protein (un)folding and conformational dynamics [16, 197–209], most of our present knowledge still stems from ensemble experiments. An important flaw of the current single-molecule optical techniques is that they do not suffice in most cases to follow one and the same individual molecule during a complete folding event: The attached fluorophores are in general too unstable at room temperature to allow for an average observation time of at least a few minutes. Single-molecule methods that do not involve fluorescence, like atomic-force microscopy [210–214] and magnetic and optical traps [211, 213, 215], have also been applied to study protein (un)folding. However, these techniques have the disadvantage that they are much more intrusive to the system than fluorescence microscopy.

We have developed the temperature-cycle method with the intention to observe complete folding events of one and the same single protein molecule *in vitro*. The temperature-cycle concept has been presented in Section 1.3. The method is applicable to slow-folding proteins, because it facilitates longer observation times than the techniques restricted to room temperature. This is a consequence of the reduced photobleaching at the low (cryogenic) temperature (cf. Chapter 4) where the optical probing is performed. Temperature cycles may also help to study fast-folding proteins, because the time resolution is not limited by the amount of photons the label emits but by the characteristic time of the temperature cycles. In Chapter 7 we have shown that in this way a time resolution of microseconds is feasible. The uncoupling of time resolution and excitation intensity also allows experiments that combine a high time resolution and a long observation time, which are impossible with current single-molecule techniques. Finally, temperature-cycle microscopy presents the temperature as an additional and easily adjustable experimental parameter. In Section 1.2, we have argued that temperature variation of single-molecule dynamics is a powerful approach to disentangle energy landscapes as complex as those describing protein folding.

8.2.1 Polyproline – characterization of spFRET as a “spectroscopic ruler”

Since the size of a folded protein is on the order of 5 to 20 nm, the spatial resolution of fluorescence microscopy itself does not suffice to discern conformational changes related to protein folding. To achieve this nonetheless, single-molecule fluorescence microscopy is generally combined with Förster resonance energy transfer (FRET) into single-pair FRET (spFRET) [16, 199,

207, 216–218]. FRET is a non-radiative energy transfer between a donor and an acceptor fluorophore. Its efficiency depends on the spectral overlap between the emission spectrum of the donor and the absorption spectrum of the acceptor, their relative orientation, and their mutual distance r . The normalized FRET efficiency E for a given FRET pair is:

$$E = \frac{F_A}{F_A + F_D} = \frac{1}{1 + (r/R_0)^6} \quad (8.1)$$

with F_A and F_D the fluorescence intensity of the acceptor and the donor, respectively, and R_0 the characteristic Förster radius which is about 5 nm for most commonly used FRET pairs. Figure 8.3 illustrates how FRET can be applied to analyze conformational dynamics of (bio)molecules. The use of FRET as a quantitative ruler involves a number of corrections to Equation (8.1), among which are terms related to i) donor leakage, the amount of donor emission in the acceptor channel, ii) direct excitation of the acceptor by the excitation source (which is at resonance with the donor), and iii) the difference in photon-collection efficiency between the two detection channels [199, 217, 219, 220]. Further complications arise from photophysical and -chemical effects, a possible lack of orientational averaging, and spectral fluctuations. A classic problem of spFRET is that it does not distinguish between a donor-acceptor distance increase and blinking or bleaching of the acceptor since both give an apparent decrease of the FRET efficiency. Recently, a solution has been presented that involves alternating laser excitation (ALEX) of the donor and the acceptor, which allows continuous monitoring of acceptor activity [220, 221]. Specific problems in the spFRET analysis of protein folding are possible quenching of the chromophores by amino-acid residues, interactions with the protein backbone hampering orientational averaging of the fluorophores, and changes due to variation of the host (when for instance the concentration of the denaturant is changed) [207].

Consequently, the use of well-defined reference molecules is necessary to provide for quantitative spFRET distance measurements in the study of protein folding. In the literature, two kinds of reference molecules are presented, the polypeptide polyproline [16, 222, 223] and double-stranded DNA segments [217, 220, 221]. Although both structures are equally stiff, we will only consider polyproline, because we are interested in protein folding and the oligopeptide is (obviously) chemically much more similar to a protein than DNA. Oligomers of proline form a helical structure in aqueous solution which is considered to be the stiffest available polypeptide, because proline's pentagons form its backbone, see Figure 8.4. Recently, Schuler *et al.* [222] have

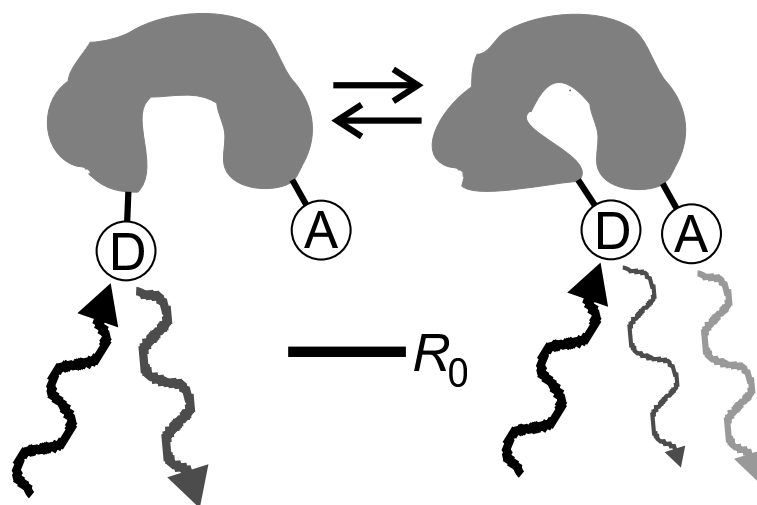


Figure 8.3: Schematic representation of the principle of FRET as a tool to study conformational changes on the nanometer scale. In the left state of the schematic (bio)molecule, the donor (D) and the acceptor (A) fluorophores are separated by almost twice the Förster radius (R_0 , typically 5 nm) so that the FRET efficiency is almost zero and the emission of the acceptor negligible. In the right form, the donor and acceptor are so close that significant quenching of the donor by the acceptor occurs. To obtain the steady-state populations and the relevant rate constants, spFRET analysis is required. This can be performed at two levels: i) the quasi-ensemble level where the FRET efficiencies of a number of single molecules are determined, from which a histogram is constructed giving the populations of the two states for a given set of conditions, or ii) the “pure” single-molecule level where histograms of the FRET efficiency are determined for each individual molecule separately by following its dynamics with time.

presented a detailed study of the spFRET efficiency of polyprolines as a function of their length. For this, they labelled the polyprolines with a donor (Alexa Fluor 488) at one end and an acceptor (Alexa Fluor 594) at the other end and varied the number of monomers from 6 to 40. They observed that polyproline is not as stiff as was commonly expected: It only behaves as a rigid rod up to a length of 12 monomers, while longer structures have to be considered as worm-like chains.

To perform spFRET measurements in our temperature-cycle microscope, we need to adapt the experimental configuration presented in Chapter 2. We will use 488 instead of 514.5 nm as the (visible) excitation wavelength, and exchange the polarization-dependent beamsplitter in the detection path by an appropriate dichroic mirror for the Alexa 488/594 FRET pair. Later on, we

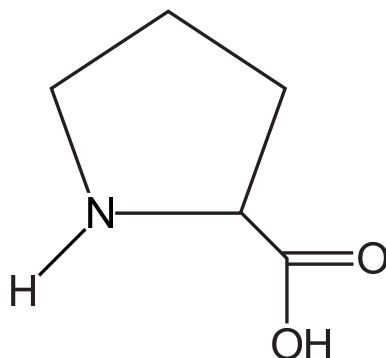


Figure 8.4: Structure of the amino acid proline.

may also implement a second excitation laser (probably a HeNe) to perform alternating excitation of the donor and the acceptor. We will measure the FRET efficiency of individual polyprolines of different lengths, which have been synthesized in the lab of B. Schuler. Initially, we intend to reproduce his results [222], by testing spFRET in our temperature-cycle microscope. Instead of an aqueous buffer solution, we will use thin glycerol films as hosts, which should also accommodate the polyprolines (B. Schuler, private communication). We will prepare 50 nm films by spincoating a solution of polyproline at the appropriate concentration in 10/90 glycerol/water. The characterization will also show to what extent the spread in relative orientations of the FRET pair affects the quality of our measurements. At room temperature, one generally supposes that all orientations are averaged within each time bin, but upon quenching at low temperature we will freeze out one particular orientation each time. This effect will induce an apparent broadening of the FRET histogram, for which we have to correct. Besides characterization, our temperature-cycle approach may also present a more detailed analysis of the conformational dynamics of the longer polyproline chains.

8.2.2 Cold-shock protein – an apparent two-state folder

Cold-shock proteins are small and robust proteins that almost exclusively exist of β -sheets. They fold very fast (≈ 1 ms) by an apparent two-state mechanism. Cold-shock proteins generally occur in bacteria where they are involved in the stabilization of important proteins, like polymerases, and found to be produced in great numbers upon sudden temperature drops (hence the name). Their robustness and simple dynamics have made cold-shock proteins and comparably small other proteins, like chymotrypsin inhibitor, the ideal guinea pigs to



Figure 8.5: Ribbon drawing of the cold-shock protein CspA from *Escherichia coli*. The figure reveals that the protein mainly consists of β sheets, which make it resistant to temperature changes. The shown structure is obtained by Schindelin *et al.* [224] using X-ray crystallography.

study protein folding and unfolding [16, 197, 199, 202, 207, 225, 226]. However, the two-state view is an approximation, since only specific conformations of the unfolded state may fold. This was not noticed for a long time, because the unfolded state rearranges itself on a timescale of microseconds which makes it difficult to analyze [227–229]. Figure 8.5 shows, as an example, the structure of cold-shock protein A (CspA) from the bacterium *Escherichia coli*.

Folding and unfolding of another cold-shock protein, that from the bacterium *Thermotoga maritima* (CspTm), has been extensively studied in spFRET experiments. In the initial study by the Eaton group [16], doubly labelled (Alexa Fluor 488 and 594) protein molecules were free to diffuse in an aqueous buffer solution. Each photon burst above a given threshold was attributed to a single protein molecule diffusing through the focus and its FRET efficiency was determined. In this way, the experimenters obtained steady-state distributions of folded and unfolded molecules at various concentrations of the denaturant, guanidinium chloride. At concentrations of up to 1 M they found predominantly the folded form, at around 1.5 M both forms, folded and unfolded, and finally above 2.5 M almost exclusively the unfolded form. The widths of the FRET histograms corresponding to the unfolded form were observed to be quite narrow, which confirmed that the unfolded protein rearranged on a sub-millisecond timescale, since the bin time of the experiment was 1 ms. In a

second experiment [202], the Eaton group investigated the kinetics of Csp *Tm* folding by driving proteins through a sudden gradient of decreasing denaturant concentration which they created at a well-defined position in space and time. They obtained FRET histograms at various positions in the gradient by varying the distance of the optical probing location to the starting point of the gradient. Although both the equilibrium and the kinetic experiments involved the measurement of the FRET efficiency of single molecules, they were still essentially ensemble experiments because they did not repeatedly probe the folding and unfolding of the same individual protein molecules (cf. Figure 8.3). Recently, Rhoades *et al.* [203] confined Csp *Tm* molecules in a fixed lipid vesicle [230] at a critical denaturant concentration of 2 M. In this way, they could observe repeated folding and unfolding of one and the same single molecule. However, they could not determine the characteristic time of the folding and unfolding steps, even at their highest achievable time resolution of 100 μ s. Furthermore, they were severely limited by photobleaching so that they could only observe a few events for each single molecule.

Temperature-cycle microscopy has the potential to present a more detailed view of the folding and unfolding of individual Csp *Tm* molecules. First of all, contrary to the previous methods, it has the time resolution (microseconds) to obtain the characteristic times of the folding and unfolding transitions and the dynamics of the unfolded form at the single-molecule level. Furthermore, it allows temperature variation by which we may slow down the actual folding and unfolding events and possibly observe short-lived intermediates or alternative folding schemes. Since we need to immobilize the proteins to prevent them from diffusing out of the hot spot (cf. Section 7.5), we will either use immobilized lipid vesicles [203, 230] or nanoporous silica gel [231]. Since the cold-shock proteins are very robust, we expect them to survive a normal (slow) cool-down of the cryostat to prepare the initial frozen state. However, when we wish to apply the temperature-cycle method to more fragile (and more interesting) proteins, such as enzymes, we expect denaturation to become a problem, as the cool-down of the cryostat is too slow to prevent ice formation. To obtain the required freezing rate of 3 K/ μ s [191], accommodation of the microspray technique inside the cryostat seems the best option [232]. This technique is currently applied to prepare samples for cryo-electron microscopy. It involves the spraying of microdroplets of a solution containing the molecules of interest at ambient temperature onto a cold surface. In this way, we may prepare a thin frozen film of proteins in lipid vesicles, once the cryostat is cold. The experimental realization of this rather ambitious construction has still to be worked out.

Bibliography

- [1] M. Orrit and J. Bernard, "Single pentacene molecules detected by fluorescence excitation in a *para*-terphenyl crystal", *Phys. Rev. Lett.*, **65** (1990) 2716–2719.
- [2] J. Bernard, L. Fleury, H. Talon and M. Orrit, "Photon bunching in the fluorescence from single molecules - a probe for intersystem crossing", *J. Chem. Phys.*, **98** (1993) 850–859.
- [3] X. S. Xie and R. C. Dunn, "Probing single-molecule dynamics", *Science*, **265** (1994) 361–364.
- [4] T. Basché, S. Kummer and C. Bräuchle, "Direct spectroscopic observation of quantum jumps of a single molecule", *Nature*, **373** (1995) 132–134.
- [5] T. Funatsu, Y. Harada, M. Tokunaga, K. Saito and T. Yanagida, "Imaging of single fluorescent molecules and individual ATP turnovers by single myosin molecules in aqueous-solution", *Nature*, **374** (1995) 555–559.
- [6] I. Sase, H. Miyata, J. E. T. Corrie, J. S. Craik and K. Kinoshita, "Real-time imaging of single fluorophores on moving Actin with an epifluorescence microscope", *Biophys. J.*, **69** (1995) 323–328.
- [7] T. Schmidt, G. J. Schütz, W. Baumgartner, H. J. Gruber and H. Schindler, "Characterization of photophysics and mobility of single molecules in a fluid lipid-membrane", *J. Phys. Chem.*, **99** (1995) 17662–17668.
- [8] T. Ha, T. Enderle, D. S. Chemla, P. R. Selvin and S. Weiss, "Single molecule dynamics studied by polarization modulation", *Phys. Rev. Lett.*, **77** (1996) 3979–3982.
- [9] R. M. Dickson, A. B. Cubitt, R. Y. Tsien and W. E. Moerner, "On/off blinking and switching behaviour of single molecules of Green Fluorescent Protein", *Nature*, **388** (1997) 355–358.
- [10] H. P. Lu, L. Y. Xun and X. S. Xie, "Single-molecule enzymatic dynamics", *Science*, **282** (1998) 1877–1882.
- [11] A. C. J. Brouwer, E. J. J. Groenen, M. C. van Hemert and J. Schmidt, "Isotope shifts and intersystem crossing for pentacene in *p*-terphenyl.

- a model system for single-molecule dynamics”, *J. Phys. Chem. A*, **103** (1999) 8959–8965.
- [12] C. E. Talley and R. C. Dunn, “Single molecules as probes of lipid membrane microenvironments”, *J. Phys. Chem. B*, **103** (1999) 10 214–10 220.
- [13] X. W. Zhuang, L. E. Bartley, H. P. Babcock, R. Russell, T. J. Ha, D. Herschlag and S. Chu, “A single-molecule study of RNA catalysis and folding”, *Science*, **288** (2000) 2048–2052.
- [14] L. A. Deschenes and D. A. Vanden Bout, “Single-molecule studies of heterogeneous dynamics in polymer melts near the glass transition”, *Science*, **292** (2001) 255–258.
- [15] K. D. Osborn, R. J. B. Urbauer, M. W. Allen and C. K. Johnson, “Single-molecule dynamics of target binding by calmodulin”, *Biophys. J.*, **82** (2002) 229.
- [16] B. Schuler, E. A. Lipman and W. A. Eaton, “Probing the free-energy surface for protein folding with single-molecule fluorescence spectroscopy”, *Nature*, **419** (2002) 743–747.
- [17] M. Dahan, S. Lévi, C. Luccardini, P. Rostaing, B. Riveau and A. Triller, “Diffusion dynamics of glycine receptors revealed by single-quantum dot tracking”, *Science*, **302** (2003) 442–445.
- [18] L. P. Watkins and H. Yang, “Single molecule dynamics of adenylate kinase”, *Biophys. J.*, **86** (2004) 180.
- [19] C. P. Schultz, “Illuminating folding intermediates”, *Nat. Struct. Biol.*, **7** (2000) 7–10.
- [20] K. A. Dill and H. S. Chan, “From Levinthal to pathways to funnels”, *Nat. Struct. Biol.*, **4** (1997) 10–19.
- [21] A. Dräbenstedt, “Hochauflösende Spektroskopie und Mikroskopie Einzelner Moleküle und Farbzentren Bei Tiefen Temperaturen”, Ph.D. thesis, Technical University of Chemnitz (1999), <http://www.tu-chemnitz.de/physik/ARCHIV/PROMOT/>.
- [22] C. M. Phillips, Y. Mizutani and R. M. Hochstrasser, “Ultrafast thermally-induced unfolding of RNase-A”, *Proc. Natl. Acad. Sci. U. S. A.*, **92** (1995) 7292–7296.
- [23] R. M. Ballew, J. Sabelko and M. Gruebele, “Direct observation of fast protein folding: the initial collapse of apomyoglobin”, *Proc. Natl. Acad. Sci. U. S. A.*, **93** (1996) 5759–5764.
- [24] V. Munoz, P. A. Thompson, J. Hofrichter and W. A. Eaton, “Folding dynamics and mechanism of β -hairpin formation”, *Nature*, **390** (1997) 196–199.

-
- [25] R. H. Callender, R. B. Dyer, R. Gilmanshin and W. H. Woodruff, "Fast events in protein folding: the time evolution of primary processes", *Annu. Rev. Phys. Chem.*, **49** (1998) 173–202.
- [26] M. Gruebele, "The fast protein folding problem", *Annu. Rev. Phys. Chem.*, **50** (1999) 485–516.
- [27] W. A. Eaton, V. Munoz, S. J. Hagen, G. S. Jas, L. J. Lapidus, E. R. Henry and J. Hofrichter, "Fast kinetics and mechanisms in protein folding", *Annu. Rev. Biophys. Biomol. Struct.*, **29** (2000) 327–359.
- [28] A. Ansari, S. V. Kuznetsov and Y. Q. Shen, "Configurational diffusion down a folding funnel describes the dynamics of DNA hairpins", *Proc. Natl. Acad. Sci. U. S. A.*, **98** (2001) 7771–7776.
- [29] C. R. Rabl, S. R. Martin, E. Neumann and P. M. Bayley, "Temperature jump kinetic study of the stability of apo-calmodulin", *Biophys. Chem.*, **101** (2002) 553–564.
- [30] G. Dimitriadis, A. Drysdale, J. K. Myers, P. Arora, S. E. Radford, T. G. Oas and D. A. Smith, "Microsecond folding dynamics of the F13W G29A mutant of the β domain of staphylococcal protein a by laser-induced temperature jump", *Proc. Natl. Acad. Sci. U. S. A.*, **101** (2004) 3809–3814.
- [31] H. S. Chung, M. Khalil, A. W. Smith, Z. Ganim and A. Tokmakoff, "Conformational changes during the nanosecond-to-millisecond unfolding of ubiquitin", *Proc. Natl. Acad. Sci. U. S. A.*, **102** (2005) 612–617.
- [32] A. Margineanu, J. Hofkens, M. Cotlet, S. Habuchi, A. Stefan, J. Q. Qu, C. Kohl, K. Müllen, J. Vercammen, Y. Engelborghs, T. Gensch and F. C. de Schryver, "Photophysics of a water-soluble rylene dye: comparison with other fluorescent molecules for biological applications", *J. Phys. Chem. B*, **108** (2004) 12 242–12 251.
- [33] J. Schuster, F. Cichos and C. von Borczyskowski, "Influence of self-trapped states on the fluorescence intermittency of single molecules", *Appl. Phys. Lett.*, **87** (2005) 051 915.
- [34] S. Masuo, T. Vosch, M. Cotlet, P. Tinnefeld, S. Habuchi, T. D. M. Bell, I. Oesterling, D. Beljonne, B. Champagne, K. Müllen, M. Sauer, J. Hofkens and F. C. de Schryver, "Multichromophoric dendrimers as single-photon sources: a single-molecule study", *J. Phys. Chem. B*, **108** (2004) 16 686–16 696.
- [35] M. Bates, T. R. Blosser and X. W. Zhuang, "Short-range spectroscopic ruler based on a single-molecule optical switch", *Phys. Rev. Lett.*, **94** (2005) 108 101.

- [36] J. P. Hoogenboom, E. M. H. P. van Dijk, J. Hernando, N. F. van Hulst and M. F. Garcia-Parajo, "Power-law-distributed dark states are the main pathway for photobleaching of single organic molecules", *Phys. Rev. Lett.*, **95** (2005) 097401.
- [37] W. Denk, D. W. Piston and W. W. Webb, "Two-Photon Molecular Excitation in Laser Scanning Microscopy", Plenum, New York (1995), pp. 445–458.
- [38] A. Schönle and S. W. Hell, "Heating by absorption in the focus of an objective lens", *Opt. Lett.*, **23** (1998) 325–327.
- [39] K. Svoboda and S. M. Block, "Biological applications of optical forces", *Annu. Rev. Biophys. Biomol. Struct.*, **23** (1994) 247–285.
- [40] Y. Liu, D. K. Cheng, G. J. Sonek, M. W. Berns, C. F. Chapman and B. J. Tromberg, "Evidence for localized cell heating induced by infrared optical tweezers", *Biophys. J.*, **68** (1995) 2137–2144.
- [41] E. J. G. Peterman, F. Gittes and C. F. Schmidt, "Laser-induced heating in optical traps", *Biophys. J.*, **84** (2003) 1308–1316.
- [42] M. Cathelinaud, F. Lemarquis and C. Amra, "Index determination of opaque and semitransparent metallic films: application to light absorbers", *Appl. Optics*, **41** (2002) 2546–2554.
- [43] H. van der Meer, J. A. J. M. Disselhorst, J. Köhler, A. C. J. Brouwer, E. J. J. Groenen and J. Schmidt, "An insert for single-molecule magnetic-resonance spectroscopy in an external magnetic field", *Rev. Sci. Instr.*, **66** (1995) 4853–4856.
- [44] A. Bloess, Y. Durand, M. Matsushita, H. van der Meer, G. J. Brakenhoff and J. Schmidt, "Optical far-field microscopy of single molecules with 3.4 nm lateral resolution", *J. Microsc.- Oxf.*, **205** (2002) 76–85.
- [45] W. E. Moerner, "Polymer luminescence - those blinking single molecules", *Science*, **277** (1997) 1059–1060.
- [46] D. N. Dempster, T. Morrow and M. F. Quinn, "The photochemical characteristics of rhodamine 6G-ethanol solutions", *J. Photochem.*, **2** (1973/74) 343–359.
- [47] V. E. Korobov and A. K. Chibisov, "Primary processes in the photochemistry of rhodamine dyes", *J. Photochem.*, **9** (1978) 411–424.
- [48] H. de Vries and D. A. Wiersma, "Fluorescence transient and optical free induction decay spectroscopy of pentacene in mixed crystals at 2 K. determination of intersystem crossing and internal conversion rates", *J. Chem. Phys.*, **70** (1978) 5807–5822.

-
- [49] R. Menzel and E. Thiel, “Intersystem crossing rate constants of rhodamine dyes: influence of the amino-group substitution”, *Chem. Phys. Lett.*, **291** (1998) 237–243.
- [50] T. Ha, T. Enderle, D. S. Chemla, P. R. Selvin and S. Weiss, “Quantum jumps of single molecules at room temperature”, *Chem. Phys. Lett.*, **271** (1997) 1–5.
- [51] K. D. Weston, P. J. Carson, H. Metiu and S. K. Buratto, “Room-temperature fluorescence characteristics of single dye molecules adsorbed on a glass surface”, *J. Chem. Phys.*, **109** (1998) 7474–7485.
- [52] W. T. Yip, D. H. Hu, J. Yu, D. A. V. Bout and P. F. Barbara, “Classifying the photophysical dynamics of single- and multiple- chromophoric molecules by single molecule spectroscopy”, *J. Phys. Chem. A*, **102** (1998) 7564–7575.
- [53] D. S. English, A. Furube and P. F. Barbara, “Single-molecule spectroscopy in oxygen-depleted polymer films”, *Chem. Phys. Lett.*, **324** (2000) 15–19.
- [54] H. P. Lu and X. S. Xie, “Single-molecule spectral fluctuations at room temperature”, *Nature*, **385** (1997) 143–146.
- [55] K. D. Weston, P. J. Carson, J. A. DeAro and S. K. Buratto, “Single-molecule detection fluorescence of surface-bound species in vacuum”, *Chem. Phys. Lett.*, **308** (1999) 58–64.
- [56] G. Messin, J. P. Hermier, E. Giacobino, P. Desbiolles and M. Dahan, “Bunching and antibunching in the fluorescence of semiconductor nanocrystals”, *Opt. Lett.*, **26** (2001) 1891–1893.
- [57] R. Verberk, A. M. van Oijen and M. Orrit, “Simple model for the power-law blinking of single semiconductor nanocrystals”, *Phys. Rev. B*, **66** (2002) 233 202.
- [58] T. Basché, S. Kummer and C. Bräuchle, “Optical spectroscopy of single pentacene molecules in an ordered and a disordered *p*-terphenyl crystal”, *Chem. Phys. Lett.*, **225** (1994) 116–123.
- [59] S. M. Nie, D. T. Chiu and R. N. Zare, “Probing individual molecules with confocal fluorescence microscopy”, *Science*, **266** (1994) 1018–1021.
- [60] J. A. Veerman, M. F. Garcia-Parajó, L. Kuipers and N. F. van Hulst, “Time-varying triplet state lifetimes of single molecules”, *Phys. Rev. Lett.*, **83** (1999) 2155–2158.
- [61] C. G. Hübner, A. Renn, I. Renge and U. P. Wild, “Direct observation of the triplet lifetime quenching of single dye molecules by molecular oxygen”, *J. Chem. Phys.*, **115** (2001) 9619–9622.

- [62] I. Renge, C. G. Hübner, A. Renn, H. Langhals and U. P. Wild, “Slow photochemical transformations of single dye molecules in polymer environment at room temperature”, *J. Lumines.*, **98** (2002) 91–96.
- [63] W. P. Ambrose, P. M. Goodwin, J. C. Martin and R. A. Keller, “Single-molecule detection and photochemistry on a surface using near-field optical excitation”, *Phys. Rev. Lett.*, **72** (1994) 160–163.
- [64] H. P. Lu and X. S. Xie, “Single-molecule kinetics of interfacial electron transfer”, *J. Phys. Chem. B*, **101** (1997) 2753–2757.
- [65] M. Sauer, K. H. Drexhage, U. Lieberwirth, R. Müller, S. Nord and C. Zander, “Dynamics of the electron transfer reaction between an oxazine dye and DNA oligonucleotides monitored on the single-molecule level”, *Chem. Phys. Lett.*, **284** (1998) 153–163.
- [66] J. Hofkens, M. Maus, T. Gensch, T. Vosch, M. Cotlet, F. Köhn, A. Herrmann, K. Müllen and F. C. de Schryver, “Probing photophysical processes in individual multichromophoric dendrimers by single-molecule spectroscopy”, *J. Am. Chem. Soc.*, **122** (2000) 9278–9288.
- [67] Y. W. Hou, A. M. Bardo, C. Martinez and D. A. Higgins, “Characterization of molecular scale environments in polymer films by single molecule spectroscopy”, *J. Phys. Chem. B*, **104** (2000) 212–219.
- [68] F. Köhn, J. Hofkens, R. Gronheid, M. van der Auweraer and F. C. de Schryver, “Parameters influencing the on- and off-times in the fluorescence intensity traces of single cyanine dye molecules”, *J. Phys. Chem. A*, **106** (2002) 4808–4814.
- [69] F. Vargas, O. Hollricher, O. Marti, G. de Schaetzen and G. Tarrach, “Influence of protective layers on the blinking of fluorescent single molecules observed by confocal microscopy and scanning near field optical microscopy”, *J. Chem. Phys.*, **117** (2002) 866–871.
- [70] Y. W. Hou and D. A. Higgins, “Single molecule studies of dynamics in polymer thin films and at surfaces: effect of ambient relative humidity”, *J. Phys. Chem. B*, **106** (2002) 10306–10315.
- [71] J. A. J. M. Disselhorst, H. van der Meer, O. G. Poluektov and J. Schmidt, “A pulsed EPR and ENDOR spectrometer operating at 95 Ghz”, *J. Magn. Reson. Ser. A*, **115** (1995) 183–188.
- [72] N. M. Atherton, “Principles of Electron Spin Resonance”, Ellis Horwood (PTR Prentice Hall): Chichester (1993).
- [73] C. R. Gochanour and M. D. Fayer, “Electronic excited-state transport in random systems. time-resolved fluorescence depolarization measurements”, *J. Phys. Chem.*, **85** (1981) 1989 – 1994.

- [74] S. Chandrasekhar, "Derivation of formula for the distance of randomly distributed particles in a large enough volume.", *Rev. Mod. Phys.*, **15** (1943) 1 – 89.
- [75] M. Talhavini and T. D. Z. Atvars, "Dye-polymer interactions controlling the kinetics of fluorescein photobleaching reactions in poly(vinyl alcohol)", *J. Photochem. Photobiol. A-Chem.*, **114** (1998) 65–73.
- [76] H. Talon, M. Orrit and J. Bernard, "Model for burning kinetics and shape of fluence-saturated spectral holes", *Chem. Phys.*, **140** (1990) 177–185.
- [77] A. A. Gorchelev, E. P. Snegirev, N. I. Ulitsky and B. M. Kharlamov, "Broadband hole burning: a new technique for the measurement of hole burning kinetics, removing the influence of inhomogeneous broadening", *Chem. Phys.*, **285** (2002) 289–297.
- [78] F. Stracke, M. Heupel and E. Thiel, "Singlet molecular oxygen photosensitized by rhodamine dyes: correlation with photophysical properties of the sensitizers", *J. Photochem. Photobiol. A-Chem.*, **126** (1999) 51–58.
- [79] M. W. Ferguson, P. C. Beaumont, S. E. Jones, S. Navaratnam and B. J. Parsons, "Excited state and free radical properties of rhodamine 123: a laser flash photolysis and radiolysis study", *Phys. Chem. Chem. Phys.*, **1** (1999) 261–268.
- [80] S. Navaratnam and B. J. Parsons, "Kinetic and spectral properties of rhodamine 6G free radicals: A pulse radiolysis study", *J. Photochem. Photobiol. A-Chem.*, **153** (2002) 153–162.
- [81] V. I. Krinichnyi, "2-mm waveband electron paramagnetic resonance spectroscopy of conducting polymers", *Synth. Met.*, **108** (2000) 173–222.
- [82] S. P. McGlynn, T. Azumi and M. Kinoshita, "Molecular Spectroscopy of the Triplet State", Prentice Hall, Inc.: Englewood Cliff, N. J. (1969).
- [83] J. Hernando, M. van der Schaaf, E. M. H. P. van Dijk, M. Sauer, M. F. Garcia-Parajó and N. F. van Hulst, "Excitonic behavior of rhodamine dimers: a single-molecule study", *J. Phys. Chem. A*, **107** (2003) 43–52.
- [84] R. M. Dickson, D. J. Norris, Y. L. Tzeng and W. E. Moerner, "Three-dimensional imaging of single molecules solvated in pores of poly(acrylamide) gels", *Science*, **274** (1996) 966–971.
- [85] S. Wennmalm, L. Edman and R. Rigler, "Conformational fluctuations in single DNA molecules", *Proc. Natl. Acad. Sci. U. S. A.*, **94** (1997) 10 641–10 646.
- [86] S. Weiss, "Fluorescence spectroscopy of single biomolecules", *Science*, **283** (1999) 1676–1683.

- [87] P. Schwille, U. Haupts, S. Maiti and W. W. Webb, “Molecular dynamics in living cells observed by fluorescence correlation spectroscopy with one- and two-photon excitation”, *Biophys. J.*, **77** (1999) 2251–2265.
- [88] X. S. Xie, “Single-molecule approach to dispersed kinetics and dynamic disorder: probing conformational fluctuation and enzymatic dynamics”, *J. Chem. Phys.*, **117** (2002) 11 024–11 032.
- [89] A. Yildiz, J. N. Forkey, S. A. McKinney, T. Ha, Y. E. Goldman and P. R. Selvin, “Myosin V walks hand-over-hand: single fluorophore imaging with 1.5-nm localization”, *Science*, **300** (2003) 2061–2065.
- [90] M. Bruchez, M. Moronne, P. Gin, S. Weiss and A. P. Alivisatos, “Semiconductor nanocrystals as fluorescent biological labels”, *Science*, **281** (1998) 2013–2016.
- [91] W. E. Moerner, “Single-molecule optical spectroscopy of autofluorescent proteins”, *J. Chem. Phys.*, **117** (2002) 10 925–10 937.
- [92] A. M. van Oijen, M. Ketelaars, J. Köhler, T. J. Aartsma and J. Schmidt, “Unraveling the electronic structure of individual photosynthetic pigment-protein complexes”, *Science*, **285** (1999) 400–402.
- [93] E. Mei, J. Y. Tang, J. M. Vanderkooi and R. M. Hochstrasser, “Motions of single molecules and proteins in trehalose glass”, *J. Am. Chem. Soc.*, **125** (2003) 2730–2735.
- [94] S. E. Radford, “Protein folding: progress made and promises ahead”, *Trends Biochem. Sci.*, **25** (2000) 611–618.
- [95] T. Ha and J. Xu, “Photodestruction intermediates probed by an adjacent reporter molecule”, *Phys. Rev. Lett.*, **90** (2003) 223 002.
- [96] T. Christ, F. Kulzer, P. Bordat and T. Basché, “Watching the photo-oxidation of a single aromatic hydrocarbon molecule”, *Angew. Chem.-Int. Edit.*, **40** (2001) 4192–4195.
- [97] M. A. Osborne, W. S. Furey, D. Klenerman and S. Balasubramanian, “Single molecule analysis of DNA immobilized on microspheres”, *Anal. Chem.*, **72** (2000) 3678–3681.
- [98] W. Göhde, U. C. Fischer, H. Fuchs, J. Tittel, T. Basché, C. Bräuchle, A. Herrmann and K. Müllen, “Fluorescence blinking and photobleaching of single terrylene diimide molecules studied with a confocal microscope”, *J. Phys. Chem. A*, **102** (1998) 9109–9116.
- [99] L. L. Song, E. J. Hennink, I. T. Young and H. J. Tanke, “Photobleaching kinetics of fluorescein in quantitative fluorescence microscopy”, *Biophys. J.*, **68** (1995) 2588–2600.

-
- [100] L. L. Song, C. A. G. O. Varma, J. W. Verhoeven and H. J. Tanke, "Influence of the triplet excited state on the photobleaching kinetics of fluorescein in microscopy", *Biophys. J.*, **70** (1996) 2959–2968.
- [101] L. L. Song, R. P. M. van Gijlswijk, I. T. Young and H. J. Tanke, "Influence of fluorochrome labeling density on the photobleaching kinetics of fluorescein in microscopy", *Cytometry*, **27** (1997) 213–223.
- [102] M. Talhavini and T. D. Z. Atvars, "Photostability of xanthene molecules trapped in poly(vinyl alcohol) (PVA) matrices", *J. Photochem. Photobiol. A-Chem.*, **120** (1999) 141–149.
- [103] M. Talhavini, W. Corradini and T. D. Z. Atvars, "The role of the triplet state on the photobleaching processes of xanthene dyes in a poly(vinyl alcohol) matrix", *J. Photochem. Photobiol. A-Chem.*, **139** (2001) 187–197.
- [104] D. Dibbern-Brunelli, M. G. Deoliveira and T. D. Z. Atvars, "Temperature-dependence of the photobleaching process of fluorescein in poly(vinyl alcohol)", *J. Photochem. Photobiol. A-Chem.*, **85** (1995) 285–289.
- [105] C. Eggeling, J. Widengren, R. Rigler and C. A. M. Seidel, "Photobleaching of fluorescent dyes under conditions used for single-molecule detection: evidence of two-step photolysis", *Anal. Chem.*, **70** (1998) 2651–2659.
- [106] C. Eggeling, J. Widengren, R. Rigler and C. A. M. Seidel, "Applied Fluorescence in Chemistry, Biology and Medicine", Springer-Verlag, Berlin Heidelberg (1998).
- [107] G. Somasundaram and A. Ramalingam, "Gain studies of rhodamine 6G dye doped polymer laser", *J. Photochem. Photobiol. A-Chem.*, **125** (1999) 93–98.
- [108] P. S. Dittrich and P. Schwille, "Photobleaching and stabilization of fluorophores used for single-molecule analysis with one- and two-photon excitation", *Appl. Phys. B-Lasers Opt.*, **73** (2001) 829–837.
- [109] G. Chirico, F. Cannone, G. Baldini and A. Diaspro, "Two-photon thermal bleaching of single fluorescent molecules", *Biophys. J.*, **84** (2003) 588–598.
- [110] M. A. van Dijk, L. C. Kapitein, J. van Mameren, C. F. Schmidt and E. J. G. Peterman, "Combining optical trapping and single-molecule fluorescence spectroscopy: enhanced photobleaching of fluorophores", *J. Phys. Chem. B*, **108** (2004) 6479–6484.

- [111] L. Fleury, J. M. Segura, G. Zumofen, B. Hecht and U. P. Wild, “Non-classical photon statistics in single-molecule fluorescence at room temperature”, *Phys. Rev. Lett.*, **84** (2000) 1148–1151.
- [112] A. M. van Oijen, J. Köhler, J. Schmidt, M. Müller and G. J. Brakenhoff, “Far-field fluorescence microscopy beyond the diffraction limit”, *J. Opt. Soc. Am. A-Opt. Image Sci. Vis.*, **16** (1999) 909–915.
- [113] M. D. Barnes, W. B. Whitten and J. M. Ramsey, “Detecting single molecules in liquids”, *Anal. Chem.*, **67** (1995) A418–A423.
- [114] S. Astilean, A. Corval, R. Casalegno and H. P. Trommsdorff, “Relaxation and photochemistry in pentacene doped benzoic acid crystals”, *J. Lumines.*, **58** (1994) 275–277.
- [115] C. V. Raman and K. R. Krishnan, “A new type of secondary radiation”, *Nature*, **121** (1928) 501–502.
- [116] C. V. Raman, “A change of wavelength in light scattering”, *Nature*, **121** (1928) 619.
- [117] C. V. Raman and K. R. Krishnan, “The optical analogue of the Compton effect”, *Nature*, **121** (1928) 711.
- [118] V. Aleksa, P. Klaeboe, C. J. Nielsen, V. Tanevska and G. A. Guirgis, “The conformations of bromomethyl dimethyl silane and bromomethyl dimethyl silane-d(1) as studied by vibrational spectroscopy and by ab initio calculations”, *Vib. Spectrosc.*, **17** (1998) 1–30.
- [119] A. Barabash, T. Gavrilko, K. Eshimov, G. Puchkovskaya and A. Shanchuk, “Vibrational spectra and lattice dynamics of hydrogen-bonded NH_4IO_3 crystal in the pretransition region”, *J. Mol. Struct.*, **512** (1999) 145–152.
- [120] K. R. Krishnan, “Influence of the temperature on the Raman effect”, *Nature*, **122** (1928) 650.
- [121] S. D. Rassat and E. J. Davis, “Temperature-measurement of single levitated microparticles using Stokes anti-Stokes-Raman intensity ratios”, *Appl. Spectrosc.*, **48** (1994) 1498–1505.
- [122] J. A. Wehrmeyer, S. Yeralan and K. S. Tecu, “Linewise Raman-Stokes anti-Stokes temperature measurements in flames using an unintensified charge-coupled device”, *Appl. Phys. B-Lasers Opt.*, **62** (1996) 21–27.
- [123] V. A. Karachevtseva, A. Y. Glamazda, U. Dettlaff-Weglikowska, V. S. Kurnosov, E. D. Obratsova, A. V. Peschanskii, V. V. Eremenko and S. Roth, “Raman spectroscopy of HiPCO single-walled carbon nanotubes at 300 and 5 K”, *Carbon*, **41** (2003) 1567–1574.

-
- [124] J. F. Lübben and B. Schrader, “Chemical composition analysis and temperature determination of optically levitated single aerosol particles by means of a compact Raman spectrometer”, *J. Mol. Struct.*, **410** (1997) 543–546.
- [125] S. Fujii and M. Gomi, “Fast temperature determination by nitrogen coherent anti-Stokes Raman-spectroscopy”, *AIAA J.*, **26** (1988) 311–315.
- [126] C. H. Chio, S. K. Sharma, P. G. Lucey and D. W. Muenow, “Effects of particle size and laser-induced heating on the Raman spectra of alpha quartz grains”, *Appl. Spectrosc.*, **57** (2003) 774–783.
- [127] D. I. Fotiadis, M. Boekholt, K. F. Jensen and W. Richter, “Flow and heat-transfer in CVD reactors - comparison of Raman temperature-measurements and finite-element model predictions”, *J. Cryst. Growth*, **100** (1990) 577–599.
- [128] R. Vehring and G. Schweiger, “Optical determination of the temperature of transparent microparticles”, *Appl. Spectrosc.*, **46** (1992) 25–27.
- [129] D. M. Haaland, K. L. Higgins and D. R. Tallant, “Multivariate calibration of carbon Raman-spectra for quantitative-determination of peak temperature history”, *Vib. Spectrosc.*, **1** (1990) 35–40.
- [130] B. Wangmanerat, T. M. Niemczyk and D. M. Haaland, “Determination of temperature and composition of phosphosilicate glass thin-films from infrared-emission spectral data”, *Appl. Spectrosc.*, **46** (1992) 1447–1453.
- [131] R. D. Andrews and T. J. Hammack, “Theoretical interpretation of dynamic mechanical loss spectra and transition temperatures”, *J. Polym. Sci. B*, **3** (1965) 655–657.
- [132] J. B. Segur and H. E. Oberstar, “Viscosity of glycerol and its aqueous solutions”, *Ind. Eng. Chem.*, **43** (1951) 2117–2120.
- [133] P. N. Shankar and M. Kumar, “Experimental determination of the kinematic viscosity of glycerol water mixtures”, *Proc. R. Soc. London Ser. A-Math. Phys. Eng. Sci.*, **444** (1994) 573–581.
- [134] R. C. Weast (ed.), “Handbook of Chemistry and Physics”, CRC Press, Cleveland, USA, 49th edn. (1968).
- [135] O. Sandberg, P. Andersson and G. Backstrom, “Heat-capacity and thermal-conductivity from pulsed wire probe measurements under pressure”, *J. Phys. E - Sci. Instrum.*, **10** (1977) 474–477.
- [136] K. Schröter and E. Donth, “Viscosity and shear response at the dynamic glass transition of glycerol”, *J. Chem. Phys.*, **113** (2000) 9101–9108.

- [137] I. V. Blazhnov, N. P. Malomuzh and S. V. Lishchuk, “Temperature dependence of density, thermal expansion coefficient and shear viscosity of supercooled glycerol as a reflection of its structure”, *J. Chem. Phys.*, **121** (2004) 6435–6441.
- [138] K. Schröter and E. Donth, “Comparison of shear response with other properties at the dynamic glass transition of different glass formers”, *J. Non-Cryst. Solids*, **307** (2002) 270–280.
- [139] G. Adam and J. H. Gibbs, “On the temperature dependence of cooperative relaxation properties in glass-forming liquids”, *J. Chem. Phys.*, **43** (1965) 139–146.
- [140] M. T. Cicerone and M. D. Ediger, “Photobleaching technique for measuring ultraslow reorientation near and below the glass-transition - tetracene in *o*-terphenyl”, *J. Phys. Chem.*, **97** (1993) 10 489–10 497.
- [141] M. T. Cicerone and M. D. Ediger, “Enhanced translation of probe molecules in supercooled *o*-terphenyl: Signature of spatially heterogeneous dynamics?”, *J. Chem. Phys.*, **104** (1996) 7210–7218.
- [142] R. Böhmer, G. Hinze, G. Diezemann, B. Geil and H. Sillescu, “Dynamic heterogeneity in supercooled *ortho*-terphenyl studied by multidimensional deuteron NMR”, *Europhys. Lett.*, **36** (1996) 55–60.
- [143] G. Hinze, “Geometry and time scale of the rotational dynamics in supercooled toluene”, *Phys. Rev. E*, **57** (1998) 2010–2018.
- [144] C. Y. Wang and M. D. Ediger, “How long do regions of different dynamics persist in supercooled *o*-terphenyl?”, *J. Phys. Chem. B*, **103** (1999) 4177–4184.
- [145] L. A. Deschenes and D. A. Vanden Bout, “Heterogeneous dynamics and domains in supercooled *o*-terphenyl: a single molecule study”, *J. Phys. Chem. B*, **106** (2002) 11 438–11 445.
- [146] A. Heuer, M. Wilhelm, H. Zimmermann and H. W. Spiess, “Rate memory of structural relaxation in glasses and its detection by multidimensional NMR”, *Phys. Rev. Lett.*, **75** (1995) 2851–2854.
- [147] S. C. Kuebler, A. Heuer and H. W. Spiess, “Glass transition of polymers: Memory effects in structural relaxation of polystyrene”, *Phys. Rev. E*, **56** (1997) 741–749.
- [148] C. Y. Wang and M. D. Ediger, “Lifetime of spatially heterogeneous dynamic domains in polystyrene melts”, *J. Chem. Phys.*, **112** (2000) 6933–6937.
- [149] E. V. Russell and N. E. Israeloff, “Direct observation of molecular cooperativity near the glass transition”, *Nature*, **408** (2000) 695–698.

-
- [150] L. A. Deschenes and D. A. Vanden Bout, “Molecular motions in polymer films near the glass transition: a single molecule study of rotational dynamics”, *J. Phys. Chem. B*, **105** (2001) 11 978–11 985.
- [151] L. A. Deschenes and D. A. Vanden Bout, “Comparison of ensemble and single molecule approaches to probing polymer relaxation dynamics near T_g ”, *J. Chem. Phys.*, **116** (2002) 5850–5856.
- [152] A. Schob, F. Cichos, J. Schuster and C. von Borczyskowski, “Reorientation and translation of individual dye molecules in a polymer matrix”, *Eur. Polym. J.*, **40** (2004) 1019–1026.
- [153] B. Schiener, R. Böhmer, A. Loidl and R. V. Chamberlin, “Nonresonant spectral hole burning in the slow dielectric response of supercooled liquids”, *Science*, **274** (1996) 752–754.
- [154] B. Schiener, R. V. Chamberlin, G. Diezemann and R. Böhmer, “Nonresonant dielectric hole burning spectroscopy of supercooled liquids”, *J. Chem. Phys.*, **107** (1997) 7746–7761.
- [155] S. A. Reinsberg, X. H. Qiu, M. Wilhelm, H. W. Spiess and M. D. Ediger, “Length scale of dynamic heterogeneity in supercooled glycerol near T_g ”, *J. Chem. Phys.*, **114** (2001) 7299–7302.
- [156] R. S. Miller and R. A. MacPhail, “Ultraslow nonequilibrium dynamics in supercooled glycerol by stimulated Brillouin gain spectroscopy”, *J. Chem. Phys.*, **106** (1997) 3393–3401.
- [157] R. S. Miller and R. A. MacPhail, “Physical aging in supercooled glycerol: evidence for heterogeneous dynamics?”, *J. Phys. Chem. B*, **101** (1997) 8635–8641.
- [158] G. J. Schutz, H. Schindler and T. Schmidt, “Imaging single-molecule dichroism”, *Opt. Lett.*, **22** (1997) 651–653.
- [159] T. Ha, J. Glass, T. Enderle, D. S. Chemla and S. Weiss, “Hindered rotational diffusion and rotational jumps of single molecules”, *Phys. Rev. Lett.*, **80** (1998) 2093–2096.
- [160] G. S. Harms, M. Sonnleitner, G. J. Schutz, H. J. Gruber and T. Schmidt, “Single-molecule anisotropy imaging”, *Biophys. J.*, **77** (1999) 2864–2870.
- [161] S. Weiss, “Measuring conformational dynamics of biomolecules by single molecule fluorescence spectroscopy”, *Nat. Struct. Biol.*, **7** (2000) 724–729.
- [162] K. D. Weston and L. S. Goldner, “Orientation imaging and reorientation dynamics of single dye molecules”, *J. Phys. Chem. B*, **105** (2001) 3453–3462.

- [163] B. C. Stevens and T. Ha, “Discrete and heterogeneous rotational dynamics of single membrane probe dyes in gel phase supported lipid bilayer”, *J. Chem. Phys.*, **120** (2004) 3030–3039.
- [164] J. W. Gilliland, K. Yokoyama and W. T. Yip, “Effect of Coulombic interactions on rotational mobility of guests in sol-gel silicate thin films”, *Chem. Mat.*, **16** (2004) 3949–3954.
- [165] S. R. Aragon and R. Pecora, “Fluorescence correlation spectroscopy and Brownian rotational diffusion”, *Biopolymers*, **14** (1975) 119–137.
- [166] R. Rigler and E. S. Elson (eds.), “Fluorescence Correlation Spectroscopy: Theory and Applications”, Springer-Verlag, New York (2001), pp. 346–359.
- [167] M. L. Barcellona, S. Gammon, T. Hazlett, M. A. Digman and E. Gratton, “Polarized fluorescence correlation spectroscopy of DNA-DAPI complexes”, *Microsc. Res. Tech.*, **65** (2004) 205–217.
- [168] J. T. Fourkas, “Rapid determination of the three-dimensional orientation of single molecules”, *Opt. Lett.*, **26** (2001) 211–213.
- [169] B. Valeur, “Molecular Fluorescence, an Introduction – Principles and Applications”, Wiley – VCH (2002).
- [170] H. Vogel, “Temperature dependence of viscosity of melts”, *Phys. Z.*, **22** (1921) 645–646.
- [171] G. S. Fulcher, “Analysis of recent measurements of the viscosity of glasses”, *J. Am. Ceram. Soc.*, **8** (1925) 339–355.
- [172] G. Tammann and W. Hesse, “Temperature dependence of viscosity of melted supercooled liquids”, *Z. Anorg. Allg. Chem.*, **156** (1926) 245–247.
- [173] G. Hinze, G. Diezemann and T. Basché, “Rotational correlation functions of single molecules”, *Phys. Rev. Lett.*, **93** (2004) 203 001.
- [174] M. H. Cohen and D. Turnbull, “Molecular transport in liquids and glasses”, *J. Chem. Phys.*, **31** (1959) 1164–1169.
- [175] J. P. Bouchaud, “Granular media: some ideas from statistical physics”, *ArXiv: cond-mat*, (2002) 0211 196.
- [176] P. Lunkenheimer, U. Schneider, R. Brand and A. Loidl, “Glassy dynamics”, *Contemp. Phys.*, **41** (2000) 15–36.
- [177] S. Adichtchev, T. Blochowicz, C. Tschirwitz, V. N. Novikov and E. A. Rössler, “Reexamination of the evolution of the dynamic susceptibility of the glass former glycerol”, *Phys. Rev. E*, **68** (2003) 011 504.
- [178] K. Dawson, G. Foffi, M. Fuchs, W. Götze, F. Sciortino, M. Sperl, P. Tartaglia, T. Voigtmann and E. Zaccarelli, “Higher-order glass-transition singularities in colloidal systems with attractive interactions”, *Phys. Rev. E*, **63** (2001) 011 401.

-
- [179] A. Einstein, "Eine neue Bestimmung der Moleküldimensionen", *Ann. Phys.*, **19** (1906) 289–306.
- [180] A. Einstein, "Berichtigung zu meiner Arbeit: "Eine neue Bestimmung der Moleküldimensionen"", *Ann. Phys.*, **34** (1911) 591–592.
- [181] R. Roscoe, "The viscosity of suspensions of rigid spheres", *Br. J. Appl. Phys.*, **3** (1952) 267–269.
- [182] A. Einstein, "Investigations on the Theory of Brownian Movement", Dover, New York (1956), p. 491.
- [183] P. Coussot, Q. D. Nguyen, H. T. Huynh and D. Bonn, "Avalanche behavior in yield stress fluids", *Phys. Rev. Lett.*, **88** (2002) 175 501.
- [184] D. Bonn, H. Tanaka, P. Coussot and J. Meunier, "Ageing, shear rejuvenation and avalanches in soft glassy materials", *J. Phys.-Condes. Matter*, **16** (2004) S4987–S4992.
- [185] V. Trappe and D. A. Weitz, "Scaling of the viscoelasticity of weakly attractive particles", *Phys. Rev. Lett.*, **85** (2000) 449–452.
- [186] E. R. Weeks, J. C. Crocker, A. C. Levitt, A. Schofield and D. A. Weitz, "Three-dimensional direct imaging of structural relaxation near the colloidal glass transition", *Science*, **287** (2000) 627–631.
- [187] J. Enderlein and C. Zander, "Single Molecule Detection in Solution", Wiley-VCH Verlag, Berlin (2002), pp. 21–67.
- [188] S. T. Hess and W. W. Webb, "Focal volume optics and experimental artifacts in confocal fluorescence correlation spectroscopy", *Biophys. J.*, **83** (2002) 2300–2317.
- [189] J. L. Dela Cruz and G. J. Blanchard, "The influence of chromophore structure on intermolecular interactions. a study of selected rhodamines in polar protic and aprotic solvents", *J. Phys. Chem. A*, **106** (2002) 10 718–10 724.
- [190] H. Carslaw and J. Jaeger, "Conduction of Heat in Solids", Clarendon Press, Oxford, UK (1959).
- [191] C. A. Angell and Y. Choi, "Crystallization and vitrification in aqueous systems", *J. Microsc.- Oxf.*, **141** (1986) 251–261.
- [192] R. L. Sutton, "Critical cooling rates to avoid ice crystallization in solutions of cryoprotective agents", *J. Chem. Soc. Faraday Trans.*, **87** (1991) 101–105.
- [193] C. Branca, S. Magazu, G. Maisano and P. Migliardo, "Anomalous cryoprotective effectiveness of trehalose: Raman scattering evidences", *J. Chem. Phys.*, **111** (1999) 281–287.

- [194] S. Herminghaus, K. Jacobs and R. Seemann, “The glass transition of thin polymer films: some questions, and a possible answer”, *Eur. Phys. J. E*, **5** (2001) 531–538.
- [195] L. Hartmann, W. Gorbatschow, J. Hauwede and F. Kremer, “Molecular dynamics in thin films of isotactic poly(methyl methacrylate)”, *Eur. Phys. J. E*, **8** (2002) 145–154.
- [196] S. Merabia, P. Sotta and D. Long, “Heterogeneous nature of the dynamics and glass transition in thin polymer films”, *Eur. Phys. J. E*, **15** (2004) 189–210.
- [197] A. A. Deniz, T. A. Laurence, G. S. Beligere, M. Dahan, A. B. Martin, D. S. Chemla, P. E. Dawson, P. G. Schultz and S. Weiss, “Single-molecule protein folding: diffusion fluorescence resonance energy transfer studies of the denaturation of chymotrypsin inhibitor”, *Proc. Natl. Acad. Sci. U. S. A.*, **97** (2000) 5179–5184.
- [198] X. W. Zhuang, T. Ha, H. D. Kim, T. Centner, S. Labeit and S. Chu, “Fluorescence quenching: a tool for single-molecule protein-folding study”, *Proc. Natl. Acad. Sci. U. S. A.*, **97** (2000) 14 241–14 244.
- [199] A. A. Deniz, T. A. Laurence, M. Dahan, D. S. Chemla, P. G. Schultz and S. Weiss, “Ratiometric single-molecule studies of freely diffusing biomolecules”, *Annu. Rev. Phys. Chem.*, **52** (2001) 233–253.
- [200] D. H. Hu and H. P. Lu, “Single-molecule nanosecond anisotropy dynamics of tethered protein motions”, *J. Phys. Chem. B*, **107** (2003) 618–626.
- [201] E. Rhoades, E. Gussakovsky and G. Haran, “Watching proteins fold one molecule at a time”, *Proc. Natl. Acad. Sci. U. S. A.*, **100** (2003) 3197–3202.
- [202] E. A. Lipman, B. Schuler, O. Bakajin and W. A. Eaton, “Single-molecule measurement of protein folding kinetics”, *Science*, **301** (2003) 1233–1235.
- [203] E. Rhoades, M. Cohen, B. Schuler and G. Haran, “Two-state folding observed in individual protein molecules”, *J. Am. Chem. Soc.*, **126** (2004) 14 686–14 687.
- [204] V. B. P. Leite, J. N. Onuchic, G. Stell and J. Wang, “Probing the kinetics of single molecule protein folding”, *Biophys. J.*, **87** (2004) 3633–3641.
- [205] E. Haas, “The study of protein folding and dynamics by determination of intramolecular distance distributions and their fluctuations using ensemble and single-molecule FRET measurements”, *ChemPhysChem*, **6** (2005) 858–870.
- [206] H. P. Lu, “Probing single-molecule protein conformational dynamics”, *Acc. Chem. Res.*, **38** (2005) 557–565.

-
- [207] B. Schuler, “Single-molecule fluorescence spectroscopy of protein folding”, *ChemPhysChem*, **6** (2005) 1206–1220.
- [208] M. Borsch and P. Graber, “Subunit movement in individual H⁺-ATP synthases during ATP synthesis and hydrolysis revealed by fluorescence resonance energy transfer”, *Biochem. Soc. Trans.*, **33** (2005) 878–882.
- [209] G. Baldini, F. Cannone and G. Chirico, “Pre-unfolding resonant oscillations of single Green Fluorescent Protein molecules”, *Science*, **309** (2005) 1096–1100.
- [210] M. Rief, M. Gautel, F. Oesterhelt, J. M. Fernandez and H. E. Gaub, “Reversible unfolding of individual titin immunoglobulin domains by AFM”, *Science*, **276** (1997) 1109–1112.
- [211] M. D. Wang, “Manipulation of single molecules in biology”, *Curr. Opin. Biotechnol.*, **10** (1999) 81–86.
- [212] A. Engel, H. E. Gaub and D. J. Müller, “Atomic force microscopy: a forceful way with single molecules”, *Curr. Biol.*, **9** (1999) R133–R136.
- [213] T. R. Strick, M. N. Dessinges, G. Charvin, N. H. Dekker, J. F. Allemand, D. Bensimon and V. Croquette, “Stretching of macromolecules and proteins”, *Rep. Prog. Phys.*, **66** (2003) 1–45.
- [214] R. B. Best, D. J. Brockwell, J. L. Toca-Herrera, A. W. Blake, D. A. Smith, S. E. Radford and J. Clarke, “Force mode atomic force microscopy as a tool for protein folding studies”, *Anal. Chim. Acta*, **479** (2003) 87–105.
- [215] M. S. Z. Kellermayer, S. B. Smith, H. L. Granzier and C. Bustamante, “Folding-unfolding transitions in single titin molecules characterized with laser tweezers”, *Science*, **276** (1997) 1112–1116.
- [216] T. Ha, T. Enderle, D. F. Ogletree, D. S. Chemla, P. R. Selvin and S. Weiss, “Probing the interaction between two single molecules: fluorescence resonance energy transfer between a single donor and a single acceptor”, *Proc. Natl. Acad. Sci. U. S. A.*, **93** (1996) 6264–6268.
- [217] A. A. Deniz, M. Dahan, J. R. Grunwell, T. J. Ha, A. E. Faulhaber, D. S. Chemla, S. Weiss and P. G. Schultz, “Single-pair fluorescence resonance energy transfer on freely diffusing molecules: observation of Förster distance dependence and subpopulations”, *Proc. Natl. Acad. Sci. U. S. A.*, **96** (1999) 3670–3675.
- [218] T. Ha, “Single-molecule fluorescence resonance energy transfer”, *Methods*, **25** (2001) 78–86.
- [219] M. Dahan, A. A. Deniz, T. J. Ha, D. S. Chemla, P. G. Schultz and S. Weiss, “Ratiometric measurement and identification of single diffusing molecules”, *Chem. Phys.*, **247** (1999) 85–106.

- [220] N. K. Lee, A. N. Kapanidis, Y. Wang, X. Michalet, J. Mukhopadhyay, R. H. Ebright and S. Weiss, “Accurate FRET measurements within single diffusing biomolecules using alternating-laser excitation”, *Biophys. J.*, **88** (2005) 2939–2953.
- [221] A. N. Kapanidis, N. K. Lee, T. A. Laurence, S. Doose, E. Margeat and S. Weiss, “Fluorescence-aided molecule sorting: analysis of structure and interactions by alternating-laser excitation of single molecules”, *Proc. Natl. Acad. Sci. U. S. A.*, **101** (2004) 8936–8941.
- [222] B. Schuler, E. A. Lipman, P. J. Steinbach, M. Kumke and W. A. Eaton, “Polyproline and the ”spectroscopic ruler” revisited with single-molecule fluorescence”, *Proc. Natl. Acad. Sci. U. S. A.*, **102** (2005) 2754–2759.
- [223] A. K. Luong, G. C. Gradinaru, D. W. Chandler and C. C. Hayden, “Simultaneous time- and wavelength-resolved fluorescence microscopy of single molecules”, *J. Phys. Chem. B*, **109** (2005) 15 691–15 698.
- [224] H. Schindelin, W. N. Jiang, M. Inouye and U. Heinemann, “Crystal-structure of CspA, the major cold shock protein of *Escherichia coli*”, *Proc. Natl. Acad. Sci. U. S. A.*, **91** (1994) 5119–5123.
- [225] S. E. Jackson and A. R. Fersht, “Folding of chymotrypsin inhibitor-2 .1. evidence for a 2-state transition”, *Biochemistry*, **30** (1991) 10 428–10 435.
- [226] S. E. Jackson, “How do small single-domain proteins fold?”, *Folding Des.*, **3** (1998) R81–R91.
- [227] K. L. Reid, H. M. Rodriguez, B. J. Hillier and L. M. Gregoret, “Stability and folding properties of a model β -sheet protein, *Escherichia coli* CspA”, *Protein Sci.*, **7** (1998) 470–479.
- [228] D. M. Vu, K. L. Reid, H. M. Rodriguez and L. M. Gregoret, “Examination of the folding of *E-coli* CspA through tryptophan substitutions”, *Protein Sci.*, **10** (2001) 2028–2036.
- [229] C. Magg and F. X. Schmid, “Rapid collapse precedes the fast two-state folding of the cold shock protein”, *J. Mol. Biol.*, **335** (2004) 1309–1323.
- [230] E. Boukobza, A. Sonnenfeld and G. Haran, “Immobilization in surface-tethered lipid vesicles as a new tool for single biomolecule spectroscopy”, *J. Phys. Chem. B*, **105** (2001) 12 165–12 170.
- [231] B. Campanini, S. Bologna, F. Cannone, G. Chirico, A. Mozzarelli and S. Bettati, “Unfolding of Green Fluorescent Protein mut2 in wet nanoporous silica gels”, *Protein Sci.*, **14** (2005) 1125–1133.
- [232] B. Halle, “Biomolecular cryocrystallography: structural changes during flash-cooling”, *Proc. Natl. Acad. Sci. U. S. A.*, **101** (2004) 4793–4798.

Dynamica van individuele moleculen bij variabele temperatuur

Inleiding

De afgelopen tien jaar heeft de studie aan individuele moleculen een spectaculaire groei doorgemaakt. Zo is het onder meer mogelijk om individuele moleculen (en atomen) af te tasten in een atomaire krachtmicroscop (AFM) of om hun fluorescentie te meten. Fluorescentie heeft als groot voordeel dat dynamica (het verloop van processen) van individuele fluoroforen direct te bestuderen is, mits een verandering in de fluorescentie optreedt. Alvorens mijn onderzoek te presenteren, beschrijf ik de waarneming van individuele moleculen met fluorescentie, haar toepasbaarheid in dynamische studies, en introduceer ik de temperatuur als een belangrijke instrumentele parameter. In mijn werk heb ik temperatuurvariatie breed toegepast in fluorescentie-experimenten aan individuele moleculen (knippen en bleken, relaxatie in glycerol) alsmede haar toepasbaarheid uitgebreid voor studies aan eiwitvouwing (temperatuurcycli).

Waarnemen van individuele moleculen met zichtbaar licht

In het beschreven onderzoek wordt fluorescenciemicroscopie gebruikt om moleculen waar te nemen met behulp van zichtbaar licht. Microscopie betekent letterlijk het zien van kleine deeltjes. Onder kleine deeltjes verstaat men grofweg wat niet met het blote oog te onderscheiden is, alles kleiner dan een tiende millimeter. Ik wil hier een duidelijk onderscheid maken tussen waarnemen, de aanwezigheid van een object vaststellen, en onderscheiden, het daadwerkelijk zien van een object. Met behulp van sterkere lenzen kunnen steeds kleinere objecten onderscheiden worden, maar er is een limiet, de zogenaamde diffractielimiet. Om dit te begrijpen, is het essentieel om het golfkarakter van licht in beschouwing te nemen. Zichtbaar licht is een klein onderdeel van het elektromagnetische spectrum. Dit spectrum omvat straling met zeer verschillende golflengten, variërend van radiogolven met golflengten van kilometers, tot de schadelijke, radioactieve gammastraling met golflengten van honderdste van nanometers (1 nm is 1 miljardste (10^{-9}) meter). In dit spectrum bevindt zicht-

baar licht zich tussen 400 nm (paars) en 700 nm (diep rood). Het golfkarakter zorgt ervoor dat alleen objecten die groter zijn dan ongeveer de helft van de golflengte, de loop van het licht voldoende veranderen om onderscheidbaar te zijn. Dientengevolge ligt de diffractielimiet voor zichtbaar licht tussen de 200 en de 350 nm. De essentiële vraag is hoe de grootte van een molecuul zich verhoudt tot de diffractielimiet. Een molecuul is het kleinst mogelijke onderdeel van een stof, waaruit na samenvoeging de stof nog steeds kan worden opgebouwd. Moleculen bestaan zelf weer uit atomen, de elementaire bouwstenen van alle materie. In dat licht kan het bestaan van moleculen ook worden gezien als een hiërarchie in sterkte van bindingen. De atomen in een molecuul zijn veel sterker aan elkaar gebonden dan aan de atomen in naburige moleculen. De typische dimensies van moleculen variëren van tiende van nanometers (water) tot enkele tientallen nanometers (eiwitten). Het is derhalve fundamenteel onmogelijk om een molecuul te onderscheiden met zichtbaar licht.

Gelukkig kan men de aanwezigheid van moleculen wel vaststellen met zichtbaar licht door gebruik te maken van de wisselwerking van sommige moleculen met licht. Een bepaalde klasse moleculen, de kleurstoffen, blijkt zichtbaar licht te kunnen opnemen. Dit noemt men absorptie. Na absorptie wil het aangeslagen molecuul zijn extra energie weer kwijt. In de meeste gevallen gebeurt dit door middel van het genereren van warmte, maar een kleine groep kleurstoffen (fluoroforen) zendt na absorptie op haar beurt weer licht uit, fluorescentie. Welnu, het blijkt mogelijk te zijn om de fluorescentie van één enkel molecuul waar te nemen, mits aan de volgende vier voorwaarden wordt voldaan: i) Het fluorofoor moet zeer veel licht kunnen absorberen en dit met hoge efficiëntie weer in fluorescentie omzetten. ii) De lichtbron moet zeer intens zijn, bij voorkeur al haar energie uitzenden in de specifieke kleur die het fluorofoor absorbeert, en het licht moet volledig focusseerbaar zijn (een parallelle bundel). Alleen één specifiek soort lichtbron, de laser, voldoet aan deze voorwaarden. iii) Een zo groot mogelijk gedeelte van de fluorescentie dient op een andere golflengte uitgezonden te worden dan die van de absorptie. In veel gevallen wordt aan deze voorwaarde voldaan, omdat een deel van de opgenomen energie wordt gebruikt om de geometrie van het molecuul te veranderen in de aangeslagen toestand voordat de fluorescentie wordt uitgezonden. Deze fluorescentie is dan roodverschoven, d.w.z. heeft een langere golflengte. Om een voorbeeld te geven, het molecuul rhodamine 6G absorbeert groen licht (500-530 nm) en fluoresceert in het oranje (550-570 nm). Deze roodverschuiving is essentieel, omdat die het mogelijk maakt om door middel van spectrale filters fluorescentielicht te scheiden van het laserlicht. iv) De concentratie van de fluoroforen moet zo laag zijn dat de kans ver-

waarloosbaar is dat er zich meer dan één fluorofoor in het focus van de laser bevindt. Het optisch waarnemen van individuele moleculen is, moge duidelijk zijn, bepaald geen sinecure en slechts mogelijk voor een selecte groep fluoroforen. Desalniettemin is de methode toch breed toepasbaar geworden, omdat men niet-fluorescerende moleculen kan “labelen” met een fluorofoor.

Dynamica van een ensemble versus individuele moleculen

De fluorescentie van vele moleculen tegelijk, een ensemble, is veel gemakkelijker te meten dan die van één enkel molecuul. Daarnaast moet men ook nog eens vele individuele moleculen bestuderen om een ensemblemeting te reproduceren. Toch is een studie aan individuele moleculen zeer de moeite waard, met name wanneer verschillen optreden tussen afzonderlijke moleculen. Dit is onder meer het geval bij de dynamica van complexe processen, zoals eiwitvouwing. Tijdens eiwitvouwing verkrijgt een eiwit zijn specifieke driedimensionale structuur waarna het zijn taak in de cel kan uitvoeren. Dit proces behelst vele tussenstappen en verloopt voor elk eiwitmolecuul verschillend. Dientengevolge is het vrijwel onmogelijk om een ensemble van eiwitten synchroon te laten vouwen en geeft een ensemblemeting slechts een globaal beeld van de voornaamste tussenstappen. In een meting aan individuele moleculen worden alle opeenvolgende tussenstappen voor ieder molecuul afzonderlijk bepaald (mits ze een fluorescentieverandering veroorzaken). Bovendien kunnen correlaties worden vastgesteld tussen verschillende stappen. Op die manier kan het mechanisme volledig worden doorgrond, wat bijvoorbeeld van belang is voor de ontwikkeling van specifieke medicatie. Fluorescentietechnieken voor dynamische studies komen aan de orde in Paragrafen 1.1, 6.1 en 8.2.1.

Dynamica en de temperatuur

Bij het bestuderen van processen zoals eiwitvouwing kan aanvullende informatie worden verkregen door experimentele parameters te variëren, zoals de zuurgraad (pH) of de temperatuur. De temperatuur, een maat voor de gemiddelde energie die een systeem bevat per vrijheidsgraad, is van groot belang voor dynamische studies, omdat de efficiëntie van een proces juist bepaald wordt door die energie. Door de temperatuur te variëren is de kritische hoeveelheid energie, de activeringsbarrière, vast te stellen. Verder kan men bepalen of bij lagere temperaturen andere, langzamere reactiepaden overblijven. Derhalve vormen temperatuurvariatie en de analyse op het niveau van individuele moleculen een ijzersterk paar om een ingewikkeld proces als eiwitvouwing uiteen te rafelen (Paragrafen 1.2 en 8.2).

Knippen en bleken in hydrofiele omgeving

Het ideale fluorofoor zou langdurig en stabiel moeten fluoresceren bij de hoge lichtintensiteit die nodig is om een individueel molecuul waar te nemen. Fluorescentie blijkt echter constant van intensiteit te veranderen en af en toe zelfs enige tijd te verdwijnen. Dit fenomeen, karakteristiek voor één enkel molecuul, noemt men knippen (photoblinking). Als het molecuul voorgoed ophoudt te fluoresceren, spreekt men van bleken (photobleaching). Deze twee processen hangen samen met de mogelijkheid dat een aangeslagen molecuul een verandering ondergaat waarna het niet meer fluoresceert. Als het molecuul weer terug kan keren naar de oorspronkelijke toestand is er sprake van knippen. Wanneer terugkeer onmogelijk blijkt, is het molecuul gebleekt. Knippen en bleken zijn doorgaans verschillend in karakter. Bij knippen is er vaak weinig verschil tussen de lichtgevende en de donkere toestand, bijvoorbeeld slechts een omlegging van een binding tussen twee atomen. Bleken behelst meestal een grootschalige verandering van het molecuul, bijvoorbeeld door reactie met zuurstof (oxidatie). Daarom is bleken sterk afhankelijk van de temperatuur en zijn fluoroforen bij kamertemperatuur veel instabieler dan bij lage temperaturen ($-100\text{ }^{\circ}\text{C}$ en lager). Om een idee te geven, moleculen bleken al na 1 à 2 minuten bij $25\text{ }^{\circ}\text{C}$, maar pas na een uur bij $-200\text{ }^{\circ}\text{C}$. Dit maakt bleken vooral een probleem voor het onderzoek aan biologische moleculen, omdat men juist geïnteresseerd is in het gedrag van die moleculen bij kamertemperatuur.

Bleken is om nog een reden een groot probleem voor het optisch onderzoek aan individuele biologische moleculen. Dit is gerelateerd aan de noodzakelijke waterachtige (hydrofiele) omgeving: water is immers het “oplosmiddel van het leven”. Hydrofiele omgevingen blijken veel reactiever voor fluoroforen dan watervrezende (hydrofobe) omgevingen. Om dit verschil te verklaren, heb ik het knippen en bleken van een fluorofoor, rhodamine 6G, in de waterachtige omgeving van het polymeer poly(vinyl alcohol) bestudeerd (Hoofdstukken 3 en 4). Wij vonden dat de verhoogde reactiviteit onder meer samenhangt met de vorming van een zeer “langlevende” donkere toestand. De fluoroforen bleven soms wel enige minuten donker, terwijl dit normaliter bij knippen korter dan een duizendste (10^{-3}) van een seconde het geval is. De donkere toestand bleek ook direct verantwoordelijk voor een forse toename van de kans op bleken. Door middel van het bepalen van de temperatuurafhankelijkheid van het knippen en het bleken en een directe identificatie door magnetische resonantie, hebben wij aangetoond dat deze niet-fluorescerende entiteit een radicaal (molecuul met een ongepaard elektron) is. Wij waren de eersten om te demonstreren dat radicalen belangrijke intermediairen kunnen zijn in knippen en bleken van organische moleculen.

Relaxatie in glycerol vlak boven het glaspunt

Een glas is een vaste stof die de ordening van een kristal mist. Moleculen met ingewikkelde structuren (polymeren) en/of met sterke onderlinge interacties (glycerol) zijn de voornaamste glasvormers. De temperatuur waarop de vloeistof in een glas overgaat, wordt het glaspunt genoemd. In veel gevallen, waaronder glycerol, ligt het glaspunt ($-83\text{ }^{\circ}\text{C}$) aanzienlijk lager dan het smeltpunt ($+18\text{ }^{\circ}\text{C}$). Tussen deze twee temperaturen noemt men de vloeistof super- of kritisch gekoeld. Hoe dichterbij de vloeistof het glaspunt nadert, hoe hoger haar viscositeit wordt; bij glycerol is die toename maar liefst een factor tien miljard (10^{10}). De viscositeit hangt samen met het gemak waarmee de moleculen opgebouwde spanningen kwijt kunnen raken, hetgeen men relaxeren noemt. Deze spanningen kunnen onder meer het gevolg zijn van externe druk op de vloeistof. Hoe hoger de viscositeit, hoe trager de vloeistof reageert op zulke externe veranderingen. Hoewel glazen zeer veel technische toepassingen hebben, begrijpt men nog steeds vrij weinig van glasvorming. Over het algemeen gaat men er vanuit dat een glasvormer vloeibaar blijft tot aan zijn glaspunt en dan ineens vast wordt omdat de moleculen niet meer ten opzichte van elkaar kunnen bewegen. In de afgelopen jaren is bovendien gebleken dat de relaxatiedynamica van supergekoelde vloeistoffen dicht bij het glaspunt zeer inhomogeen is, d.w.z. zeer verschillende tijdsschalen omvat.

In onze metingen (Hoofdstuk 6) hebben wij gebruik gemaakt van de draaiing (rotatie) van individuele fluoroforen (peryleendicarboximide) in glycerol. Moleculaire rotatie wordt veroorzaakt door botsingen met omringende moleculen. Daaruit volgt dat de rotatie van een individueel gastmolecuul in glycerol wordt bepaald door de relaxatie van de omliggende glycerolmoleculen. Wij vonden inderdaad een brede spreiding van rotatietijden, hetgeen een directe afspiegeling is van de reeds bekende heterogeniteit van de relaxatieprocessen. Echter, tot onze verrassing bleken de fluorescerende moleculen hun specifieke rotatietijd zeer lang te behouden, namelijk vele uren terwijl de moleculaire relaxatieprocessen korter dan een seconde duurden. Wij konden derhalve niet anders concluderen dan dat glycerol reeds bij $25\text{ }^{\circ}\text{C}$ boven het glaspunt een vaste structuur heeft. Doordat deze structuur waarschijnlijk zeer gemakkelijk vervormt, is zij in andere experimenten moeilijk te onderscheiden geweest van een zeer viskeuze vloeistof. Om dit te verifiëren willen wij glycerol binnenkort gaan onderzoeken bij zeer kleine vervormingen. Als het inderdaad als een vaste stof reageert, hebben wij, op instigatie van onze metingen aan individuele moleculen, onomstotelijk aangetoond dat glycerol, een moleculaire glasvormer, geen klassieke vloeistof blijft tot aan zijn glaspunt, een radicale breuk met de heersende ideeën!

Temperatuurcycli van individuele moleculen

Wij hebben een nieuwe methode ontwikkeld voor experimenten aan individuele moleculen bij kamertemperatuur, “temperatuurcycli van dynamica van individuele moleculen” (temperature cycles of single-molecule dynamics), die een langere observatietijd en een hogere tijdsresolutie (de kortste tijd waarbinnen een signaalverandering waarneembaar is) mogelijk moet maken. De beoogde toepassing is eiwitvouwing. Het idee is als volgt: Wij laten een enkel eiwit, met daaraan de eventueel benodigde fluoroforo(en) bevestigd, vouwen in het donker bij kamertemperatuur en koelen het van tijd tot tijd af naar een lage temperatuur (typisch $-150\text{ }^{\circ}\text{C}$) waardoor het vouwingsproces abrupt onderbroken wordt. Vervolgens bepalen wij de voortgang van het proces door middel van een fluorescentiemeting. Bij lage temperatuur is bleken veel minder een probleem en wordt derhalve een langere observatietijd mogelijk. Het is essentieel dat de temperatuurveranderingen snel genoeg zijn om te voorkomen dat water in het eiwit kristalliseert en de eiwitstructuur uiteenvalt (denatureert). Om snel afkoelen mogelijk te maken, verwarmen wij slechts een klein volume rondom het eiwit tot kamertemperatuur, terwijl de omgeving op de lage temperatuur blijft (in een cryostaat). De verwarming wordt bewerkstelligd door een zeer intense laser te focuseren op een lichtabsorberende laag onder het preparaat. Door de verwarmingslaser achtereenvolgens steeds aan en uit te zetten wordt de eiwitvouwing opgedeeld in opeenvolgende stapjes die telkens worden uitgevroren bij lage temperatuur. In Paragraaf 1.3 en in Hoofdstuk 2 worden de techniek en de experimentele realisatie uitvoerig besproken.

In Hoofdstuk 7 hebben wij met rotatiemetingen aan ensembles van fluorescerende moleculen in glycerol de laser-geïnduceerde lokale verwarming gekarakteriseerd. Moleculaire rotatie is temperatuurafhankelijk omdat de viscositeit van glycerol met de temperatuur verandert (zie vorige paragraaf). Op deze manier hebben wij aangetoond dat de verwarmde regio inderdaad zeer klein is, namelijk een paar micrometer (micro is 1 miljoenste, 10^{-6}). Wij konden eveneens vaststellen dat het opwarmen en afkoelen plaatsvindt op een tijdsschaal van microseconden, snel genoeg om ijsvorming te voorkomen. Dit betekent een aanzienlijke verbetering in de tijdsresolutie ten opzichte van normale experimenten aan individuele moleculen, namelijk van milliseconden tot microseconden. Dit komt doordat de resolutie hier slechts wordt beperkt door de snelheid van temperatuurverandering (mits het systeem totaal is vastgevroren bij de lage temperatuur) en niet door de hoeveelheid fluorescentie die een individueel molecuul produceert. In Hoofdstuk 8 beschrijf ik experimenten tijdens welke de rotatie van enkele moleculen is beïnvloed door lokale opwarming, en geef ik een vooruitblik op het te verrichten onderzoek aan eiwitvouwing.

List of Publications

- R. Zondervan, F. Kulzer, J. Berkhout, and M. Orrit, “Relaxation in supercooled glycerol near T_g probed by single-molecule rotational diffusion”, *in preparation*.
- R. Zondervan, F. Kulzer, H. van der Meer, J. A. J. M. Disselhorst, and M. Orrit, “Laser-driven microsecond temperature cycles analyzed by fluorescence polarization microscopy”, *accepted for publication in Biophys. J.*
- R. Zondervan, F. Kulzer, M. A. Kol’chenko, and M. Orrit, “Photobleaching of rhodamine 6G in poly(vinyl alcohol) at the ensemble and single-molecule levels”, *J. Phys. Chem. A* **108** (2004) 1657–1665.
- R. Zondervan, F. Kulzer, S. B. Orlinskii, and M. Orrit, “Photoblinking of rhodamine 6G in poly(vinyl alcohol): radical dark state formed through the triplet”, *J. Phys. Chem. A* **107** (2003) 6770–6776.
- R. Zondervan, F. Kulzer, G. Mathies, and M. Orrit, “Non-exponential kinetics of photoblinking and photobleaching of rhodamine 6G in poly(vinyl alcohol)”, *Single Molecules* **3** (2002) 317–318.
- M. van Gastel, Y. Nagano, R. Zondervan, G. W. Canters, L. J. C. Jeuken, G. C. M. Warmerdam, E. C. de Waal, and E. J. J. Groenen, “Hydrogen bonding in the blue copper site. A resonance Raman study”, *J. Phys. Chem. B* **106** (2002) 4018–4021.
- A. van Duijn-Arnold, R. Zondervan, P. G. Baranov, E. N. Mokhov, and J. Schmidt, “The electronic structure of the N donor center in 4H-SiC and 6H-SiC”, *Phys. Rev. B* **64** (2001) 085206.

Curriculum Vitae

van Rob Zondervan, geboren te Leiden op 13 maart 1978.

In 1996 behaalde ik mijn eindexamen aan het Gymnasium Erasmianum te Rotterdam. Ik slaagde in veertien vakken, destijds een unicum in Nederland aangezien de norm toen nog zeven vakken was. Vervolgens begon ik aan de studie scheikunde in Leiden. De laatste twee jaar verrichte ik onderzoek in de groep die toen nog MAT (Moleculen in Aangeslagen Toestand) heette, begeleid door prof. dr. E. J. J. Groenen en prof. dr. J. Schmidt. Mijn afstudeeronderzoek, onder supervisie van dr. M. Matsushita en prof. dr. J. Schmidt, behelsde de optische karakterisatie van de negatieve siliciumvacature in siliciumcarbide met behulp van ODMR (optische detectie van magnetische resonantie) en hoge-resolutie fluorescentie-excitatiespectroscopie. In augustus 2001 heb ik het doctoraalexamen (master) in de scheikunde afgelegd met afstudeerrichtingen fysische en theoretische chemie.

In september 2001 ben ik in dienst gekomen als onderzoeker in opleiding bij de FOM (Stichting voor Fundamenteel Onderzoek der Materie). Mijn onderzoek verrichtte ik in de vakgroep MoNOS (Molecular Nano-Optics and Spins), voorheen MAT, onder begeleiding van dr. F. Kulzer en prof. dr. M. Orrit. Mijn werkzaamheden behelsden twee richtingen: Enerzijds heb ik de temperatuur gebruikt als parameter in experimenten aan individuele moleculen. Op die manier heb ik ontdekt dat radicalen belangrijke intermediairen zijn in het knippen en bleken van fluorescerende moleculen en dat de eigenschappen van glasachtig glycerol al hoog boven het glaspunt door supra-moleculaire structuren worden gedomineerd. Anderzijds heb ik een nieuwe experimentele methode ontwikkeld om razendsnel de temperatuur rondom een individueel molecuul te kunnen veranderen. Daardoor is het mogelijk geworden om een snel verlopend proces te bestuderen in opeenvolgende stapjes die worden uitgevroren bij lage temperatuur. Mijn bijdrage aan het onderwijs bestond uit het geven van werkgroepen quantumfysica 2a en 2b, quantummechanica 1 en atoom- en molecuulfysica (AMF) en het begeleiden van een IEN-student (bachelor) en drie doctoraalstudenten (master) tijdens hun onderzoeksstages.

Nawoord

Gedurende mijn werkzaamheden in de vakgroep MoNOS heb ik de altijd open deuren, de stimulerende wetenschappelijke omgeving en de oprechte interesse in mijn persoonlijke ontwikkeling zeer gewaardeerd.

Mijn bijzondere dank gaat uit naar de fabuleuze ondersteuning binnen het LION: Voor het fijnmechanische werk stonden Jos Disselhorst en Harmen van der Meer altijd klaar. Naast vele “kleinere” klussen hebben Harmen en Jos de insert ontworpen en gebouwd voor de “temperature-cycle microscope”, waardoor zij zeer fascinerend onderzoek aan dynamica van individuele moleculen hebben mogelijk gemaakt. Ook de overige leden van de FMD waren altijd bereid bij te springen. Voor elektronische zaken kon ik immer een beroep doen op René Overgaww, Arno van Amersfoort, Leendert Prevo, Bert Crama, Raymond Koehler of Ton Tampung. Verder zorgden Arno en Leendert voor een perfect functionerend netwerk en ben ik Arno zeer erkentelijk voor de prettige manier van zijn computerbeheer. De dames van het secretariaat, Henriëtte van Leeuwen, Anneke Aschoff, Daniëlle van Raaij en Riet Nieuwenhuijzen droegen altijd zorg voor de administratieve ondersteuning. Helaas is gedurende mijn promotie Anneke ernstig ziek geworden en uiteindelijk overleden. Zij was een sociaal voelende en markante persoonlijkheid die dan ook node wordt gemist. During my PhD, I shared my office first with Michio Matsushita and later with Markus Lippitz. I wish to explicitly thank them for their continuing interest in my scientific efforts and the endless amounts of advise and help that I received. Ik ben zeer erkentelijk voor de bijdrage van Markus Lippitz, Sergei Orlinskii, Mikhail Kol’chenko, Aurélien Nicolet, Jennifer Mathies, Elsbeth van der Togt en Joris Berkhout aan mijn wetenschappelijk werk. Verder wil ik Rogier, Alexander, Meindert en al mijn andere collega’s bij de MoNOS (en vroegere MAT) bedanken voor de interessante gesprekken over wetenschap en de vele discussies over politiek (al zullen sommigen van jullie deze meer als monologen herinneren...).

Tot slot wil ik mijn vrienden en familie bedanken, die mij als rare bèta in de bijt al die jaren hebben getolereerd. In het bijzonder noem ik mijn ouders en mijn zus Ingrid die altijd voor me klaar hebben gestaan, en uiteraard Susanne die als enige weet uit welke bergen en dalen mijn leven als promovendus echt heeft bestaan.